SAND2015-8102R

SNF Interim Storage Canister Corrosion and Surface Environment Investigations

Fuel Cycle Research & Development

Prepared for
U.S. Department of Energy
Used Fuel Disposition Program
C.R. Bryan and D.G. Enos
Sandia National Laboratories
September 7, 2015
FCRD-UFD-2015-00511

Sandia National Laboratories is a multi-program laboratory managed and operated by Sandia Corporation, a wholly owned subsidiary of Lockheed Martin Corporation, for the U.S. Department of Energy's National Nuclear Security Administration under contract DE-AC04-94AL85000.

Reserved for Signature page

SUMMARY

This progress report describes work being done at Sandia National Laboratories (SNL) to assess the localized corrosion performance of container/cask materials used in the interim storage of spent nuclear fuel (SNF). Of particular concern is stress corrosion cracking (SCC), by which a through-wall crack could potentially form in a canister outer wall over time intervals that are shorter than possible dry storage times. In order for SCC to occur, three criteria must be met. A corrosive environment must be present on the canister surface, the metal must susceptible to SCC, and sufficient tensile stress to support SCC must be present through the entire thickness of the canister wall. SNL is currently evaluating the potential for each of these criteria to be met.

To assess the environment, SNL has continued to work with the Electric Power Research Institute in characterizing dust on canisters at Independent Spent Fuel Storage installations, evaluating dust samples from the surface of an unused canister at the Hope Creek site. Strong evidence of particle-to-gas conversion reactions were found, that are effective at converting chloride salts into harmless sulfates or nitrates on the canister surface. Moreover, salt loads were actually heavier on the sides of the unused canister than on the in-service canisters sampled previously, despite the much shorter storage time, and much lower air flow rates though the overpack. This may indicate that thermophoresis is effective at rejecting dust from the surface of hot in-service canisters. Additional environment investigations include experimental work evaluating the stability of salts and deliquesced brines on hot canister surfaces; thermally-driven exchange reactions with the atmosphere may work to make salt assemblages or brines less corrosive. Moreover, the work can help define realistic salt assemblages and brine compositions for experimental studies. Preliminary studies have shown that ammonium chloride and ammonium nitrate decompose rapidly in the solid state, and cannot accumulate on a hot package. It is likely that a deliquesced brine containing ammonium and either nitrate or chloride cannot persist—it will degas ammonia and an acid gas (HCl, HNO_3, or both) until one or the other is consumed. These experiments both support development of relevant experimental matrices and potentially provide arguments for lengthening inspection intervals at some inland sites where chloride deposition may be overwhelmed by deposition of ammonium minerals.

The potential for high residual tensile stresses in interim storage canisters, and canister material properties, including material susceptibility to SCC are being evaluated by analysis of a full-diameter cylindrical mockup of a canister, fabricated by a canister supplier using the same materials and manufacturing procedures as real in-service canisters. Residual stresses due to cold working and welding processes are being measured in and around longitudinal and circumferential welds, simulated weld repair regions, and base metal far from any welds. Work to data has shown that base metal stress patterns are dominated by a bending moment introduced during rolling of the plate into a cylinder, with the outer half of the shell dominated by tensile stresses, and the inner half, by compressive stresses. Material characterization studies will begin once stresses are well understood and the mockup can be sectioned into smaller pieces, and will include 3-dimensional characterization of the degree of sensitization and textural changes near weld zones. Ultimately, this information will be used to identify relevant sample properties and stress states for corrosion testing. A suite

of corrosion tests are being planned to (1) measure important environmental parameters such as threshold relative humidity and the salt surface load required for pitting and SCC initiation and growth (pits are precursors for SCC); (2) characterize pit initiation and growth rates as a function of environmental conditions; (3) SCC initiation experiments under relevant salt loads and compositions; and (4), SCC growth experiments evaluating the potential importance of processes such as cathodic limitation due to limited brine volumes and assessing crack growth rates as a function of time, crack depth, and salt load. All experiments will be carried out using samples prepared to match material properties and stresses determined from the mockup characterization work.

CONTENTS

FIGURES

TABLES

ACRONYMS

AH	Absolute humidity
ASTM	American Society for Testing and Materials
CISCC	Chloride Induced Stress Corrosion Cracking
CRADA	Cooperative Research and Development Agreement
CRIEPI	Central Research Institute of the Electric Power Industry (Japan)
DHD	Deep Hole Drilling
DOE	Department of Energy
EDM	Electric Discharge Machining
EDS	Energy-Dispersive [X-ray] Spectroscopy
EPR	Electrochemical Reactivation
EPRI	Electric Power Research Institute
FCRD	Fuel Cycle Research and Development
FME	Foreign Material Exclusion [Cover]
HAZ	Heat-Affected Zone
iCHD	Incremental Center-Hole Drilling
iDHD	Incremental Deep-Hole Drilling
ISFSI	Independent Spent Fuel Storage Installation
NDE	Non-Destructive Evaluation
NEUP	Nuclear Energy University Programs
NRC	Nuclear Regulatory Commission
NWTRB	Nuclear Waste Technical Review Board
PDM	Potential Drop Method
RH	Relative Humidity
RH_D	Deliquescence Relative Humidity
RH_L	Limiting Relative Humidity for Corrosion
SCC	Stress Corrosion Cracking
SEM	Scanning Electron Microscope
SNF	Spent Nuclear Fuel
SNL	Sandia National Laboratories
SS	Stainless Steel
UFD	Used Fuel Disposition
WRS	Weld Residual Stress
XRD	X-Ray Diffraction
XRF	X-ray Fluorescence

SNF INTERIM STORAGE CANISTER CORROSION AND SURFACE ENVIRONMENT INVESTIGATIONS

1. INTRODUCTION

This progress report describes work being done at Sandia National Laboratories (SNL) to assess the localized corrosion performance of container/cask materials used in the interim storage of spent nuclear fuel (SNF). Of particular concern is stress corrosion cracking (SCC), a localized corrosion phenomenon by which a through-wall crack could potentially form in a canister outer wall over time intervals that are shorter than possible dry storage times. Work is being done at SNL to evaluate the potential for SCC of interim storage canisters. It involves characterization of the physical and chemical environment on the surface of the storage canisters and how it might evolve through time; testing to characterize canister materials and to evaluate performance of the materials under anticipated storage conditions; and characterization of stress present in the canister materials due to manufacturing processes.

In order for SCC to occur, three criteria must be met (Figure 1): an aggressive chemical environment must exist, the metal must be susceptible to SCC, and sufficient tensile stress must be present to support SCC. In general, these criteria are expected to be met, at least at some Independent Spent Fuel Storage Installation (ISFSI) sites, during the period of interim storage, which may be far longer the original canister design specifications because of the current lack of a pathway for final disposal. Each of the criteria for stress corrosion cracking is being addressed by current work at SNL.

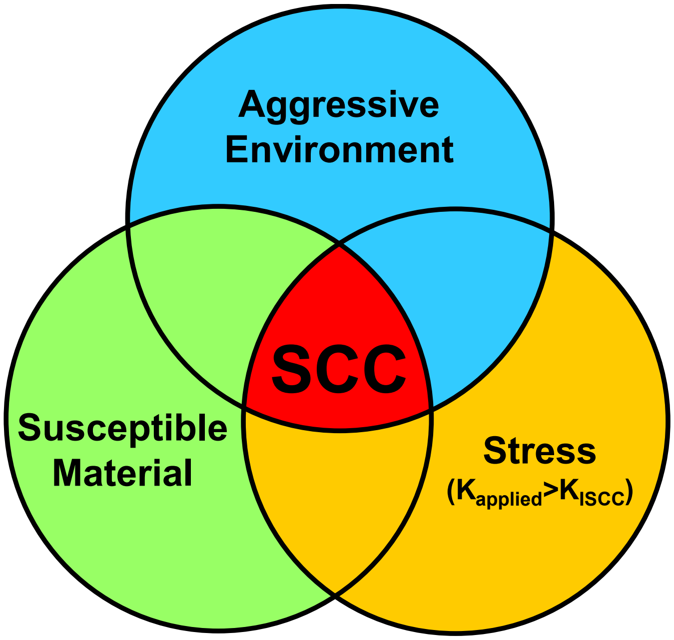

Figure 1: Criteria for SCC initiation and propagation.

Aggressive chemical environment: Field sampling of surface deposits on in-service SNF storage canisters at three near-marine ISFSI sites has been carried out over the last three years, and analyses have shown that chloride-rich salts can be present on the canister surfaces (Enos et al. 2013; Bryan and Enos 2014b;

EPRI 2014a; Bryan and Enos 2015). Once portions of the canister surfaces cool sufficiently for these salts to deliquesce, a corrosive chloride-rich aqueous environment could potentially form.

SNL has been working with the Electric Power Research Institute (EPRI) as part of a cooperative research and development agreement (CRADA) to collect and analyze dust samples from the surface of in-service SNF storage canisters. In FY15, a final set of samples was analyzed. These were samples that were collected from the surface of an unused storage canister, stored within an overpack at the Hope Creek ISFSI for one year. Sampling an unloaded canister was much easier and cheaper than sampling an in-service canister. Moreover, comparing dust samples from the unloaded canister to those from loaded, in-service canisters at the site may provide information on the effects of heating on the composition of deposited dusts. The results of the unused canister dust analyses are discussed in Section 2 of this report.

While corrosive salts may be deposited on canister surfaces, many different processes can occur that will modify the composition of the salts, or of the brines that form by deliquescence of the salts. SNL is experimentally evaluating salt and brine stabilities as a function of composition, under environmental conditions relevant to canister surfaces. As part of this work, a system was developed for depositing salts onto metal surfaces for atmospheric corrosion testing purposes. The system is capable of controlled deposition of very even salt loadings at very low total salt loads per unit area, duplicating anticipated field conditions. It will be used to prepare samples for both salt/brine stability tests and for SCC corrosion tests. Preliminary results of these experiments are described in Section 3 of this report.

Susceptible material: The majority of SNF dry storage casks currently in use are made from austenitic stainless steels, including 304, 304L, and 316. Should sufficient tensile stress be present, there is ample evidence that these stainless steels are susceptible to chloride-induced SCC (CISCC) in aggressive chloride-bearing environments. SCC of 304 stainless steel (SS), the most widely used alloy for containers that are currently in service, occurs readily in experimental tests with deliquesced sea-salts (e.g., Nakayama 2006; Prosek et al. 2009; Tani et al. 2009; Mintz et al. 2012; Prosek et al. 2014), and has also been observed in near-marine ambient temperature field tests and industrial sites (Kain 1990; Hayashibara et al. 2008; Kosaki 2008; Cook et al. 2011; Nakayama and Sakakibara 2013; Cook et al. 2014). However, overall susceptibility is a function of several factors, including the degree of sensitization, the degree of cold work, and the surface finish (Parrott and Pitts 2011); to date, none of these factors have been assessed for materials representative of fielded interim storage canisters.

- Degree of sensitization — austenitic stainless steels contain a small amount of carbon, and when welded, are prone to a phenomenon known as sensitization when welded. In the material adjacent to the weld fusion zone (i.e., the heat affected zone (HAZ) the thermal cycling associated with the welding process facilitates the nucleation of chromium carbides along grain boundaries. The diffusion of chromium from the surrounding microstructure enables growth of these carbides. As the mass transfer rate of chromium is much higher along grain boundaries than in the bulk of the material, chromium moves from the material within each grain to the grain boundary, where it rapidly diffuses to the growing chromium carbides. As a result, the regions adjacent to the grain boundaries become depleted in chromium, eventually dropping to well below the 10% Cr threshold required to maintain a protective chromium oxide on the metal surface. These Cr-depleted zones are thus more susceptible to corrosion than the surrounding grains, and serve as a preferential site for localized corrosion initiation. These localized corrosion sites, in turn, can serve as initiation sites for stress corrosion cracking. The first grain boundaries to become sensitized are those along which there is the greatest lattice mismatch between adjacent grains, but with progressive heating, more and more grain boundaries become sensitized. The degree of sensitization is defined as the percentage of grain boundaries that are sensitized. In general, the degree of sensitization induced by welding increases with the thickness of the weld, as the heat input is greater.

Sensitization has many effects on localized corrosion. As the degree of sensitization increases, pit incubation times decrease, while pit nucleation and growth rates increase. As pits frequently serve as initiation sites for SCC, the nucleation rate for SCC cracks also increases. Nakayama and Sakakibara (2013) estimate that the induction time for SCC initiation can decrease by more than an order of magnitude as the degree of sensitization increases from 0 to 20%, and that crack propagation rates can increase by a factor of 5, for atmospheric SCC conditions. Khatak et al. (1996) also saw increases in crack growth rates for sensitized 304 SS, and noted that sensitization significantly lowered the threshold stress intensity for SCC. Sensitization can also result in a change in the SCC mechanism: in sensitized materials SCC is, at least initially, intergranular, while in unsensitized materials, it is transgranular.

The degree to which an austenitic stainless steel can sensitize is a function of its carbon content, with reduced carbon content alloys (e.g., L grade stainless steels such as 304L) being less susceptible. Current canisters are made from dual-certified 304/304L SS; however, some early canisters may have been made from 304 SS with a higher carbon content (Pacific Nuclear Fuel Services 1991).

- Degree of cold work — The deformation of concern here comes from two sources – the bending of the plate stock used to manufacture the container into a cylinder, as well as local deformation due to grinding operations on the surface of the container, with the magnitude of the latter being the most significant. Cold work can adversely affect the corrosion resistance of stainless steels (Khatak et al. 1996; García et al. 2001; Parrott and Pitts 2011). First, it results in the formation of extensive dislocation structures within the metal matrix, which can result in the formation of regions where destabilization of the protective oxide layer is more likely and the ability of the material to repassivate is degraded (Peguet et al. 2007), increasing the susceptibility to localized attack. For large deformation, the formation of strain-induced martensite in the metal is possible, which is less resistant to corrosion than austenite. Martensite that is incident with the metal surface can serve as sites where the susceptibility to localized corrosion initiation is enhanced. SCC crack growth rates have also been observed to increase with increasing cold work, particularly at 20% cold work and above (Kuniya et al. 1988).
- Surface finish — A rough surface finish (>1 µm) has also been found to promote initiation of localized corrosion, as chloride ions are trapped and concentrated in heterogeneities that exist on the metal surface (Parrott and Pitts 2011). Surface grinding can also produce large local variations in stress and microstructure near the surface, which may contribute by increasing strain energy and the dissolution rate of the metal (Ghosh and Kain 2010a; 2010b; Ghosh et al. 2011). Localized corrosion initiation at the highly stressed surface irregularities also results in an increased nucleation rate of SCC cracks within and adjacent to the resulting pits (Turnbull et al. 2011). All storage canisters will have a roughly ground surface with a roughness well in excess of 1 µm.

While these factors are known to affect susceptibility to SCC, they are all specific to the material and to the manufacturing processes used to fabricate the canister. In order to evaluate them, it is necessary to obtain relevant metal samples, from a canister or mockup made using the same techniques as real, in-service canisters. SNL purchased a full diameter cylindrical mockup of an interim storage canister, made using the same materials and manufacturing processes as one type of in-service canister, in 2014, and is in the process of characterizing the material properties of the canister base metal and weld zones. The status of the mockup characterization work was recently summarized in Enos and Bryan (2015); a short summary is presented here in Section 4. The mockup will provide information on material properties for developing corrosion testing protocols using relevant materials, and will also provide actual samples for testing purposes. Planned experimental work is summarized in Section 6.

Tensile stress: In order for an SCC crack to initiate, the tensile stresses in the metal must be of a sufficiently large magnitude that the threshold stress intensity value at a potential nucleation site is exceeded. In order for an initiated crack to propagate and penetrate through the container, the applied stress intensity at the crack front must be maintained above that threshold. In other words, a sufficiently large tensile stress state must exist through the entire wall thickness. Tensile stresses may be applied externally—for instance, by loading or by pressurization—but for SNF interim fuel canisters, external loads are negligible relative to the yield stress of the metal. High residual tensile stresses may be present in the metal, however, due to cold working or welding. Weld residual stresses (WRS) are generally the most important component, and are a function of many factors, including weld geometry, sample thickness, welding speed, number of passes, inter-pass temperatures, and base metal properties relative to the weld. Because of this, WRS are specific to the geometry and welding processes used, and can only be measured from an actual storage canister or a mockup made using the same procedures as the real canisters. However, WRS measurements on samples with relevant geometries and typical welds have never been done. The NRC modeled WRS for typical canister welds using finite element methods (NRC 2013), and predicted that within the HAZ of both longitudinal and circumferential welds, sufficient tensile stresses would be present to support SCC. Moreover, they predicted that the tensile stresses would be present through the thickness of the cylinder wall, permitting full penetration over time.

Typical weld residual stresses for one type of interim storage canister are being obtained by characterization of the SNL full diameter mockup. As noted previously, the status of the mockup characterization work was recently provided in Enos and Bryan (2015), but a short summary is presented here in Section 4.

Section 5 describes current and planned corrosion experimental work at SNL. Current experiments address potential limits on the extent of localized corrosion in the presence of a limited amount of reactants. It has been theorized that limited salt loads on metal surfaces will limit the extent of corrosion over time (SNL 2008), and SNL has previously performed experimental work to assess that. The experiments involved crevice corrosion of 304 SS samples sprayed with known amounts of salts, and were summarized in Enos et al. (2013) and Bryan and Enos (2014a). However, the experiments were only carried out for a duration of 100 days, and the results were ambiguous. A new set of experiments has been initiated that will be carried out for a longer duration.

Preliminary plans for experimental work to assess the potential for through-wall SCC of SNF interim storage canisters are also discussed in Section 5. The work will evaluate important assumptions and parameter values required for prediction of SCC penetration times, including the potential dependence of pitting and SCC incubation times on salt load; environmental conditions for SCC (e.g., relevant relative humidity (RH) and salt surface load thresholds, if they exist); corrosion crack growth rates and their dependence, on chloride surface load; and finally, the potential effects of deliquescence hysteresis on estimated total times of wetness.

2. ANALYSIS OF DUST SAMPLES FROM THE SURFACE OF AN UNUSED SNF INTERIM STORAGE CANISTER AT THE HOPE CREEK ISFSI.

SNL has been working with EPRI as part of a CRADA to collect and analyze dust samples from the surface of in-service SNF storage canisters. As part of this sampling effort, samples of dusts have been collected and analyzed from the surfaces of in-service canisters at three sites, the Calvert Cliffs ISFSI, the Hope Creek ISFSI, and the Diablo Canyon ISFSI. The Calvert Cliffs samples were analyzed in part by an external lab contracted by EPRI, and in part by SNL and results are reported in Calvert Cliffs Nuclear Power Plant LLC (2013) and in Enos et al. (2013). The samples from in-service canisters at the Hope Creek and Diablo Canyon sites were characterized by SNL and are described in Bryan and Enos (2014b). In summer of 2014, a final set of samples was collected, from the surface of an unused storage canister stored within an overpack at the Hope Creek Site for one year. The foreign material exclusion (FME) cover that had been on the top of the canister during storage, and a second recently-removed FME cover, were also sampled. The sampling was done for several reasons. First, it offered the opportunity to assess the potential effects of heating on dust deposited on an in-service canister relative to dust deposited under ambient conditions on the unused canister. Second, dust could be collected easily, since the empty canister was not emitting high levels of radiation. Finally, it offered an additional opportunity to collect and analyze dust deposited on a vertical steel surface at the Hope Creek site. The samples were analyzed at SNL in the fall of 2014.

As with the in-service canisters, both wet and dry samples of the dust/salts were collected, using SaltSmart™ sensors and Scotch-Brite™ abrasive pads, respectively. The SaltSmart™ samples were leached and the leachate analyzed chemically to determine the composition and surface load per unit area of soluble salts present on the canister surface. The dry pad samples were analyzed by X-ray fluorescence (XRF) and by scanning electron microscopy (SEM) to determine dust texture and mineralogy; and by leaching and chemical analysis to determine soluble salt compositions. The results of the unused canister and FME cover dust analyses are summarized here; the complete analyses are available in Bryan and Enos (2015).

2.1 Samples and Methods

2.1.1 Samples

Unlike the sampling of the in-service canisters at Hope Creek where extensive tooling was required to acquire dust samples, the unused canister, MPC-387, was removed from its overpack and the SaltSmart™ and Scotch-Brite™ samples were collected by hand. Samples were collected from three locations on the side of the canister. The sampling plan called for then sampling dust on the Foreign Material Exclusion (FME) cover on top of the canister; however, the FME cover was inadvertently removed and placed outdoors in an exposed location, and the top of the canister, which had been shielded during storage, was sampled instead. When the error was discovered, the sampling team returned to the site and collected samples from the FME cover. An adjacent FME cover (MPC-389), also in exposed storage, was also sampled. Unfortunately, in the intervening days, a thunderstorm had thoroughly washed the FME covers, probably removing most of the soluble salts. Table 1 lists the samples that were collected and the sampling locations.

Table 1. Hope Creek dust samples collected from unused storage canister MPC-387

Sample #	**Sample Type**	**Sample location**
387-001	Dry pad	Canister side, 1 foot from base
387-002	SaltSmart	Canister side, 1 foot from base
387-003	Dry pad	Canister side, 1 foot from top
387-004	SaltSmart	Canister side, 1 foot from top
387-005	Dry pad	Canister lid, 1 foot from edge
387-006	SaltSmart	Canister lid, 1 foot from edge
387-007	Dry pad	Canister lid, center
387-008	SaltSmart	Canister lid, center
387-009	Dry pad	Canister side, 5 feet from base
387-010	SaltSmart	Canister side, 5 feet from base
387-011	Dry pad	FME cover, 1 foot from edge
387-012	SaltSmart	FME cover, 1 foot from edge
387-013	Dry pad	FME cover, center
387-014	SaltSmart	FME cover, center
389-015	Dry pad	FME cover, 1 foot from edge
389-016	SaltSmart	FME cover, 1 foot from edge
387-017	SaltSmart	FME cover, center

2.1.2 Methods

Upon delivery to Sandia, the samples were examined and a description was recorded. No discoloration was visible on any samples; salt and dust loads on the Saltsmart^{TM} wicks and the Scotch-Brite^{TM} pads were too light to be seen. When the SaltSmart™ samples were disassembled to extract the soluble salts, the condition of the wick and the reservoir pad was also noted; no discoloration was observed.

The methods and equipment used to characterize the samples are identical to those used previously for the in-service canisters, and include:

- *Scanning Electron Microscope (SEM) imaging and Energy Dispersive X-ray Spectroscopy (EDS) element mapping. SEM/EDS analysis of the dry dust samples* provides textural and mineralogical information of dust/dust components, and allows visual identification of organic matter (floral/faunal fragments).
- *X-ray Fluorescence (XRF) analysis*. This method was implemented as a microbeam technique, allowing chemical mapping of the dry dust samples on the surface of the collection pads, with a resolution of ~25 µm. It provides semi-quantitative chemical analyses. However, one limitation is that elements lighter than sodium (e.g. oxygen, nitrogen, carbon) cannot be detected, and sensitivity to sodium is low.
- *Chemical analyses of the dust and soluble salts.* The soluble salts were leached from the components of the SaltSmart™ sensors and analyzed. For the dry samples, the Scotch-Brite™ pad was washed thoroughly with deionized water and the leachate collected and filtered. The leachate was then analyzed for soluble salts.

A more detailed discussion of each method is presented in Bryan and Enos (2014).

2.2 SEM Analysis

SEM/EDS analysis of the dry pad samples was carried out to determine dust and salt mineralogy, to identify organic materials present, and to determine dust particle size and morphology. Analyzed samples include pads from the Hope Creek unused canister and from the FME cover (Table 1). SEM images were taken of characteristic features and EDS element mapping was done to assess mineralogy. Results are summarized here with typical images from some samples; a complete suite of analyses is provided in Bryan and Enos (2015).

2.2.1 Samples from the Surface of Canister MPC-387

All of the Scotch-Brite™ pad samples that were collected from the canister were analyzed (Table 1). Dust loads were relatively heavy on the pads used to sample the sides of the canister (Figure 2, upper), and somewhat lighter on those pads used to sample the canister top (Figure 2, lower), which had been protected by the FME cover during storage. However, the mineralogy varied little from location to location. For all samples, the most abundant particles present are stainless steel particles, associated with the manufacturing (cutting and grinding) of the canister shell. These are shown in a high magnification SEM image and element maps in Figure 3, from the side of the canister. (Note that on these and other figures, the Ni map is not included to save space, however, as a component of stainless steel, Ni was co-located with Fe and Cr in all mapped areas). Terrestrially-derived dust particles are less common, and are dominantly quartz and aluminosilicates. Several salts are present, and are mostly sulfates or bisulfates. Ca-SO_4 is the most common phase (e.g., Figure 4), but K-SO_4, Na-K-SO_4, and Mg-Ca-carbonate phases are also present. On the canister top, rare grains of NaCl and $NaNO_3$ are also present. At all locations, the salts are commonly associated with clusters of fine grained aluminosilicates, probably clays.

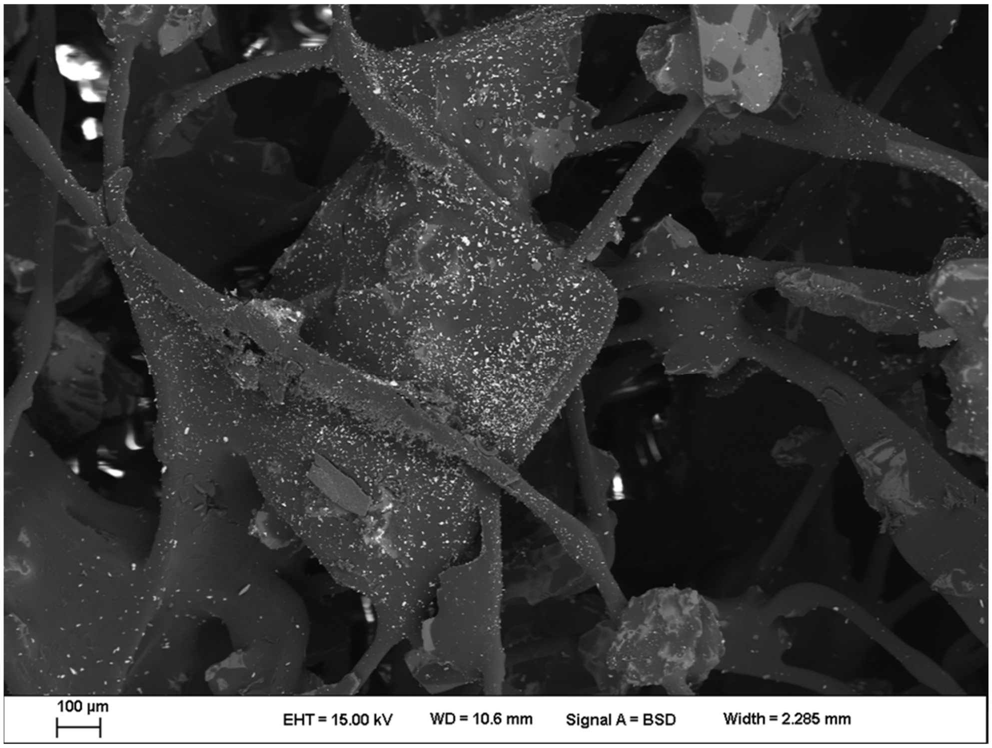

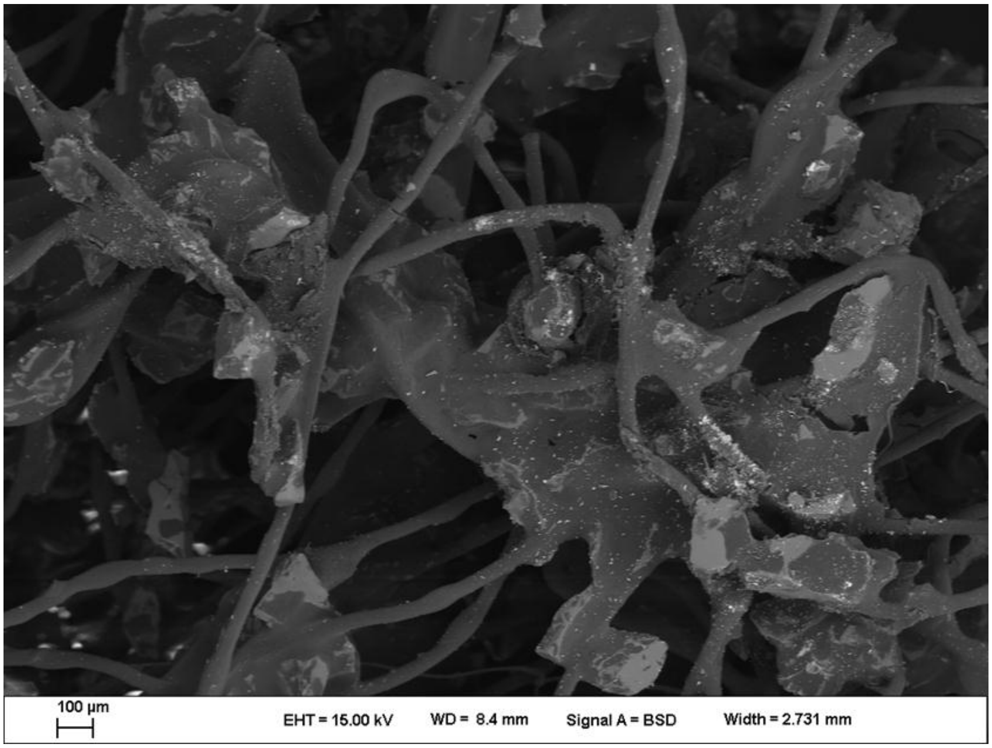

Figure 2. SEM images of pad samples collected from the unused canister. Upper: Sample 387-001, collected from the canister side, 1 foot above the bottom edge. Lower: Sample 387-007, collected from the center of the canister top. Note the much lighter dust load on the sample from the canister top, which was protected during storage by the FME cover.

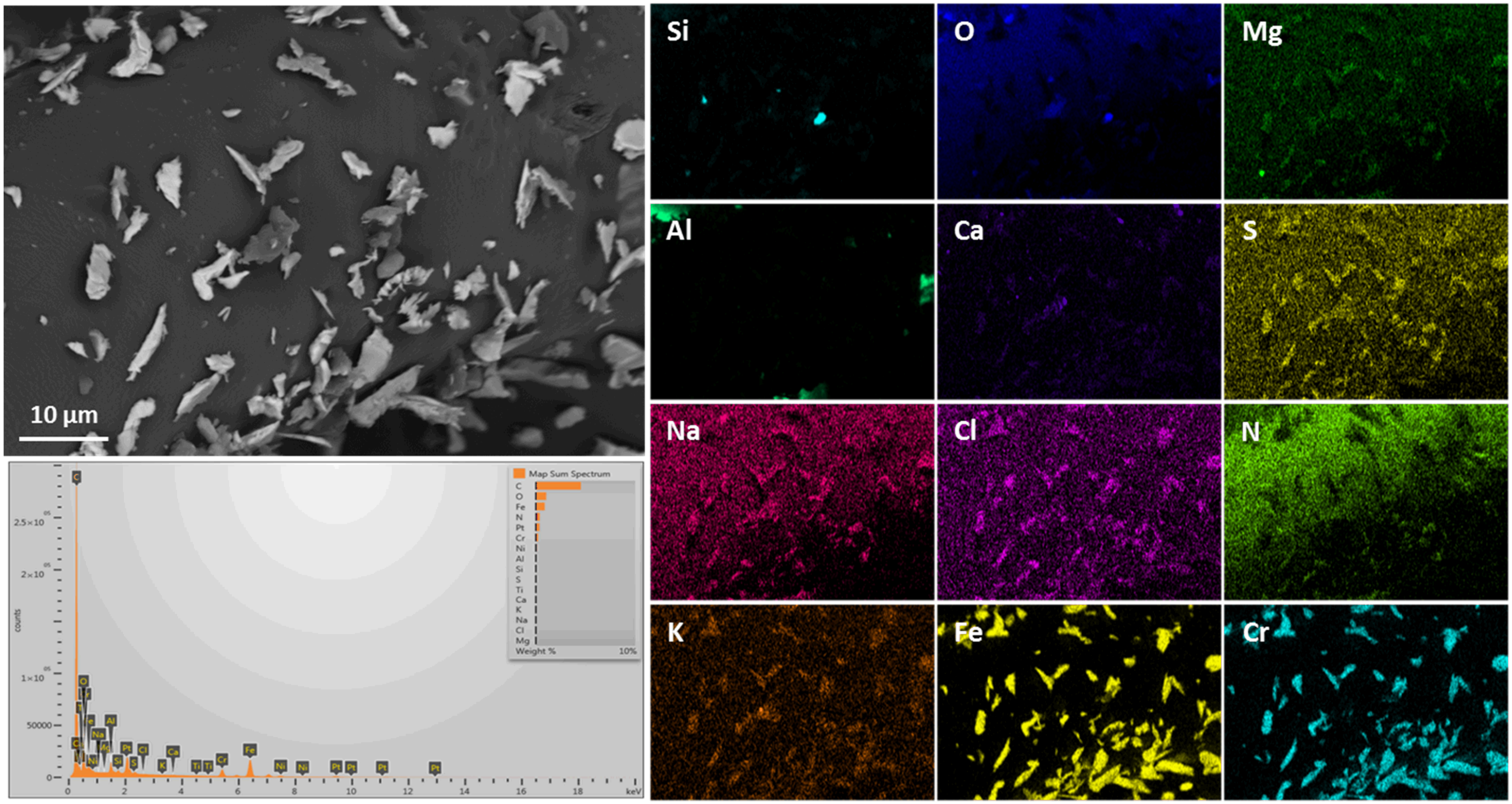

Figure 3. SEM image/EDS map of Sample 387-003, collected from the canister side, 1 foot below the top edge. Almost all particles are stainless steel.

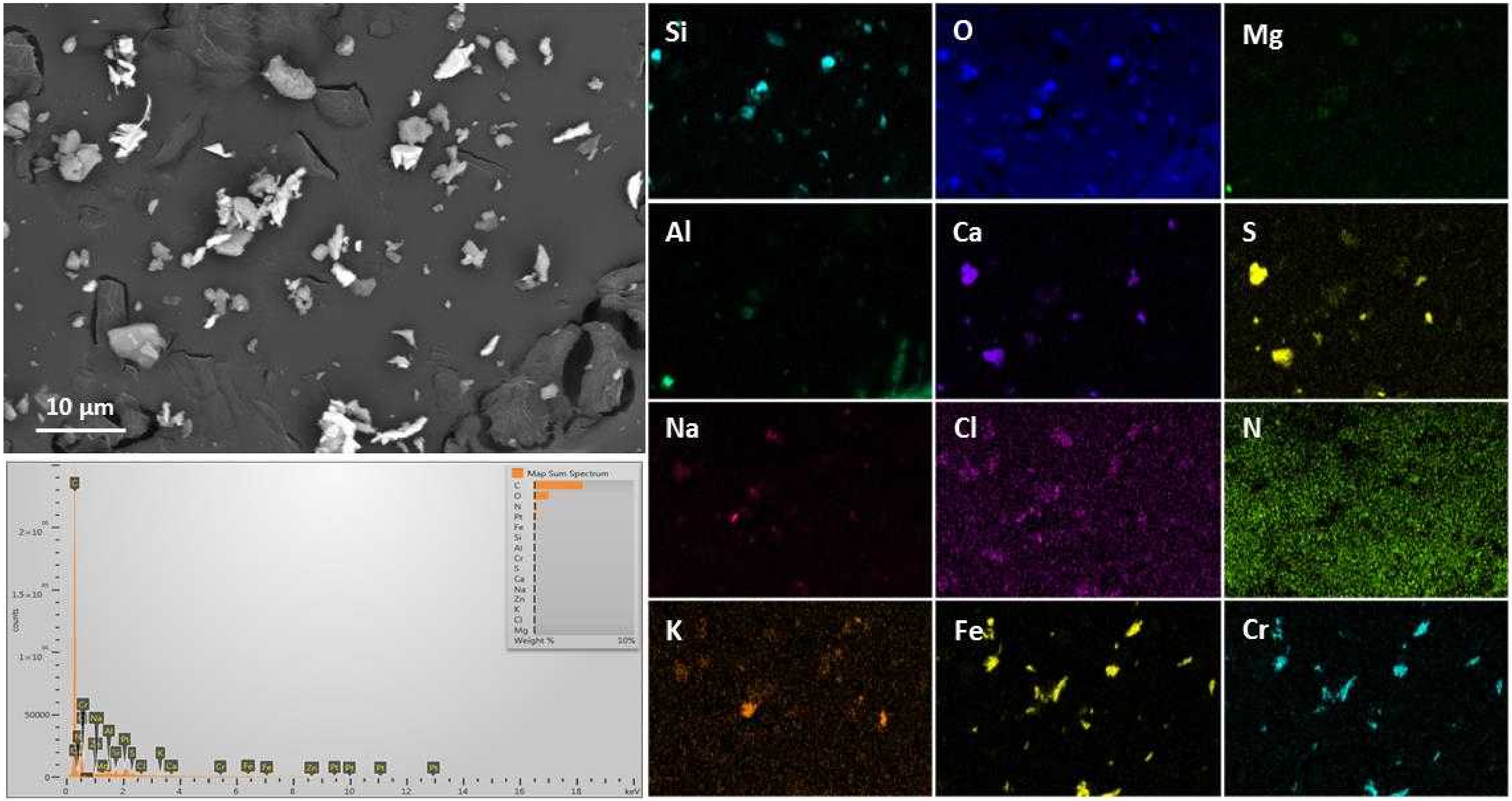

Figure 4. SEM image/EDS map #1 of Sample 387-007, collected from the center of the canister top. Note stainless steel and Ca-SO_4 grains.

2.2.2 Samples from the Foreign Material Exclusion Cover

As noted previously, the FME cover was stored outside for several days prior to sampling, and had been rained on prior to sampling. Expectations were low that dust remained on the cover at the time of sampling. However, although dust loads on the pad samples from the FME cover were variable, they were generally higher than those from canister. In addition to having generally higher dust loads than the samples from the canister itself, the FME samples have significantly different compositions. While the canister dusts consisted almost entirely of stainless steel particles, the dust on the FME cover seems to be dominantly terrestrially-derived silicate and aluminosilicate particles, and stainless steel particles are rare. Salt phases are common, and consist almost entirely of sulfates, but a few specks of nitrate-rich material were observed. No unequivocal chloride mineral grain was observed.

A representative SEM image and EDS maps are shown for a typical FME sample in Figure 5. The silicate minerals include quartz and various Na, K, Ca, Mg, and Mg-Fe aluminosilicates that are probably a mixture of feldspars and clays. Calcium carbonate is present. Sulfates are the most abundant salts present, occurring as Ca-SO_4 but mostly as a Na-Al-SO_4 phase (Figure 6). While Na-Al-SO_4 minerals occur naturally in areas of hydrothermal alteration, the natural minerals are unlikely to be present in aerosols at the Hope Creek site. The Na-Al-SO_4 phase probably formed, either prior to or after deposition, by a particle-gas conversion reaction between sodium-and-aluminum-bearing aerosol particles and sulfuric acid captured as SO2 from the atmosphere. Naturally occurring Na-Al phases are also unlikely to be present as aerosols at the Hope Creek site. However, both a particulate (cryolite, Na_3AlF_6) and a gas-phase compound ($NaAlF_4$) are found in emissions from aluminum smelting operations that use the Hall-Heroult process for refining aluminum (Kvande and Drabløs, 2014). These could react with atmospheric sulfuric acid (also present in smelter emissions) to form the Na-Al-SO_4 phase observed by SEM. There is a large Al recycling and smelting company in Camden, NJ, 40 miles NE of the Hope Creek site. This company, State Metal Industries Inc., uses the Hall-Heroult method. It seems likely that the Na-Al-SO_4 phase observed in the dusts from the unused canister at Hope Creek can be sourced to reactions between Na-Al phases in Al smelter emissions and atmospheric SO_2 or sulfuric acid.

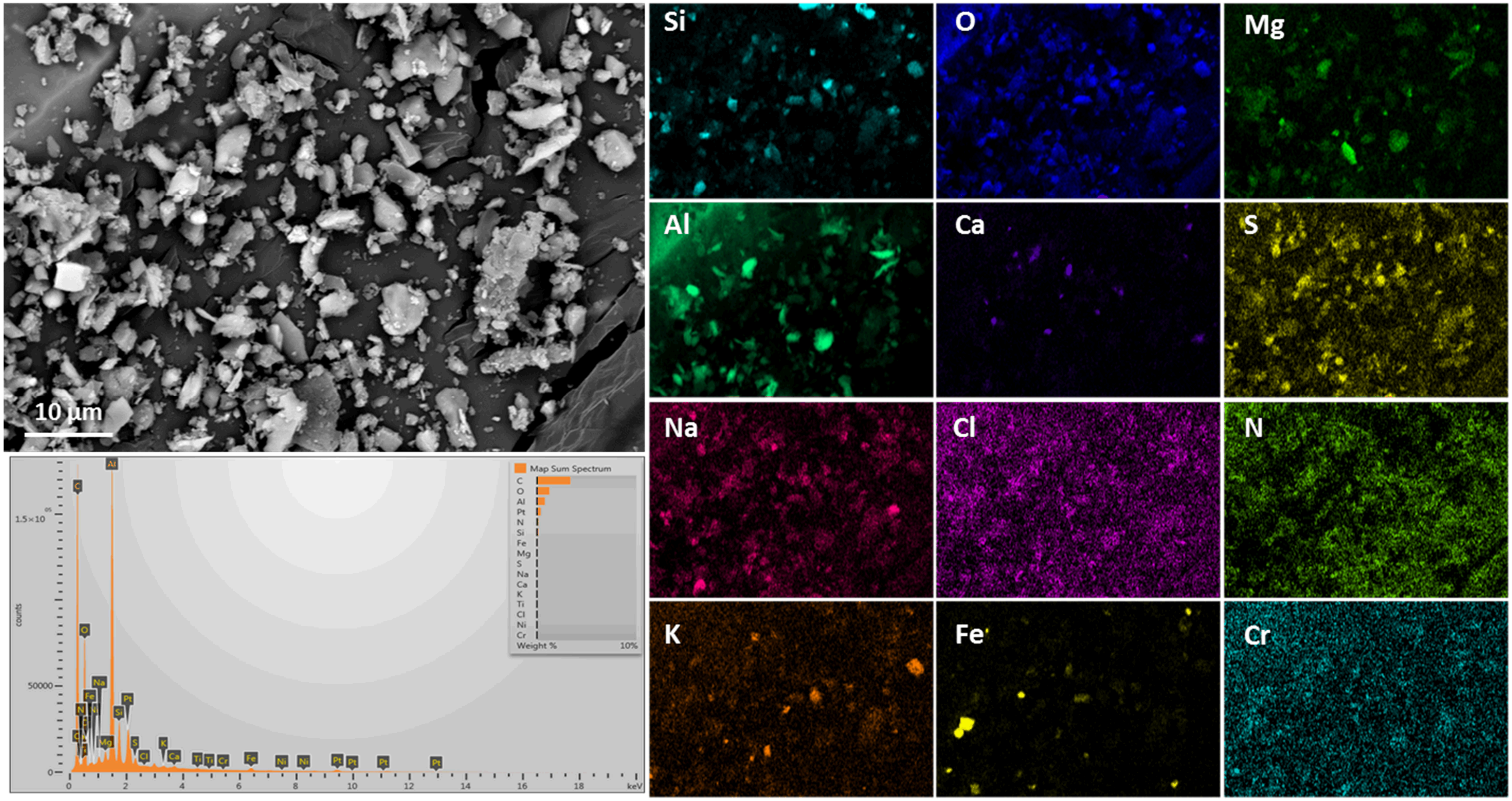

Figure 5. SEM image/EDS map #2 of sample 387-013, collected from the center of the FME cover. Grains are largely aluminosilicates, but note the abundance of SO_4 phases.

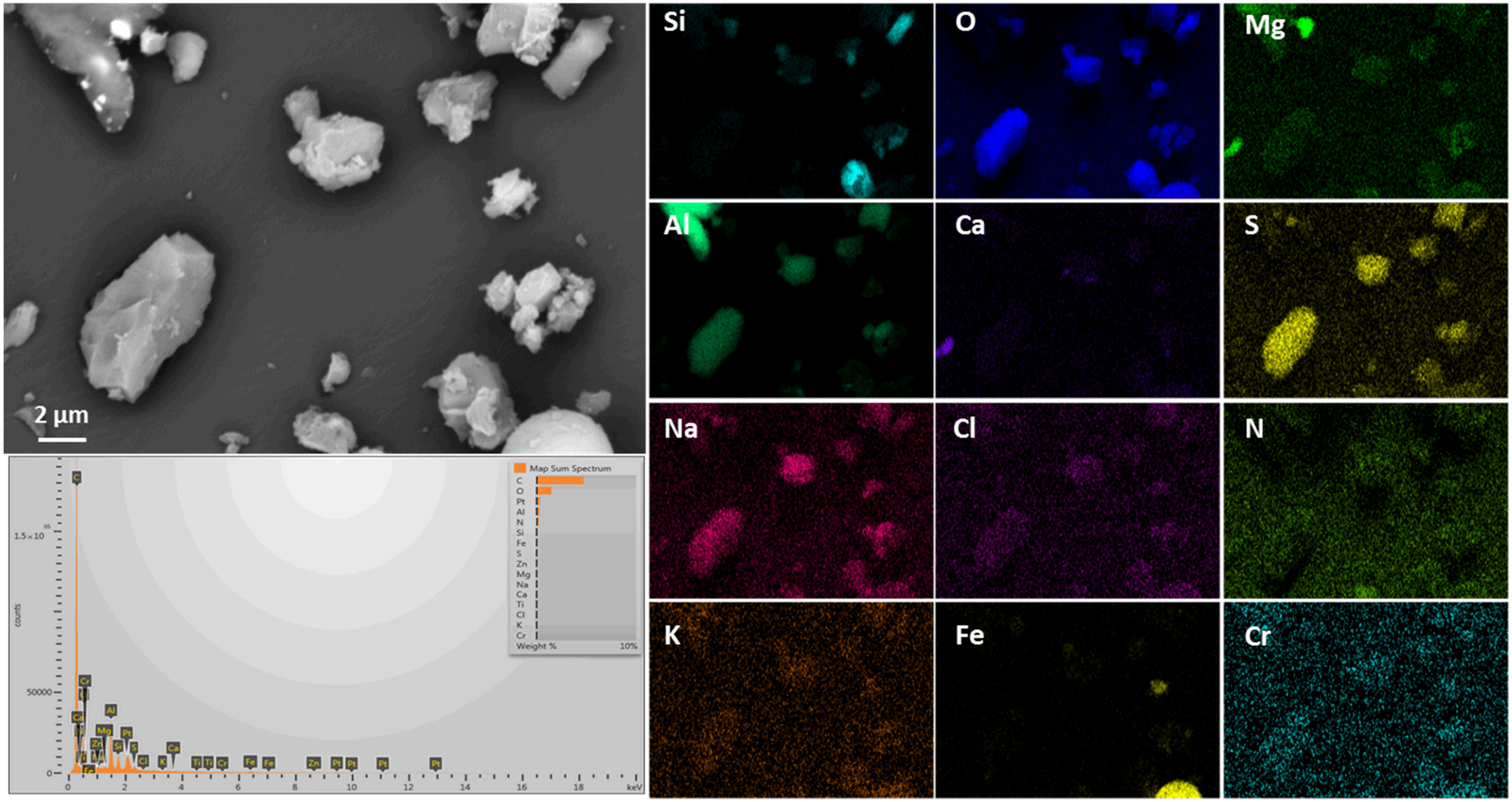

Figure 6. SEM image/EDS map #2 of sample 389-015, collected 1 foot from the edge of the FME cover. Magnified image of Na-Al-SO$_4$ phases.

2.2.3 Summary of SEM/EDS Analyses

Dust samples collected from the canister surfaces and from the FME covers differed greatly. Dusts from the canister surface were dominantly stainless steel particles generated during manufacturing of the canister. Environmentally derived particles—silicates/aluminosilicates and salts--were sparse. Dust loads on the canister surface were light, for both the side and the top. This is not unexpected, as the canister lid was covered by the FME cover during the one-year storage interval. Although the FME covers were washed by rain prior to sampling, it is clear that the dust loads were heavier, and that the particles were dominantly environmentally derived. Salts were present despite the rain, although it is not clear if they are representative of what was present prior to the rainfall.

For both the canister and FME cover samples, chloride and nitrate salts were rare; Ca-Mg carbonate and Ca-carbonate, were present in minor amounts. The most abundant salts were sulfates, consisting largely of Ca-SO_4 and Na-Al-SO_4, although Na-SO_4 and K-SO_4 phases were also present. Most of these, while occurring naturally (generally in arid climates), are unlikely to be present as detrital grains at the Hope Creek site, and probably form by particle-gas conversion reactions involving chloride and nitrate salts, and atmospheric SO2 or sulfuric acid. If there is sufficient relative humidity that the surfaces of salt particles have a deliquesced or adsorbed water film, then sulfuric acid will react with the minerals, transforming carbonates, chlorides, and nitrates to sulfates via reactions such as:

$$2NaCl(s) + H_2SO_4(aq) \leftrightarrow Na_2SO_4(s) + 2HCl(g)$$

$$2NaNO_3(s) + H_2SO_4(aq) \leftrightarrow Na_2SO_4(s) + 2HNO_3(g)$$

$$CaCO_3(s) + H_2SO_4(aq) \leftrightarrow CaSO_4(s) + CO_2(g) + H_2O$$

These reactions are schematic in that bisulfate phases or hydrated sulfates may form instead, and H2SO4(aq) is fictive, representing dissociated H^+ and HSO_4^-/SO_4^{2-}. The reactions will proceed as written as long as the acid gas partial pressures generated by the solution are higher than the levels in the atmosphere. This is generally true because of the acidification of the brine by reaction with SO2; the equilibrium acid gas partial pressures are higher at low pH. Elevated temperatures also elevate acid gas partial pressures.

To form the observed Na-Al-SO_4 phase, either cryolite (Na_3AlF_6) or $NaAlF_4$ gas in aluminum smelter emissions could react via:

$$Na_3AlF_6(s) + 3H_2SO_4(aq) \leftrightarrow NaAl(SO_4)_2(s) + Na_2(SO_4)(s) + 6HF(g)$$

$$NaAlF_4(g) + 2H_2SO_4(aq) \leftrightarrow NaAl(SO_4)_2(s) + 4HF(g)$$

These reactions probably occurred while the salts were aerosols, prior to deposition onto the canister surface.

Reactions involving ammonium sulfate are also possible. If RH values are sufficiently high to allow a thin film of brine to form on the particle surfaces, then conversion reactions with ammonium sulfate are also possible. For example with a water layer as a medium for reaction, the following reaction could occur:

$$2NaCl(s) + (NH_4)_2SO_4(s) \leftrightarrow Na_2SO_4(s) + 2HCl(g) + 2NH_3(g)$$

When acid degassing alone occurs, the pH of the remaining solution rises, and the generation rate of acid gases drops—the reaction is self-limiting. But coupled acid and ammonia degassing does not result in a rise in pH, and the degassing rate can be maintained. Hence, these reactions can result in the rapid loss of chloride and nitrate from deliquesced brines. Similar reactions can be written for many of the other salts discussed above. All of these reactions convert atmospheric aerosols into sulfates, either prior to deposition or afterwards on the canister surface.

2.3 XRF Analyses

XRF analysis was used to quantify element concentrations on the pads. The XRF was capable of mapping the filters and pads with a spot to spot resolution of 25 μm, providing spatial information on the scale of the filters. This information provides a link between the SEM data, which is confined to small areas on the sample surface, and the chemical analysis, which does not discriminate spatially, but rather provides an averaged composition for all the phases present. Moreover, the analysis provides element ratios which may be useful in estimating concentrations of some insoluble elements.

Only the dry pad samples from the canister surface were analyzed, as it was anticipated that the FME cover would have been rinsed free of dust by the rain (later SEM analyses showed that this was not entirely true). The XRF analyses provided little information beyond that provided by SEM and EDS analyses. The X-ray fluorescence patterns for the dry pads showed that the samples were uniformly enriched in the components of stainless steel relative to the blank pad, consistent with the abundance of steel particles in the dust (Figure 7). In addition to the components in stainless steel, samples from top of the canister showed a slight enrichment in Si, S, and K. This suggests that small amounts of dust of terrestrial origin, silicates and sulfates, were preferentially deposited on the top of the canister relative to the sides, even though the FME cover was in place.

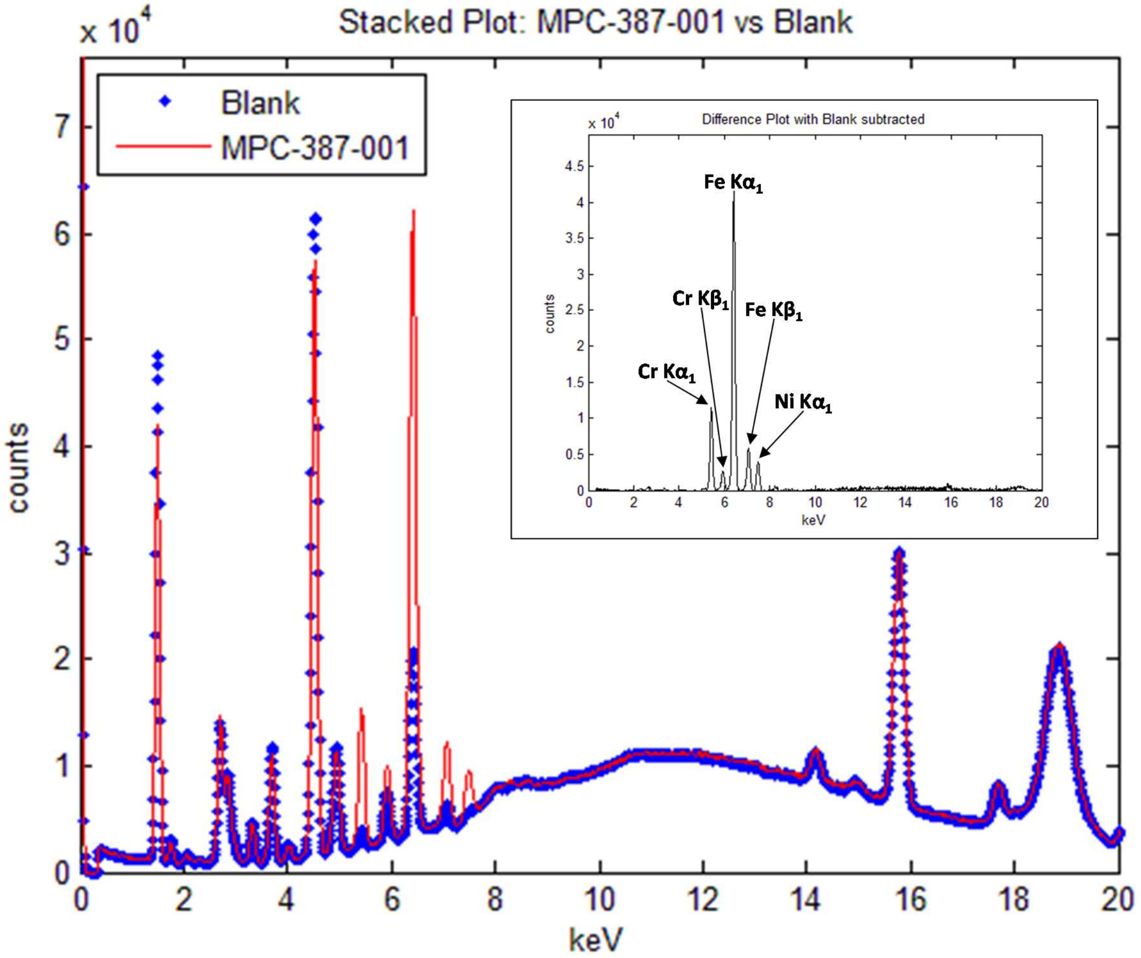

Figure 7. XRF pattern for 387-001 and the Blank pad. The inset shows the blank-subtracted pattern. Stainless steel components are enriched in the dust on the pad.

2.4 Chemical Analysis

The methods used for chemical analysis of the SaltSmart™ and dry pad samples from Hope Creek and Diablo Canyon are described in Bryan and Enos (2014b). The results of the soluble salt analyses for the SaltSmart™ are presented below. Although chemical analysis of leachates from the dry pads was carried out, solutes that leached from the matrix of the dry pads overwhelmed any contribution from the adhering dust, so those results are not presented.

Nine SaltSmart™ sensors were analyzed from the Hope Creek unused canister (MPC-387). Although there was no discoloration on the wicks, concentrations of soluble salts were significant in the SaltSmarts™, as suggested by the conductivity measurements recorded on-site. Measured compositions for the soluble salts extracted from the SaltSmart™ sensors are provided in Table 2, in units of µg per sample. Also shown in this table are several SaltSmart® blanks run at Sandia; see Bryan and Enos (2014b) for a description of these samples. The blanks are included here to allow better assessment of the significance of the measured values for the unknowns. Blank-subtracted concentrations for the samples, calculated using average blank values, are provided in Table 3 and in Table 4 in µg/sample and microEquivalents (µEq) per sample, respectively (where Eq = (mass(g)/mole wt.) × ion charge), where an Equivalent is . As with the previous SaltSmart™ analyses of soluble salts from canister surfaces, the charge balances are poor; the soluble salts measured from the unused canister are deficient in anions. It seems likely that this is because a significant fraction of the soluble species were present as carbonates (as confirmed by SEM), and carbonate was not included in the chemical analyses.

The results for the unused canister samples are generally consistent with those from Hope Creek in-service canisters (MPC-143 and MPC 144); sulfate and nitrate are the most abundant anions, but some chloride is present, and the most abundant cations are Ca^{2+} and Na^{+} (Bryan and Enos 2014b) In terms of amount of soluble salts present, the samples from the unused canister contain more soluble salts and chloride than the samples from sides of the in-service canisters, but less than the samples from the tops of the in-service canisters. The estimated chloride surface loadings, calculated assuming 100% extraction efficiency by the SaltSmart™ sensors and a surface contact area of 3 cm^2, are given in Table 5. Chloride surface loadings range from 6 to 14 mg/m^2.

The element concentrations in the blanks and samples are plotted against Ca, the most abundant element in the blanks, in Figure 8. Anion and cation concentrations in the samples are much higher than those in the blanks for all solutes except for phosphate, indicating that a large component of each solute came from the dust. This is true for all samples, even those that were collected from the FME cover. For phosphate, the sample and blank ranges overlap completely, suggesting that the phosphate was largely, if not entirely, leached from components in the SaltSmart™ sensors, and does not represent a component in the soluble salts.

Data for samples collected from the in-service canisters MPC-143 and MPC-144 (see Table 9, Bryan and Enos 2014b) are plotted with the blanks and samples from the unused canisters (MPC-387 and MPC-389) in Figure 9 and Figure 10. Despite the much longer storage times for the in-service canisters, solute concentrations tended to be lower on the sides of the in-service canisters than on the sides of the unused canister and FME covers, plotting on a trend between the blanks and the unused canister samples. The three samples from the tops of the in-service canisters are enriched in many elements relative to samples from the unused canisters (Figure 9).

The consistent differences in salt load for the in-service and unused canister sides suggest that thermal effects are being observed. For in-service canisters, thermally driven airflow within the annulus between the canister and overpack may be rapid enough to limit dust deposition. In addition, thermophoresis, or thermally-driven rejection of dust from the heated surface of the canister, may also be limiting deposition relative to the unheated, unused canister. The heavy loads on the tops of the in-service canisters are likely due to gravitational settling in the “dead air” above the canisters in the overpack. It is notable that the canister-top samples fall on a similar trend as the other samples for most species, but not for those that are most likely to be affected by ammonium mineral decomposition— NH_4, Cl^-, and NO_3^-. The canister top locations were the hottest surface locations, and the relative depletion of these species may indicate thermally-driven decomposition occurred.

Table 2. Ion concentrations in the Hope Creek SaltSmart™ samples (µg/sample).

Sample #	**Location**	**Na^+**	**K^+**	**Ca^{2+}**	**Mg^{2+}**	**NH_4^+**	**F^-**	**Cl^-**	**NO_3^-**	**PO_4^{3-}**	**SO_4^{2-}**	**SUM**
387-002	Side, 1' from base	7.0	2.2	7.5	0.67	4.1	nd	2.8	9.2	*0.19*	7.2	40.8
387-004	Side, 1' from top	13.6	2.0	7.6	0.62	5.2	*0.19*	3.0	8.4	0.57	12.0	53.1
387-006	Lid, 1' from edge	9.2	2.3	10.6	0.82	2.7	nd	2.0	11.6	0.41	9.5	49.2
387-008*	Lid, center	na	na	na	na	na	nd	4.2	14.9	1.79	10.0	30.9
387-010	Side, 5' from base	6.0	1.7	9.0	0.86	3.3	nd	1.7	6.2	1.6	7.5	37.7
387-012	FME cover, 1' from edge	10.4	2.3	8.9	0.62	4.3	nd	2.4	6.2	0.52	8.7	44.3
387-014	FME cover, center	9.5	3.4	6.9	0.67	4.3	nd	1.9	9.5	0.96	9.4	46.5
389-016	FME cover, 1' from edge	6.4	1.3	6.4	0.75	4.4	nd	2.1	4.4	1.1	8.2	35.2
387-017	FME cover, center	6.7	1.4	7.8	1.0	3.7	nd	2.2	5.9	0.85	9.3	38.8
B1-6	—	0.88	1.2	2.2	0.23	1.4	*0.10*	1.3	3.9	0.87	0.45	12.5
B1-8(1)	—	nd	0.23	1.2	0.15	1.4	0.53	0.42	*0.29*	*0.34*	*0.26*	4.8
B1-10	—	*0.01*	0.35	1.5	0.21	1.1	0.38	0.68	2.3	0.97	0.35	7.8
B1-12	—	0.33	1.0	1.3	0.19	1.2	*0.26*	1.2	2.2	0.91	0.33	8.9
B1-14	—	nd	*0.14*	1.1	0.16	1.2	0.32	0.44	0.92	1.29	*0.23*	5.8
B1-8(2)	—	nd	0.26	1.4	0.27	1.0	0.38	0.39	1.3	nd	0.52	5.5
SS-Bl-8 min-1	—	nd	nd	1.3	0.20	1.1	nd	0.36	1.6	nd	0.58	5.1
SS-Bl-8 min-2	—	nd	nd	1.2	0.18	1.5	nd	0.69	0.9	0.5	0.25	5.2
SS-Bl-15 min	—	nd	nd	1.5	0.49	5.7	0.24	0.67	1.1	1.6	1.68	12.9

* Sample spilled. Too little sample remained to analyze both cations and anions, so only anions were analyzed.

Table 3. Ion concentrations in the Hope Creek SaltSmart™ samples (µg/sample), after subtracting average blank values.

Sample #	**Location**	**Na$^+$**	**K$^+$**	**Ca^{2+}**	**Mg^{2+}**	**NH$_4^+$**	**F$^-$**	**Cl$^-$**	**NO$_3^-$**	**PO$_4^{3-}$**	**SO$_4^{2-}$**	**SUM**
387-002	Side, 1' from base	6.9	1.8	6.1	0.4	2.3	nd	2.1	7.6	nd	6.7	34.0
387-004	Side, 1' from top	13.4	1.6	6.2	0.4	3.4	nd	2.4	6.8	nd	11.4	45.6
387-006	Lid, 1' from edge	9.1	2.0	9.2	0.6	1.0	nd	1.4	10.0	nd	9.0	42.1
387-008*	Lid, center	na	na	na	na	na	nd	3.6	13.3	nd	9.5	26.3
387-010	Side, 5' from base	5.8	1.4	7.5	0.6	1.6	nd	1.0	4.6	0.8	7.0	30.3
387-012	FME cover, 1' from edge	10.3	1.9	7.5	0.4	2.6	nd	1.7	4.6	nd	8.2	37.1
387-014	FME cover, center	9.3	3.0	5.5	0.4	2.5	nd	1.3	7.9	0.2	8.9	39.0
389-016	FME cover, 1' from edge	6.3	1.0	5.0	0.5	2.7	nd	1.4	2.8	0.3	7.7	27.7
387-017	FME cover, center	6.5	1.0	6.4	0.8	2.0	nd	1.5	4.3	0.0	8.8	31.3

Table 4. Ion Concentrations in the Hope Creek SaltSmart™ Samples (µEq/sample) After Subtracting Average Blank Values.

Sample #	**Location**	**Na$^+$**	**K$^+$**	**Ca$^+$**	**Mg$^+$**	**NH$_4^+$**	**F$^-$**	**Cl$^-$**	**NO$_3^-$**	**PO$_4^{3-}$**	**SO$_4^{2-}$**	**Cat. Sum**	**An. Sum**	**Chg. Bal. Error**
387-002	Side, 1' from base	3.0E-01	4.6E-02	3.1E-01	3.6E-02	1.3E-01	nd	5.9E-02	1.2E-01	nd	1.4E-01	0.81	0.32	43.4
387-004	Side, 1' from top	5.8E-01	4.2E-02	3.1E-01	3.2E-02	1.9E-01	nd	6.6E-02	1.1E-01	nd	2.4E-01	1.16	0.41	47.3
387-006	Lid, 1' from edge	3.9E-01	5.1E-02	4.6E-01	4.8E-02	5.4E-02	nd	3.8E-02	1.6E-01	nd	1.9E-01	1.01	0.39	44.5
387-008*	Lid, center	na	na	na	na	na	nd	1.0E-01	2.1E-01	nd	2.0E-01	—	0.51	—
387-010	Side, 5' from base	2.5E-01	3.6E-02	3.8E-01	5.2E-02	8.6E-02	nd	2.8E-02	7.4E-02	2.4E-02	1.4E-01	0.80	0.27	49.6
387-012	FME cover, 1' from edge	4.5E-01	4.9E-02	3.7E-01	3.2E-02	1.4E-01	nd	4.7E-02	7.5E-02	nd	1.7E-01	1.04	0.29	56.1
387-014	FME cover, center	4.1E-01	7.8E-02	2.7E-01	3.6E-02	1.4E-01	nd	3.6E-02	1.3E-01	5.1E-03	1.9E-01	0.93	0.35	45.0
389-016	FME cover, 1' from edge	2.7E-01	2.5E-02	2.5E-01	4.3E-02	1.5E-01	nd	4.1E-02	4.5E-02	1.0E-02	1.6E-01	0.74	0.26	48.5
387-017	FME cover, center	2.8E-01	2.6E-02	3.2E-01	6.6E-02	1.1E-01	nd	4.3E-02	6.9E-02	1.5E-03	1.8E-01	0.80	0.30	46.1

* Sample spilled. Too little sample remained to analyze both cations and anions, so only anions were analyzed.

Table 5. Measured chloride concentrations on the unused canister and FME cover (mg/m^2).

Sample #	Location	Cl^-, mg/m^2
387-002	Side, 1' from base	9.2
387-004	Side, 1' from top	10.1
387-006	Lid, 1' from edge	6.8
387-008	Lid, center	14
387-010	Side, 5' from base	6
387-012	FME cover, 1' from edge	7.8
387-014	FME cover, center	6.5
389-016	FME cover, 1' from edge	7.1
387-017	FME cover, center	7.3

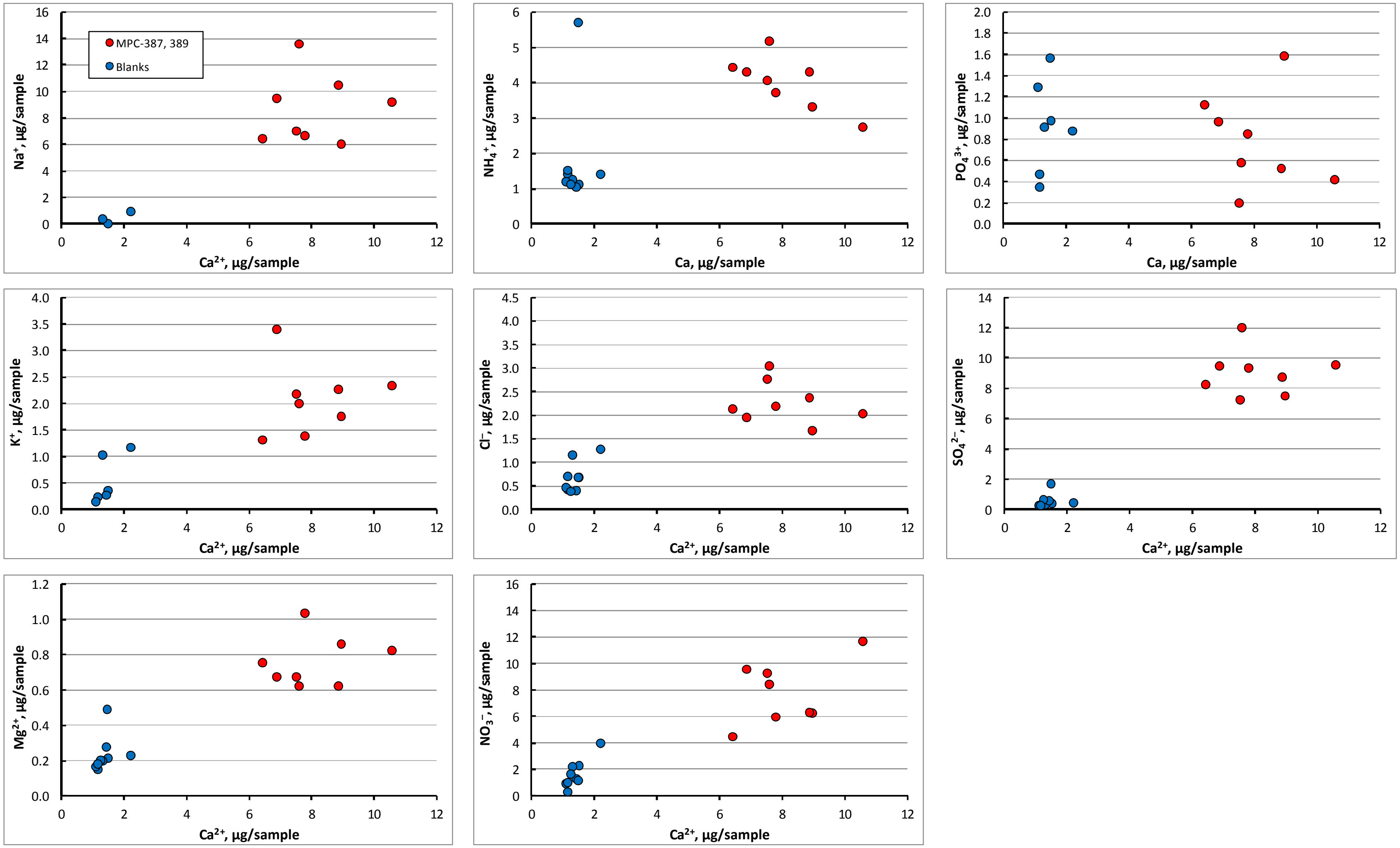

Figure 8. Plots of Ca^{2+} vs. other species in the unused canister and FME cover samples (MPC-387 and MPC-389) and the blanks.

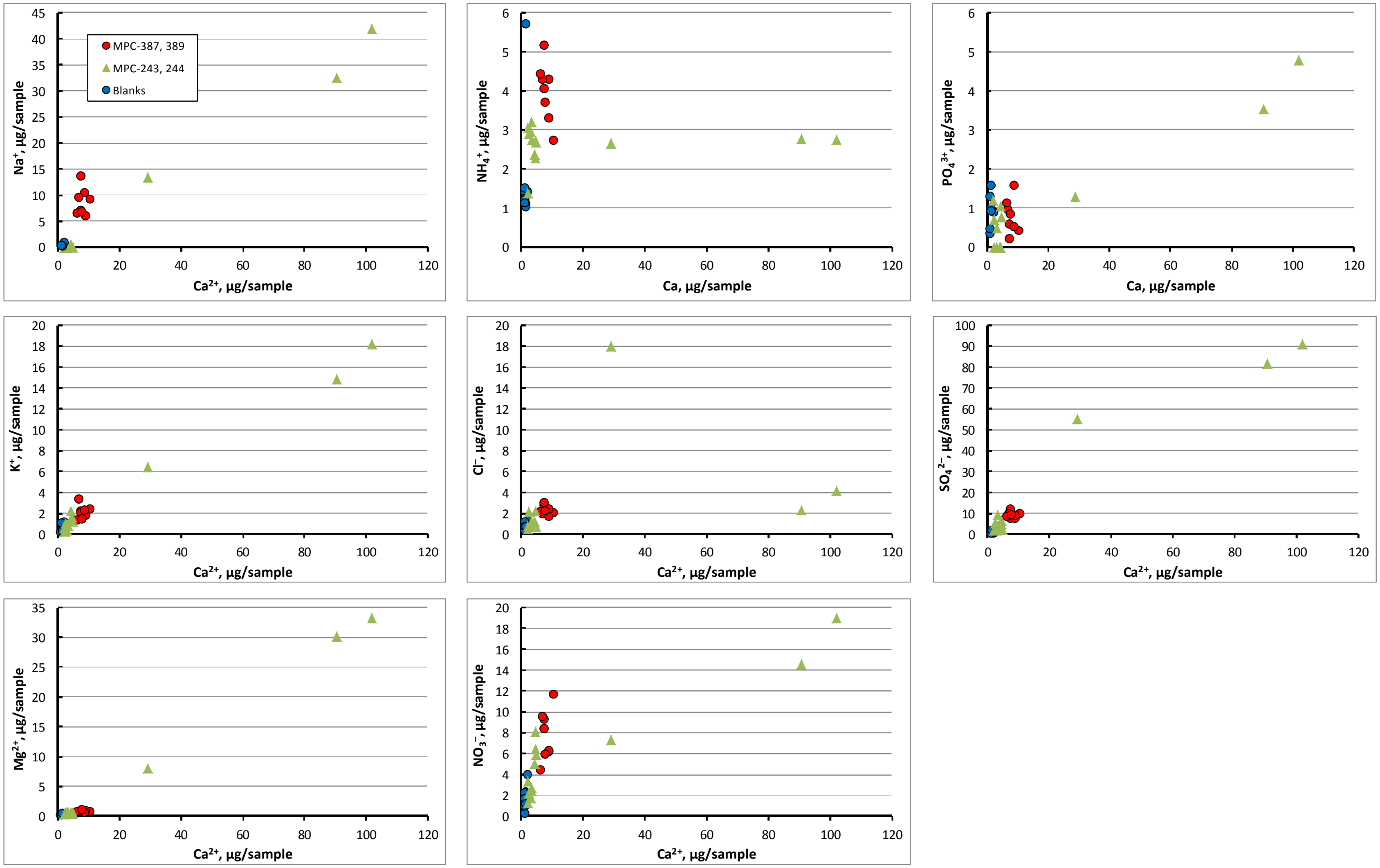

Figure 9. Plots of Ca^{2+} vs. other species in the unused canister and FME samples (MPC-387 and MPC-389), in-service canister samples (MPC-143 and MPC-144), and blanks. See Figure 10 for expanded views of the lower range of the graphs.

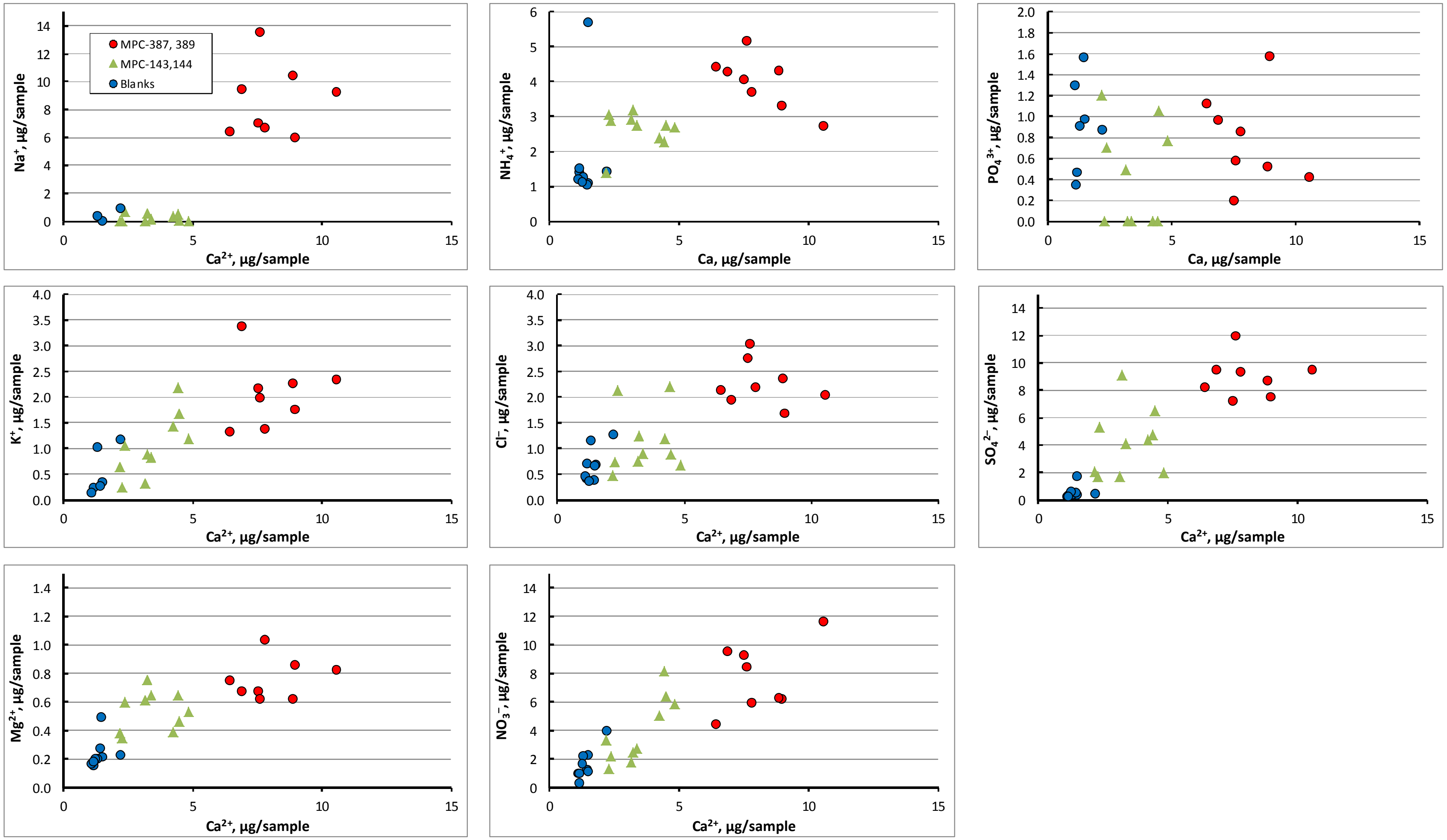

Figure 10. Plots of Ca^{2+} vs. other species in the unused canister and FME samples (MPC-387 and MPC-389), in-service canister samples (MPC-143 and MPC-144), and blanks. Graphs are expanded plots of the lower corners of graphs shown in Figure 9.

2.5 Summary of Hope Creek Unused Canister Dust Analyses

In November, 2013, EPRI directed the sampling of dusts on the surface of in-service SNF storage canisters at the Hope Creek ISFSI, from canisters in service for 7 years. The samples from the Hope Creek ISFSI were characterized by Sandia National Labs (Bryan and Enos, 2014). In July, 2014, EPRI went back to the Hope Creek facility and sampled dust on the surface of an unused canister that had been stored in an overpack at the site for approximately one year. Since the canister was empty, and had no heat load, convective airflow through the overpack was very limited, and it was anticipated that dust loads on the canister surface would be very light. The dust compositional data for a cold, unused canister complements that from dust on the hot in-service canisters, potentially allowing evaluation of the effects of temperature on the salt compositions. The Foreign Material Exclusion (FME) cover that had been on the top of the canister during storage, and a second recently-removed FME cover, were also sampled. This report summarizes the results of analyses of dust samples collected from the unused Hope Creek canister and the FME covers.

The sample types collected were similar to those described previously for the Hope Creek and Diablo Canyon sampling episodes (Bryan and Enos, 2014). Both wet and dry samples of the dust/salts were collected, using SaltSmart™ sensors and Scotch-Brite™ abrasive pads, respectively. At SNL, the wet samples were analyzed by chemical analysis to determine the composition and abundance of soluble salts present. The pads containing the dry dust were removed from the stainless steel backing plates and analyzed by X-ray fluorescence to obtain bulk chemical compositions. Then, a small portion of the sponge was removed and retained for SEM analysis. The remaining sponge was washed thoroughly with deionized water and the leachate collected, filtered, and analyzed for soluble salts. The pads were washed, and a tiny amount of insoluble residue was collected; however, the sample size was too small for bulk analysis of the residue.

As discussed in the previous section, the dust samples from the surface of the unused canister at Hope Creek were dominantly particles of stainless steel. Terrestrially-derived silicate/aluminosilicate dust particles and salts were also present, but at much lower abundances. The salts were dominantly sulfates, with rare chlorides and nitrates. The FME covers had been stored in the open for a few days prior to sampling, and a rainstorm had washed them. Sampling showed that despite the rain, dust and salts remained on the surface; however, the degree to which these salts represent what was there prior to the rain is unknown. The FME dusts were almost entirely silicates/aluminosilicates, but sulfate salts were also abundant; nitrate and chloride salts were rare, as were stainless steel particles. The abundance of stainless steel particles on the canister surface, and the relative paucity of stainless steel particles relative to environmentally-derived particles on the FME cover, strongly suggest that the stainless steel particles were created during the canister manufacturing process and were not deposited after relocation of the canister to the Hope Creek Site.

Sulfate salts dominated the assemblages on the canister and FME surfaces, and included Ca-SO_4, but also Na-SO_4, K-SO_4, and Na-Al-SO_4. It is likely that these salts were formed by particle-gas conversion reactions, either prior to, or after, deposition. These involve reaction of carbonate, chloride, or nitrate salts with atmospheric SO_2, sulfuric acid, or ammonium sulfate to form sulfate minerals. The Na-Al-SO_4 phase is unusual, and may have formed by reaction of Na-Al containing phases in aluminum smelter emissions with SO_2, also present in smelter emissions. An aluminum smelter is located in Camden, NJ, 40 miles NE of the Hope Creek Site.

3. EVALUATING SALT AND BRINE STABILITY ON THE SURFACE OF INTERIM STORAGE CANISTERS.

As noted in Section 1, one criterion for SCC is a corrosive environment, an aqueous environment that contains an aggressive chemical component that promotes metal corrosion. In the context of interim storage canisters stored within overpacks, a persistent aqueous solution can only form by deliquescence of salts deposited on the canister surface from air circulating though the overpack, and the aggressive component in the brines is chloride. The composition of atmospheric salt aerosols varies from storage site to storage site, and the composition of deposited salts may vary from the atmospheric salts. However, the potential for deposition of chloride-containing salts, at least at some sites, is high. In near-marine environments, chloride rich sea salts comprise a significant fraction of the atmospheric salt load. At inland sites, salt aerosols are generally chloride-poor; however, chloride salts associated with cooling tower emissions or with road salting during inclement winter weather could be carried into the ventilated overpack and deposited onto the canister.

However, while chloride-containing salts may be deposited on the canister, a variety of reactions can occur that can modify the composition of the deposited salts potentially making them less deliquescent, or even less corrosive if the reactions result in loss of chloride to the atmosphere. SNL has initiated experiments evaluating salt and brine stabilities on the surface of heated canisters and those are described here. In Section 3.1, typical marine and non-marine atmospheric aerosol compositions are reviewed. Section 3.2 describes reactions that could modify the composition of the salts, either while the salts are in the solid state, or once they have deliquesced. Section 3.3 describes the experimental setup used to evaluate salt and brine stability, and presents preliminary results.

3.1 Atmospheric Aerosol Compositions

Atmospheric aerosol particles have a number of natural sources, such as windblown surface soils/dust, sea spray, volcanic emissions, biosphere emissions, and the condensation of atmospheric gases. In addition, a significant fraction of the modern aerosol loading of the atmosphere results from anthropogenic activities such as fuel combustion. The chemical and physical properties of aerosol particles vary globally. A large fraction of ISFSIs are located in coastal regions, while others are located inland (Figure 11). Typical atmospheric aerosols for the two environments differ. Aerosols in the atmosphere over or near the oceans contain a large proportion of sea-spray-derived salt; sulfates formed by oxidation of sulfide species emitted by marine plankton also contribute to the soluble salt load. The aerosols over continental landmasses generally contain a larger proportion of terrestrial dusts/soil particles, particles derived from reactions of sea salt with atmospheric gases, and particles that have anthropogenic origins (Seinfeld 1986).

3.1.1 Near-Marine Aerosols

In near-marine settings, chloride-rich sea salts generated by wave action and evaporation of sea-spray can comprise a large fraction of aerosols. These salts reflect the composition of sea water, a typical example of which is provided in Table 6. Dominant ions in seawater are Na^+ and Cl^- with lesser amounts of Mg^{2+}, Ca^{2+}, K^+, and SO_4^{2-}. Sea spray evaporates to form salt aerosols, which upon deliquescence form highly concentrated chloride-rich brines (sea salt is approximately 55% Cl by weight). The predicted evolution of brine composition upon evaporation of sea water was modeled using the thermodynamic solubility and speciation modeling program EQ3/6 (Wolery and Jarek 2003) and the YMP Pitzer database (SNL 2007). In Figure 12, solute concentrations are plotted against the activity of water in the brine, which is equivalent to the relative humidity, expressed as a unit value. Inflections in the concentration curves occur when a mineral phase begins to precipitate. In Figure 13, the concentrations are given in terms of concentration factor, calculated as (original water mass)/(remaining water mass). The final concentration factor, at a RH of 28%, is 6060, meaning that 0.16 ml of water is left out of an original volume of 1 liter. On the concentration factor plot, solutes plot along a straight line as long as they are conserved in solution (do not precipitate out). Note that, while these plots show the evolution of seawater as it evaporates, deliquescence of sea-salts produces exactly the same fluid compositions as a function of RH. At low relative humidities, predicted deliquescent brine compositions are rich in Mg^{2+} and Cl^{-}, and somewhat less enriched in Br and B; these species plot as straight lines in Figure 13, as they are conserved in solution—that is, no mineral containing them is predicted to precipitate. (it should be noted that the YMP database is not qualified for use to predict borate species and contains few borate salts, so the enrichment in B may not be real). Other seawater components have been removed by precipitation, and are minor in the remaining brine.

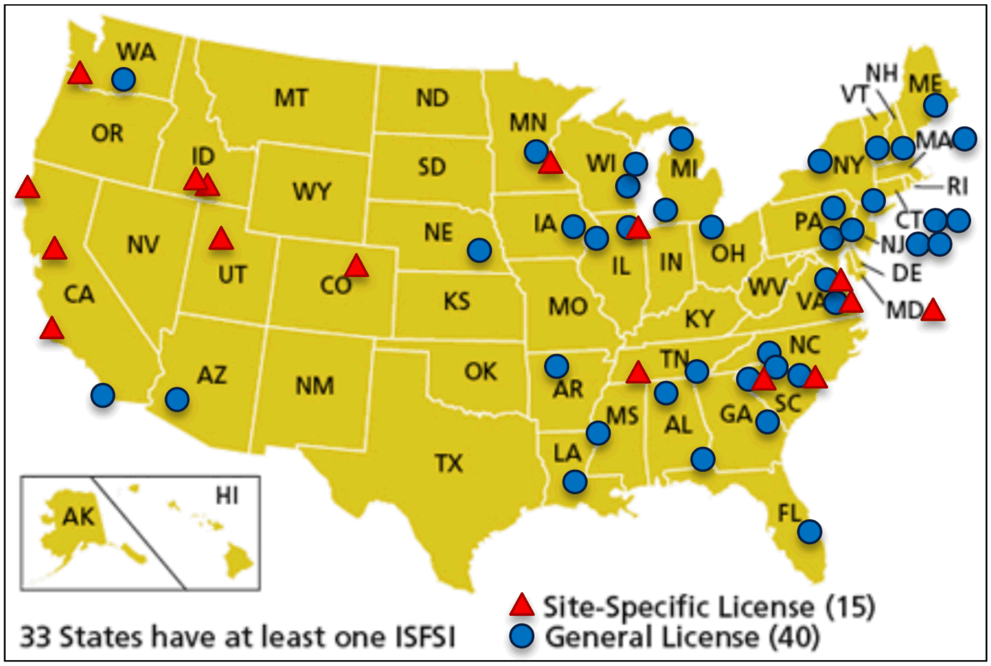

Figure 11. Location of licensed ISFSIs in the United States.

Table 6. Typical composition of seawater (McCaffrey et al. 1987)

Species	µg/ml
Na^{+}	11731
K^{+}	436
Mg^{2+}	1323
Ca^{2+}	405
Cl^{-}	21176
Br^{-}	74
F^{-}	—
SO_4^{2-}	2942
BO_3^{3-}	—
HCO_3^{-}	—
pH	8.2

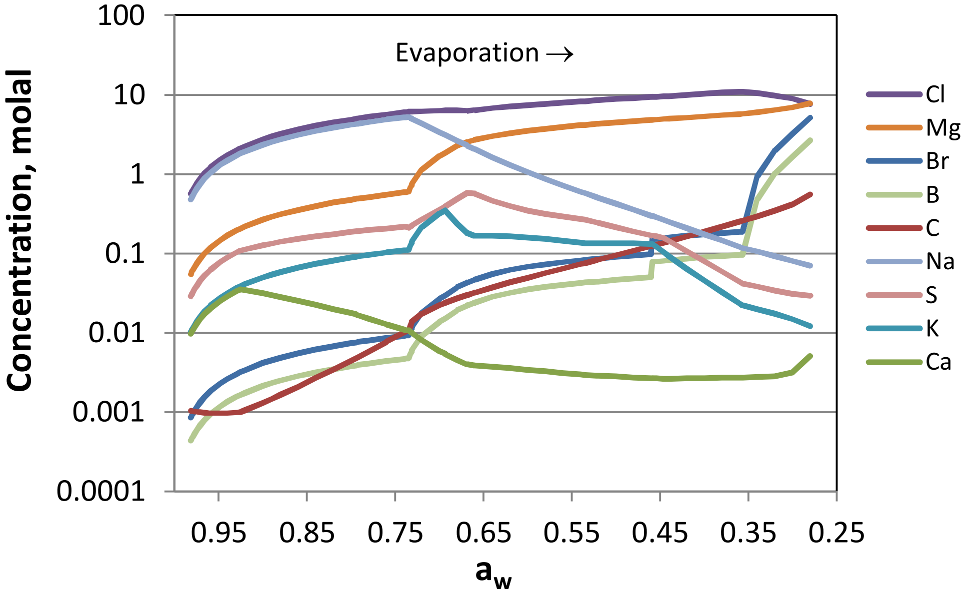

Figure 12. Evaporation of seawater. Predicted brine composition as a function of a_w.

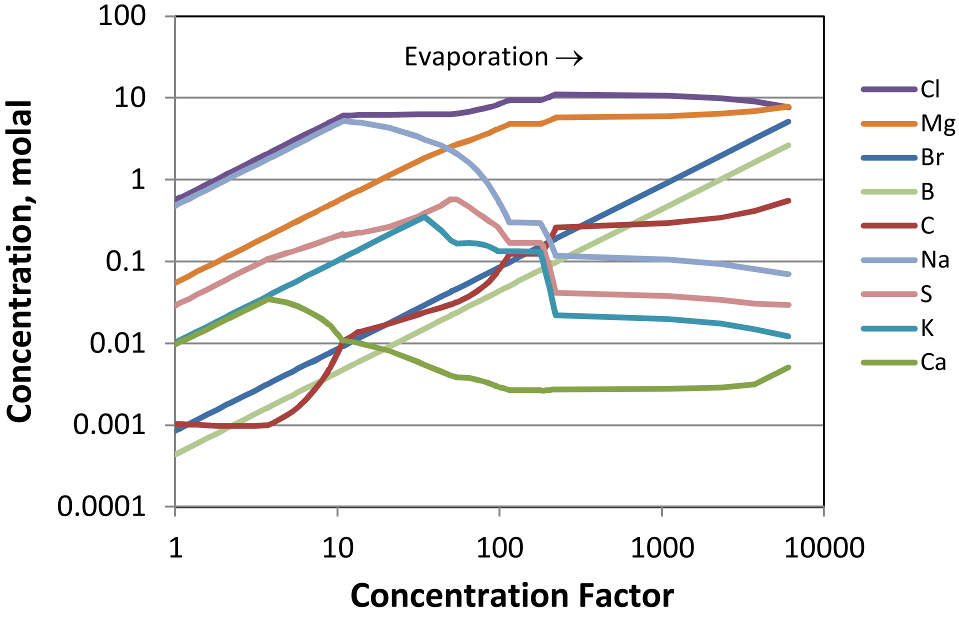

Figure 13. Evaporation of seawater. Predicted brine composition as a function of concentration factor.

It is mineral precipitation that ultimately controls the relative proportion of species in the evaporating brine. Salt minerals that are predicted to precipitate out during evaporation are shown in Figure 14. In order of occurrence, calcite ($CaCO_3$) precipitates first, and then gypsum ($CaSO_4{:}2H_2O$), which converts to Anhydrite ($CaSO_4$) at a concentration factor of about 9. Halite (NaCl) precipitates at a concentration factor of about 11. Other minerals precipitate, and in many cases redissolve, as the seawater evaporates. The final salt assemblage at dryout consists mostly of halite, with minor amounts of Bischofite ($MgCl_2{:}6H_2O$) and Kieserite ($MgSO_4{:}2H_2O$) and trace amounts of Anhydrite, Carnallite ($KMgCl_2{:}6H_2O$), and Hydromagnesite ($Mg_5(CO_3)_4(OH)_2{:}4H_2O$). As sea-spray aerosols dry out, these salts are precipitated, and salts, or a mixture of salts and brine, may be deposited on the canister surface. As the RH rises over time, the salts redissolve and the composition of the deliquescent brine follows the path of evaporation in reverse order. It is the highly deliquescent $MgCl_2{:}6H_2O$ that is believed to control the deliquescence behavior of sea salts; determining when an aqueous phase is present.

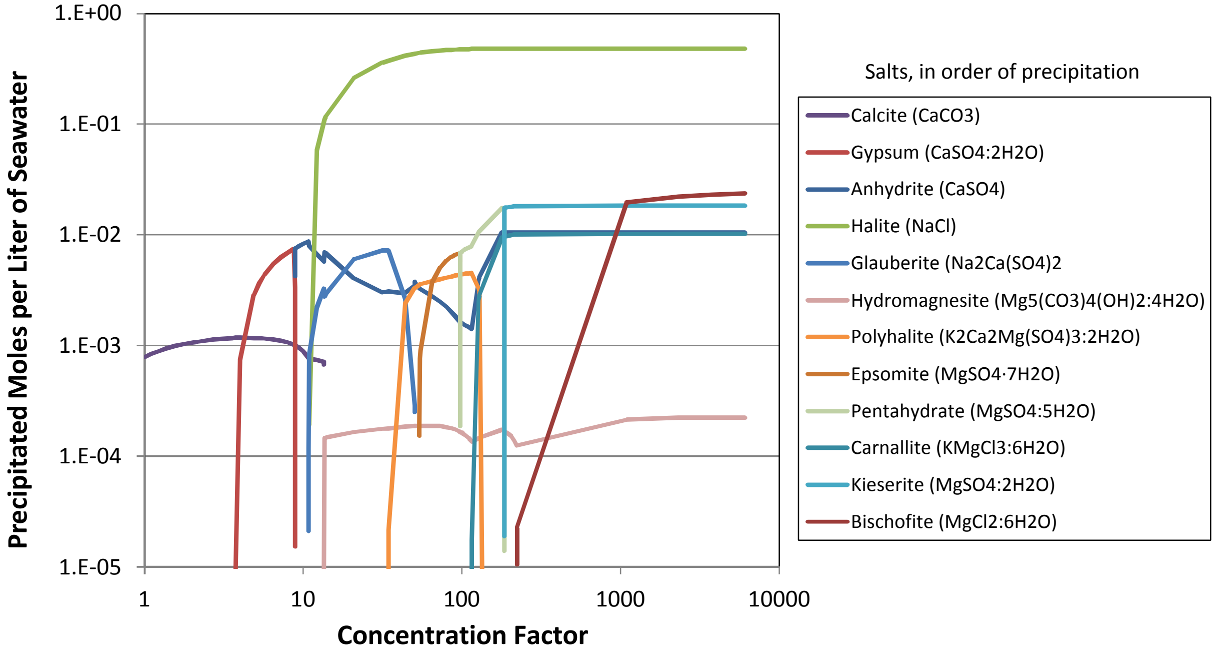

Figure 14. Evaporation of Seawater. Predicted salt phases as a function of concentration factor.

The occurrence of sea-salt aerosols on SNF dry storage canisters was recently confirmed, when sea-salt aggregates were observed in dust samples collected from canister surfaces at the Diablo Canyon ISFSI (Figure 15).

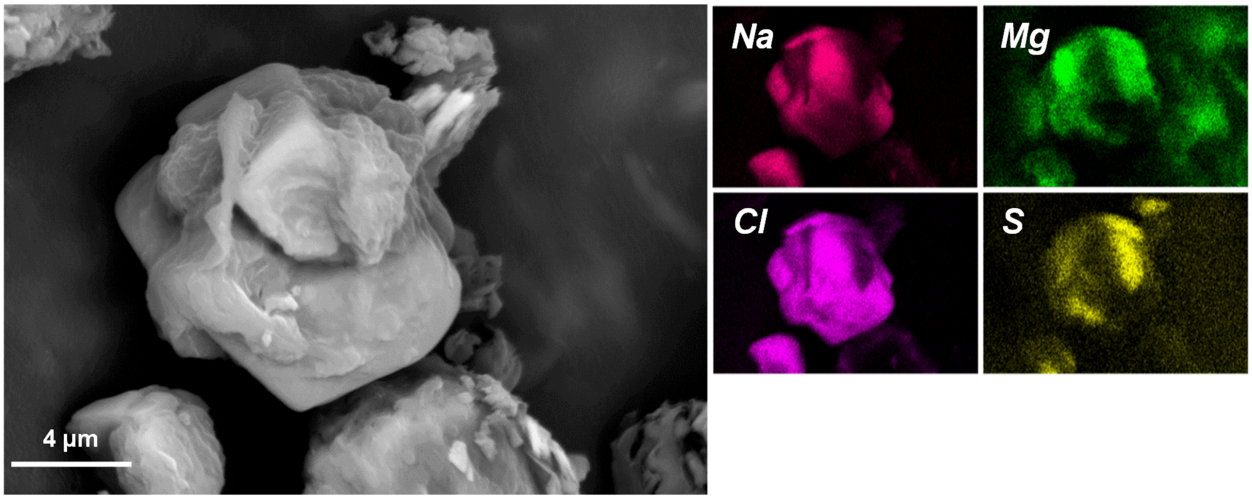

Figure 15. Sea-salt aerosols in dust collected from the surface of an in-service dry storage canister at the Diablo Canyon ISFSI.

3.1.2 Inland Aerosols

Nitrate and sulfate salts typically dominate the soluble fraction of atmospheric aerosols over continental landmasses, with the most common cations being ammonium and sodium (Seinfeld 1986; Malm et al. 2003; Rossi 2003). Most atmospheric ammonia is anthropogenic in origin, being produced by hydrolysis of urea present in livestock wastes and by offgassing of ammonia from fertilizers used in agriculture; other significant anthropogenic sources include biomass burning, human wastes, chemical and industrial processes, and fossil fuel combustion (Seinfeld 1986; Aneja et al. 2001; Anderson et al. 2003). The primary natural sources are oceanic emissions and emissions from soil and vegetation Like ammonia, atmospheric nitrate and sulfate currently have major anthropogenic sources, being emitted as acid gases, or reduced species that react with water to form acid gases, in power plant emissions. However, their anthropogenic emissions are decreasing in the U.S., due to pollution prevention programs. Atmospheric ammonia reacts readily with sulfate and nitrate acid gases in the atmosphere to form solid salts such as $(NH_4)_2SO_4$, $(NH_4)HSO_4$, and NH_4NO_3 (Seinfeld 1986; Rossi 2003). Because the ammonia originates almost entirely from the surface, the abundances of ammonium salts are higher in the lower troposphere, are becoming less abundant in the upper troposphere, and are nearly absent in the stratosphere (Rossi 2003). Near the surface, $(NH_4)_2SO_4$ and NH_4NO_3 dominate. At higher altitudes, the more acidic $(NH_4)HSO_4$ becomes important, while in the stratosphere, sulfate and nitrate exists as sulfuric and nitric acids. Fine atmospheric particles (particles with diameters less than 2.5 microns, also referred to as the PM2.5 fraction) primarily originate from gas condensation reactions such as those involving ammonia and sulfuric and nitric acids. Thus, one would expect most of the $(NH_4)_2SO_4$ and NH_4NO_3 to be present in the fine fraction.

Atmospheric salt compositions have been characterized extensively by national sampling programs. The State and Federal Interagency Monitoring of Protected Visual Environments (IMPROVE) program provides compositional data for the PM2.5 aerosol size fraction at over 150 sites through the continental US. The database does not include all solute species, but provides data for the most abundant soluble anions in atmospheric dusts, including nitrate, sulfate, and chloride. Data for five typical sites across the US were summarized in NRC (2014, Table 4-2), and are given in Table 7. These data illustrate the relative abundances of the anion species in typical continental aerosols.

The National Atmospheric Deposition Program (NADP) (2015) provides wet deposition, or rainout, data across the U.S. Precipitation scavenges aerosols from the atmosphere, and is often used to evaluate atmospheric aerosol compositions. Wet deposition data from a typical site in Iowa is given in Table 8, and confirm that ammonium is the dominant cation species. At this inland site, far from the ocean, Ca is the second most abundant cation. Nearer to the ocean, Na-sulfate and Na-nitrate are commonly abundant, formed by reactions between chloride-rich sea salts and sulfuric and nitric acids in the atmosphere (Section 3.2).

Table 7. Selected element concentrations in PM2.5 dust fractions from Five IMPROVE Sampling Sites.

Site	**NO_3^-, µg/m^3 Median (Range)**	**SO_4^{2-}, µg/m^3 Median (Range)**	**Cl^-, µg/m^3 Median (Range)**
Arendtsville, PA	0.5349 (0.0529 to 8.3000)	2.2702 (0.366 to 15.2673)	0.0253 (0.0002 to 0.3252)
Bondville, IL	1.1627 (0.0662 to 8.9192)	2.0517 (0.4084 to 9.0997)	0.0315 (0.0006 to 0.2855)
Great River Bluffs, MN	0.4869 (0.0145 to 16.106)	1.1351 (0.1649 to 8.3342)	0.0229 (0.0001 to 0.6104)
Great Smoky Mtns National Park, TN	0.1482 (0.0382 to 4.5818)	2.0497 (0.1252 to 7.0209)	0.0145 (0.0007 to 0.1657)
Phoenix, AZ	0.3837 (0.0638 to 5.9663)	0.7779 (0.1761 to 8.3342)	0.0841 (0.0028 to 1.0963)

Data from National IMPROVE network, summarized in NRC (2014), NUREG/CR-7170, Table 4-2.

Table 8. Composition of wet deposition from an Iowa NADP site.

Species	Rain Conc., µeq/L
NH_4^+	29.217
Na^+	2.045
K^+	0.511
Mg^{2+}	3.208
Ca^{2+}	16.766
Cl^-	1.975
NO_3^-	15.565
SO_4^{2-}	17.685

NADP (2015)

3.2 Processes Affecting Aerosol/Brine Compositions

Once deposited on the canister surface, several processes can affect the composition of deposited salts, or of the brine that can form when they deliquesce. Some of these can occur prior to deliquescence; others can only occur after a deliquescent brine has formed, or, at least, require the RH be sufficiently high that a thin adsorbed water film is present on the salt surface. Significant films of adsorbed water may be present below the deliquescence RH (RH_D) for a given salt, and probably explain why the limiting RH for corrosion (RH_L) is below the deliquescence RH for a given salt (this is discussed in further detail in Section 3.3.3.1).

For purposes of the discussion here, it is assumed that the RH_L represents the humidity at which adsorbed water films on salt surfaces become significant enough to support chemical reactions between the salt and other solid or gaseous phases present, while the RH_D refers to a somewhat higher RH at which a salt or assemblage of salts is in equilibrium with a bulk saturated solution of that salt or assemblage.

Reactions occurring prior to deliquescence.

Some salts are not thermally stable and prior to deliquescence can decompose, emitting gas species and therefore being removed from the surface of the storage canister. The salts most susceptible to thermal decomposition are ammonium salts, which are abundant at inland sites (Section 3.1.2). Prior to deliquescence, ammonium salts decompose via the following reactions:

$$NH_4Cl(s) \leftrightarrow NH_3(g) + HCl(g)$$

$$NH_4NO_3(s) \leftrightarrow NH_3(g) + HNO_3(g)$$

$$(NH_4)_2SO_4(s) \leftrightarrow 2NH_3(g) + H_2SO_4\ (g)$$

As ammonia degasses, there is concomitant loss of an acid gas species. Experiments with bulk salts show that ammonium chloride and ammonium nitrate reactions are very rapid even at moderately elevated temperatures (SNL 2008). At 100ºC, the reaction is complete within days or weeks; even at 50ºC, a large fraction of the minerals will be lost over years. Ammonium sulfate decomposition is much slower; it is complete in less than 1 year at 100ºC, but may persist with little loss at lower temperatures (SNL 2008). For fine particulates such as atmospheric aerosols, loss is rapid even at ambient temperatures—loss of nitrate due to volatilization of particulate ammonium nitrate from sampling filters is a widely recognized bias in atmospheric dust sampling (Zhang and McMurry 1992; Chang et al. 2000). It is evident that ammonium salts deposited on a hot dry storage container will decompose rapidly, taking a significant fraction of acid gas anions with them. The ratio of cations removed is a function of the identity of the salt phases—for atmospheric aerosols, most ammonium is associated with sulfate, and to a lesser degree, nitrate (Seinfeld 1986); however, if the small amount of chloride present in inland aerosols is present as ammonium salts, it will also be lost over time. If the rate of loss is more rapid that the rate of deposition, then there can be no accumulation of ammonium chloride on canister surfaces. Because the previous experiments were performed on bulk salts (SNL 2008), and we anticipate that finely dispersed salts will degas much more rapidly, SNL has evaluated decomposition rates for ammonium minerals as a function of temperature under essentially dry conditions (RH = 11-13%) (Section 3.3).

Other than ammonium salts, most inorganic salts are thermally stable (with the exception of dehydration reactions) at temperatures anticipated to occur on interim storage canisters surfaces.

Reactions occurring after dDeliquescence.

Once an aqueous solution is present either as a deliquescent brine or as an adsorbed water film, salts may react with gas phases in the atmosphere, or with other salt phases. Some of these reactions can result in degassing of chloride and other anionic components as mineral acids, and loss of those species from canister surfaces.

Possible exchange reactions with the atmosphere include acid degassing, equilibration with atmospheric CO_2, and coupled degassing of ammonium and acid gases. At low pH, concentrated, deliquesced brines will produce partial pressures of acid gases (HCl, HNO_3) that are higher than the concentrations in ambient air. The brines degas the acids, resulting in loss of Cl^- and NO_3^- from solution. The solution pH rises, and the acid gas partial pressures decrease until (1) they are equal to that of the ambient air and degassing ceases; or (2) a buffering reaction occurs which stabilizes the pH allowing continued acid degassing and loss of Cl^-/NO_3^-. One buffering reaction involves adsorption of CO_2 from the atmosphere and precipitation of carbonate. For a sodium-rich brine, this occurs only at high pH (>10), because of the high solubility of sodium carbonate phases. Because of the high equilibrium pH, acid degassing is likely to be inhibited before significant loss of anions occurs. For a magnesium-rich brine, saturation with magnesite and precipitation occurs between pH 6 and 7; at these values, acid gas partial pressures in equilibrium with the solution may still be higher than ambient values, and degassing will continue to occur. A second buffering reaction for Mg-rich brines is precipitation of Mg-hydroxy-chlorides. Because this reaction is internally buffered, it can occur rapidly under some conditions. At 150ºC, deliquesced $MgCl_2$ brine has been experimentally shown to rapidly convert to nondeliquescent $Mg(OH,Cl)_2$. While this temperature is excessive for long term interim storage, it does illustrate that acid degassing can potentially change brine compositions over the long term. The effect of acid degassing is always to raise the pH; if a buffering reaction such as precipitation of carbonate occurs such that the degassing reaction can go to completion, then the composition of the salt assemblage has changed, and dryout may also occur (SNL 2008). In field conditions, for salts deposited over a period of years or decades in a storage container experiencing exposure to large volumes of circulating air, it is likely that degassing will limit brine pH, and may result in precipitation of non-deliquescent Mg carbonate or hydroxyl-chloride. Note that in a laboratory corrosion test setting, these effects are minimized by rapid deposition of relatively large amounts of salt, and low rates of air exchange. Proper experiment design is critical to understanding the effects of these processes.

Salt deposition continues to occur after deliquescence, but the role of ammonium salts changes. Once a deliquescent brine is present, ammonium minerals will dissolve into it, and coupled ammonium/ acid degassing will occur. However, the identity of the cation lost is no longer a function of the original ion association in the deposited mineral. Instead, the brine will degas ammonia and acid gas cations in proportion to their equilibrium vapor pressure above the brine. This means that chloride deposited as any chloride salt will be degassed, if ammonium, deposited as any ammonium salt is present. For instance, assume that NaCl and $(NH_4)_2SO_4$ are deposited on the canister. Once deliquescence occurs, the following reaction can occur:

$$2NaCl(s) + (NH_4)_2SO_4(s) \leftrightarrow Na_2SO_4(s) + 2HCl(g) + 2NH_3(g)$$

where ammonia and HCl are degassed and lost from the canister surface. Similar reactions can be written for Mg-Cl_2 or Ca-Cl_2 phases or the equivalent NO_3^- phases, or even carbonate phases, all result in loss of the mineral acid and ammonia from the canister surface. These reactions may be very important in limiting chloride accumulation at inland sites, where ammonium salts are the dominant components of atmospheric aerosols.

Other reactions that may be important in limiting chloride buildup on canisters at inland sites are described in Section 2.2 and involve reactions of chloride and nitrate salts with atmospheric SO_2, or with sulfuric acid formed when SO_2 reacts with water, that result in degassing of HCl or HNO_3 and precipitation of a sulfate mineral. These reactions are likely to be most important in the mid Atlantic states, where atmospheric concentrations of SO_2 are elevated due to industrial activities. Evidence of these reactions has been observed in dust samples collected at the Hope Creek and Calvert Cliffs IFSIs (Section 2.2).

The soluble fraction of marine aerosols contains a significant amount of chloride (as might be expected, as sea salt is approximately 55% by weight Cl). However, even over the oceans, the composition of soluble aerosols has long been recognized to be deficient in chloride relative to sea salt (e.g., Hitchcock et al. 1980), implying the presence of a mechanism for the removal of chloride (or chlorine) from atmospheric particles. This is generally attributed to reactions of strong inorganic acids with sea salt, such as:

$$\mathrm{NaCl(s,\ aq) + HNO_3(g) \leftrightarrow NaNO_3(s,\ aq) + HCl(g)}$$

$$\mathrm{2NaCl(s) + H_2O + \tfrac{1}{2}O_2 + SO_2(g) \leftrightarrow Na_2SO_4(s) + 2HCl(g)}$$

In addition, there are a number of photochemically-mediated reactions with nitrous oxides that can transfer chloride from the solid to the gas phase (Rossi 2003).

Because of these reactions, as sea-salt aerosols in near-marine settings are blown inland, they become progressively enriched in sodium salts of nitrate and/or sulfate, originating from reactions on primary particles of sea salt (Wall et al. 1988; Malm et al. 2003). These reactions can be very efficient; for instance, coastal aerosols in Spain lose 24% (coarse particles) to 67% (fine particles) of their chloride prior to reaching the shoreline, and continue to convert to nitrates and sulfates at a rate ~11% per hour thereafter (Pio and Lopes 1998).

One criterion for chloride-induced SCC of interim storage canisters is the accumulation of chloride on the canister surface. Accumulation will largely be controlled by the rate of chloride deposition relative to that of processes which result in chloride loss through degassing. If the chloride-loss reactions can be shown to be sufficiently rapid, then chloride is unlikely to accumulate. At some sites, particularly inland sites, this approach, when combined with validating site-specific aerosol or dust compositional data, may be a rationale for screening SCC, or at least, increasing SCC inspection intervals.

3.3 Experimentally Evaluating Salt and Brine Stability

In order to evaluate salt and brine stability as a function of temperature and RH on a canister surface, SNL developed techniques to accurately deposit a finely dispersed coating of soluble salts on flat surfaces. These samples are exposed to controlled environments, and mass loss and compositional changes are monitored. As discussed above, for some salts, mass loss can occur by decomposition of the solid phase. For other salts, deliquescence, or at least the development of an adsorbed water film on the surface of the salts, is required before degassing, reaction with atmospheric gas species, or reaction with other salts contacting them can occur. These reactions may result in mass or compositional changes in the soluble salts or brine chemistry, or, if a salt species is completely converted or decomposed, changes in the RH_D, resulting in dryout.

To evaluate these processes, we first deposit salts in aqueous or alcohol-based solutions onto samples using an airbrush mounted to an automated X-Y stage. We simultaneously deposit salts onto a quartz-crystal microbalance (QCM) wafer and onto 2.5″ × 5″ metal coupons. The QCM wafers monitor the mass deposited, and are later used to monitor deliquescence and mass loss in the environmental chamber. The coupons have a much larger surface area, and are used to measure changes in salt composition due to exposure in the environmental chamber; this is done by leaching off the soluble salts and analyzing them by wet chemical methods.

The extent to which atmospheric exchange and degassing reactions can occur is dependent in many cases on the background concentration of gas species (ammonia, HCl, HNO_3) in the atmosphere. It is difficult to evaluate some of these processes, as the gas species concentrations are site-specific. However, other processes are less dependent upon background concentrations. For instance, ammonium salt aerosols are commonly assumed to be in equilibrium with the gas-phase species at any given location. They decompose and degas rapidly because of the difference between the temperature on the canister surface and the ambient temperature. Similarly, for Mg-chloride containing salt assemblages, precipitation of Mg

(OH, Cl) species or reaction and precipitation of Mg-carbonate buffers the acid gas partial pressures to levels above the background. So, these systems can be examined without having to match site-specific gas species concentrations, and SNL has begun experimental work to evaluate them.

3.3.1 Salt Deposition

Sea salt aerosols formed from evaporation of sea-spray are mostly in the >2.5 µm aerosol fraction, and can be up to ~20 µm in diameter (e.g., Figure 15). Continental salts, which generally form by condensation from atmospheric gases (e.g., ammonia and sulfuric acid) are commonly in the PM2.5 fraction. Because degassing and decomposition reactions will be strongly controlled by the surface area of the salt particles, it is important, when evaluating salt and brine stability, to evaluate the reactions using finely dispersed salts deposited on the surface of interest. In order to prepare samples for testing, Sandia has developed a salt deposition system that is capable of depositing finely dispersed salt films. This system consists of an airbrush mounted on a computer controlled X-Y stage. The airbrush is fed a salt-containing solution (commonly a 0.1 M aqueous solution or an alcohol-based solution) at a controlled rate using a syringe pump, although a gravity fed system may also be used. The X-Y stage then rasters the airbrush over the samples to be coated, and also over a quartz crystal microbalance (QCM), which monitors the surface load of salt deposited (Figure 16). Each pass of the airbrush is close enough to the previous pass that the cone of spray overlaps, and the passes are designed to overspray the targets to minimize edge effects. Using a 0.1 M aqueous solution, each coating is equivalent to approximately 2 $\mu g/cm^2$ (20 mg $salt/m^2$); more dilute solutions can be used make lighter coatings, and if a heavier coating is desired, multiple coatings are used. For the experiments described here, 100 $\mu g/cm^2$ (1 g/m^2) was deposited in 50 coats. An example of the salt coating produced using the spray system is shown in Figure 17. The deposited salts are present as dispersed particles, evenly coating the surface of the sample. Though not as small as most atmospheric aerosols, the deposited salts are in the range of 20-50 µm in diameter, and should be fine enough for use as analogs for atmospheric salt aerosols.

The salt deposition system is ideal for preparing samples for atmospheric corrosion testing, because it is capable of evenly depositing very thin films of salts over the surface of test coupons, at surface loads ranging from a few mg/m^2 to g/m^2.

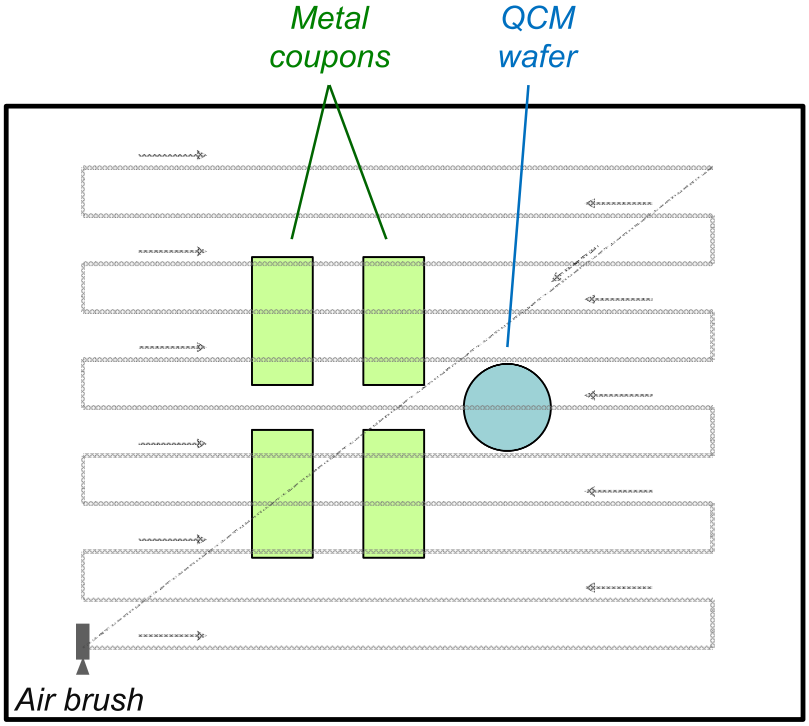

Figure 16. Schematic of salt deposition system. A computer-controlled X-Y stage rasters the airbrush over the samples, evenly depositing a salt film at a specified surface loading.

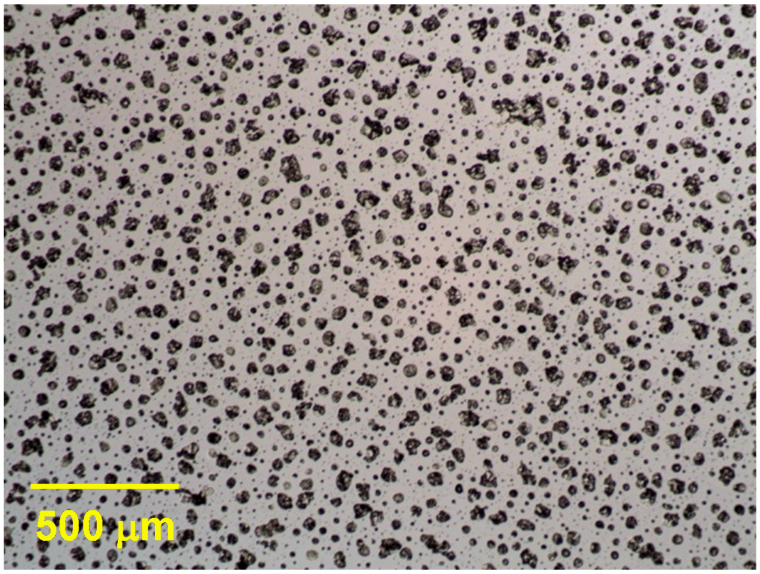

Figure 17. QCM wafer coated with 100 µg/cm^2 (1 g/m^2) of evenly dispersed NaNO$_3$.

3.3.2 Quartz Crystal Microbalance

The quartz crystal microbalance, or QCM, is a very sensitive mass measuring device. It was used to monitor the amount of salt surface loading (salt deposited per unit area) by the salt spray unit, but is also used in experiments evaluating salt and brine stability. Specifically, after coating QCM wafers with salts, they were exposed to controlled temperature and RH conditions in an environmental chamber, and mass changes were monitored. Mass changes occur because of degassing or decomposition of the dry salts, and this can be monitored directly by QCM. Once deliquescence occurs, the mass on the wafer cannot be measured for reasons discussed below. However, mass loss during the period of deliquescence can still be monitored, by measuring the mass of the initial dry salts, and then measuring the mass again, after drying the deliquesced brine out again.

To interpret the results of these experiments, a general understanding of how a QCM works is necessary. The heart of the QCM is a thin wafer of quartz, cut at a precise crystallographic orientation from a single crystal of quartz. The wafer has a gold electrode on each side (Figure 18a). Electrical contacts or leads are attached to the electrodes and an oscillator circuit is used to apply an oscillating current to the electrodes (Figure 18b). Because quartz is piezoelectric, the wafer vibrates in a direction parallel to the surface at a frequency corresponding to the fundamental frequency of the wafer (9MHz for the QCM used here). As mass is deposited onto the crystal, that fundamental frequency changes, and by monitoring the frequency change, the deposited mass can be measured (Figure 18c). Because changes in frequency of less than one Hz can be readily measured, QCMs offer an extremely precise method of measuring changes in mass on the wafer surface. The mass resolution for the 9 MHZ QCM used for these experiments is <1 ng/cm^2; corresponding to a thickness of NaCl on the surface less than 1/10 of a molecular monolayer thick.

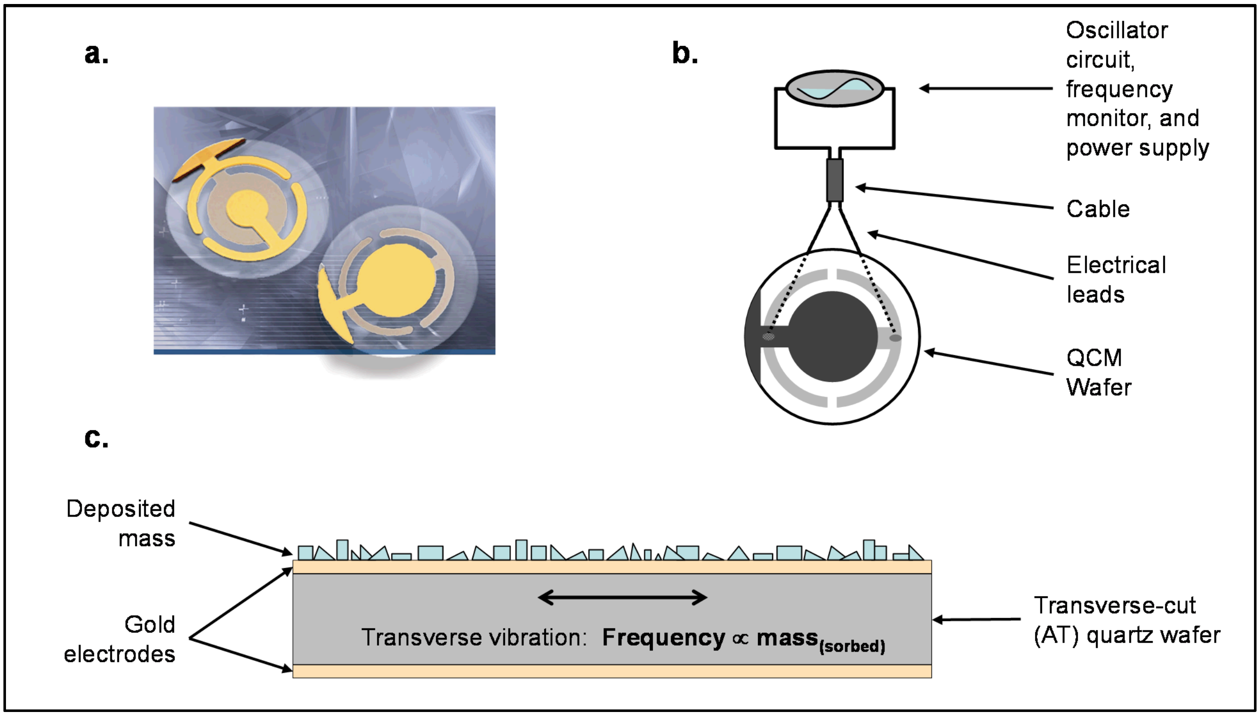

Figure 18. Operating principle of a QCM. Quartz wafers with gold electrodes (a) are connected to a control circuit that both piezoelectrically stimulates the wafer, and monitors the resulting frequency of vibration. The oscillating current creates a transverse vibration in the wafer, the frequency of which is a function of the mass deposited on the wafer (c).

The QCM can only accurately measure mass if the mass strongly couples to the surface of the wafer and vibrates with it as the wafer vibrates (Figure 19a). If the mass is not strongly coupled—for instance, if it is present as a liquid (e.g., deliquescent brine) on the wafer surface, shear or slip will occur at the contact with the wafer, and the mass will appear to be less than it actually is. At the same time, the vibration will extend into the solution and exert a viscous drag on the vibrating wafer (Figure 19b); this resistance to vibration does not affect the fundamental frequency, but instead affects the current necessary to achieve it; it is exactly equivalent to an increase in electrical resistance in the driving circuit. This means that the QCM cannot be used to measure the mass of liquid on the surface. In the experiments described here, QCM wafers are used to monitor the salt load deposited on the wafers, and are also used to monitor mass loss due to decomposition or degassing over the course of the experiment when the salts are in the solid state. The QCM can also be used to measure mass loss of deliquesced salts, however, by first measuring the mass of the dry salts, then raising the relative humidity and causing the salts to deliquesce for the test period, and then lowering the RH to dry the salts back out and measuring the mass a second time.

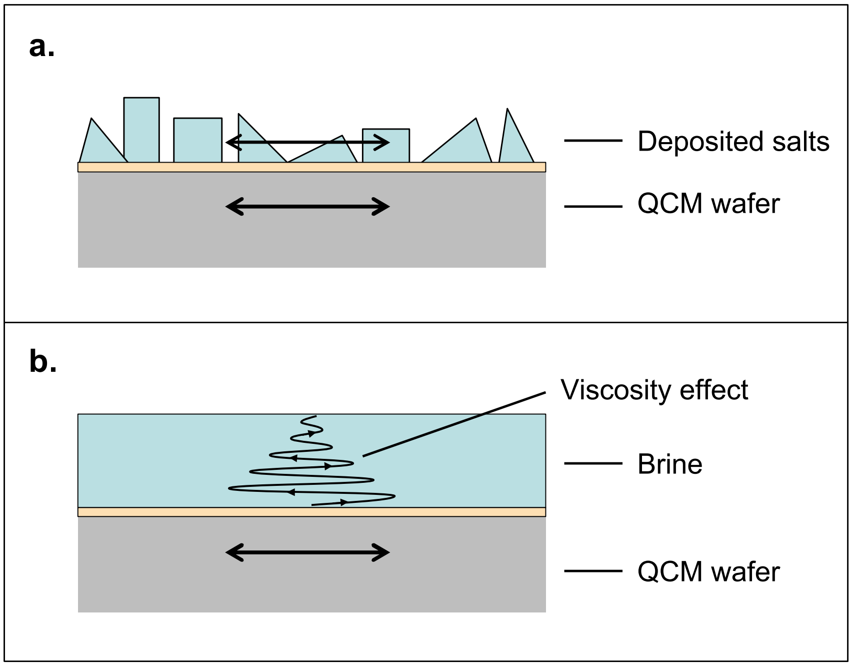

Figure 19. Solids (a) are strongly coupled to the QCM wafer surface and vibrate with the wafer, while liquids (b) do not couple well to the surface, resulting in an apparent low mass; also, viscous effects change the electrical resistance of the wafer.

3.3.3 Results of Salt/Brine Stability Experiments

To date, SNL has evaluated the stability of simple systems involving ammonium salts. These were chosen because they are the dominant soluble components at inland sites. Also, previous work has shown that they decompose relatively rapidly as bulk salts at higher temperatures (SNL 2008), and it was considered likely that finely dispersed, high surface area salts would decompose even more rapidly. If decomposition reactions are sufficiently rapid, then coexistence of ammonia and chloride on a canister surface is not possible, and the likelihood that SCC can occur at ammonium-rich inland sites may be small.

Existing data for ammonium salt decomposition rates is from SNL (2008), and is summarized in Table 9. The data suggest that at temperatures below 100ºC on an interim canister surface, NH_4NO_3 and NH_4Cl

can persist for days to years, or even years to decades at a temperature of 50ºC; lower temperatures were not tested. Moreover, the salts were dry, and the work did not evaluate whether deliquesced salts would degas as efficiently as the dry salts decomposed. However, these data were collected using fairly coarse-grained salts; it is likely that decomposition and degassing rates are a function of salt surface area, and that fine grained, high surface area atmospheric aerosols will decompose even more rapidly. To test this, salt and brine stability experiments were performed with individual ammonium salts. In future experiments, mixtures of ammonium salts will be tested, and then ammonium salts mixed with chlorides such as NaCl. For instance, it is likely that mixtures of $(NH_4)_2SO_4$ (the most common inland salt aerosol), and NaCl (possibly from road salts), while stable when dry, will degas NH_3 and HCl when deliquesced, leaving Na_2SO_4 behind. Finally, the stability of sea-salts will be examined, to evaluate the potential for conversion of $MgCl_2$(s, aq) to Mg-carbonate or Mg-hydroxychloride.

Table 9. Ammonium salt decomposition times from SNL (2008).

T (ºC)	NH_4NO_3			NH_4Cl		
	low	nominal	high	low	nominal	high
50	235 days	861 days	3208 days	11 days	347 days	9188 days
75	23.6 days	82.1 days	290 days	1.1 days	31 days	707.2 days
100	3.2 days	10.7 days	36.1 days	3.8 hr	3.8 days	76.6 days
125	13.5 hr	1.8 days	5.8 days	40.8 min	14.7 hr	262.9 hr
150	2.9 hr	9.0 hr	28.0 hr	8.9 min	2.9 hr	47.3 hr
175	44.5 min	2.2 hr	6.7 hr	2.3 min	41.4 min	10.3 hr
200	13.1 min	38 min	1.9 hr	0.7 min	11.4 min	2.6 hr
225	4.4 min	12.3 min	35.4 min	0.2 min	3.6 min	46.1 min
250	1.6 min	4.4 min	12.5 min	0.1 min	1.3 min	15.2 min

3.3.3.1 NH_4NO_3

In this experiment, 100 µg/cm^2 was deposited on a QCM wafer, the wafer was placed in an environmental chamber at the desired conditions, and decomposition and degassing were monitored by measuring the weight change over time. Because only one salt is present, the weight change correlates directly to amount of salt lost, and it was not necessary to coat and analyze metal coupons to evaluate changes in composition. First, conditions for deliquescence were evaluated. A temperature of 50ºC was used as a baseline. The sample was placed in a Thunder Scientific environmental chamber, and the minimum possible RH was used, corresponding to about 11% as measured by a Viasala RH probe placed adjacent to the QCM wafer in the center of the chamber. An unloaded QCM wafer was also placed in the chamber, as a blank. Then, the RH was ramped up in 5% increments. The results are shown in Figure 20. There was an overall decrease in mass over the course of the experiment, as NH_4NO_3 decomposed (dry salt) or degassed (deliquesced brine) from the wafer surface. The salt deliquesced between 40 and 45% RH (about 210 minutes into the experiment), and there was an apparent large loss in mass, along with a concomitant large increase in resistance as the brine decoupled from the wafer surface. However, when the RH was decreased to about 28%, below the deliquescence RH, the salts dried back out, and recoupled with the wafer. At this point, it was possible to accurately measure the mass load again. To verify that deliquescence had occurred, the RH was once again raised to above 40% (about 270 minutes into the experiment) and decoupling occurred once again.

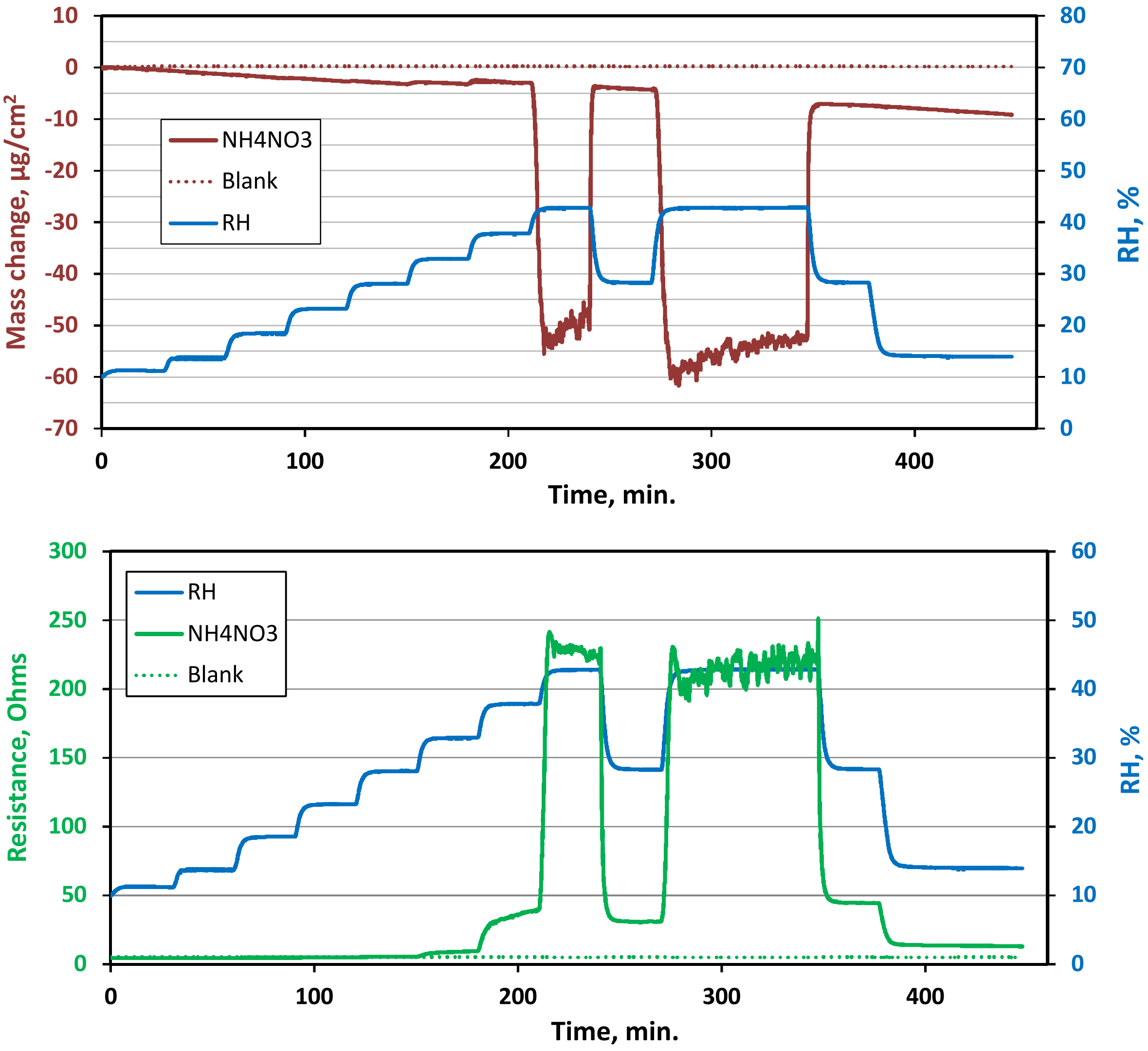

Figure 20. Changes in apparent mass loading (upper) and electrical resistance (lower) as a function of RH, for a QCM wafer loaded with 100 $\mu g/cm_2$ NH_4NO_3.

An expanded image of the upper part of Figure 20 is shown in Figure 21. An important feature of this image is that it shows that there are progressively larger increases in the mass loading on the wafer as the deliquescence RH is approached. These show that, while full deliquescence and conversion from a solid salt to a brine is sharply delineated, some water adsorption occurs below the deliquescence point. This is commonly observed for many deliquescent salts, including NaCl and $MgCl_2$ (e.g., Dai et al. 1997; Schindelholz et al. 2013), and is probably the reason why the threshold RH for corrosion (RH_L) is below the deliquescence RH. Thin adsorbed water films on the salt surface form initially at high-energy step sites, and then, with increasing RH, expand over the salt grain surface until they are sufficient to support corrosion. Corrosion has frequently been observed at RH values below the deliquescence point of $MgCl_2$, the most abundant component in sea-salt deliquescent brines at low RH. This has been attributed to the presence of a $CaCl_2$ hydrate, which deliquesces at lower RH values, in small amounts (NRC 2014). However, this is probably incorrect. Thermodynamic modeling shows that Ca concentrations in sea-salt deliquescent brines are controlled by precipitation of gypsum and anhydrite, and are extremely low at low RH. It is more likely that the development of adsorbed water films on the hydrated $MgCl_2$ mineral phase is the real cause.

In the next experiment, mass loss as a function of temperature was measured, first decomposition of the dry salt at ~13 % RH, and then degassing from the deliquesced brine, at a RH above the RH_D. Mass loss was measured directly under dry conditions. To measure mass loss from deliquesced brines, the surface load was first measured dry, then the salts were deliquesced for a time interval, and the dried out again, and a second reading taken. Dry and deliquesced degassing rates were measured at 50ºC, 40ºC, and 30ºC (Figure 22). The deliquescence RH of NH_4NO_3 is temperature-sensitive; at 50ºC and 40ºC, deliquescence occurred at about 40% RH, while at 30ºC, it was necessary to raise the RH to 50% to reach deliquescence. In this plot, the yellow lines are linear fits to the data for dry decomposition, and connect the measured masses under dry conditions before and after deliquescence for wet conditions. The slopes of the lines represent the rate of mass loss at each condition.

The mass on the QCM wafer decreased over the entire duration of the experiment, as the time was insufficient to result in complete loss of the ammonium nitrate. At the end of the experiment, the surface was examined with a microscope to verify that the recorded changes were not artifacts of the experimental method. Before and after images of the salt loading on the wafer are shown in Figure 23; it is clear that the majority of the salt has been lost from the wafer. The wafer was returned to the environmental chamber at 50ºC and 13% RH, and after additional ageing, the NH_4NO_3 decomposed completely. The rates of mass loss are summarized in Table 10. Finely dispersed NH_4NO_3 decomposes very rapidly even at low temperatures. A surface load of 1 g/m^2, which is quite heavy relative to measured salt loads on in-service canisters and would require years or decades to accumulate, would degas within days to a few weeks even at canister surface temperatures as low as 30ºC. It is clear that NH_4NO_3 accumulation cannot occur at temperatures above ambient.

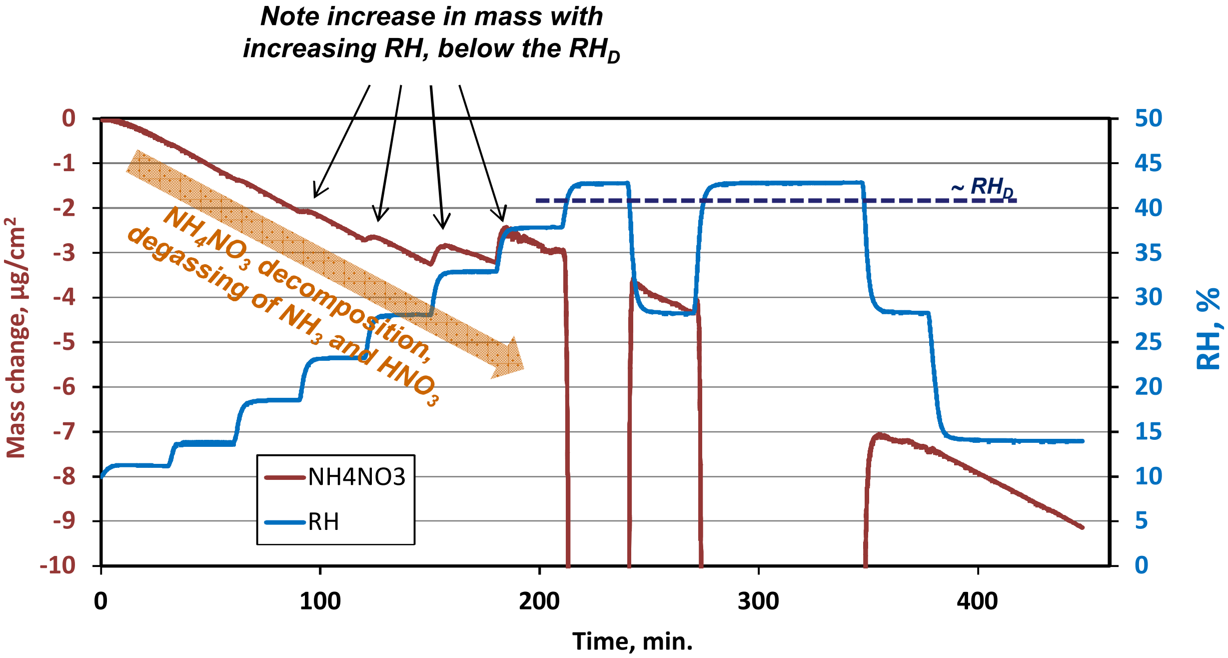

Figure 21. Expanded image of Figure 20, showing water adsorption by NH_4NO_3 prior to deliquescence.

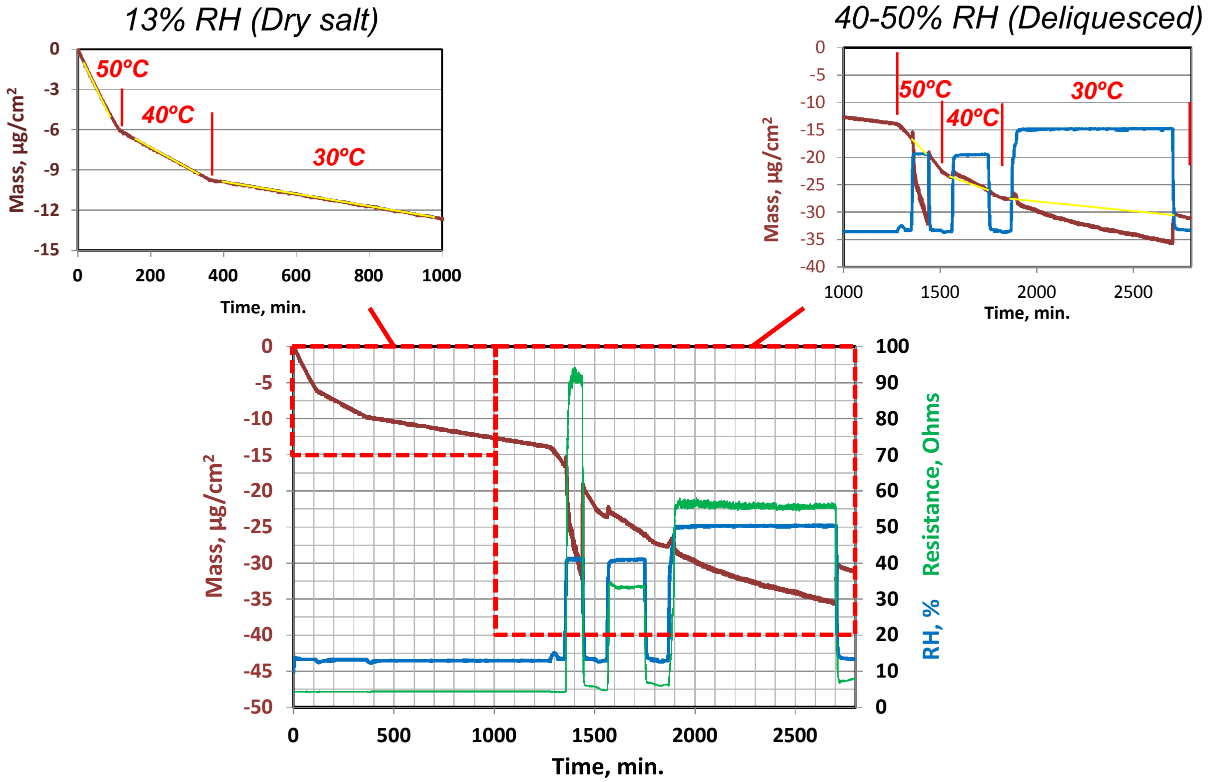

Figure 22. QCM measurements of NH_4NO_3 mass loss as a function of temperature, under dry and deliquesced conditions.

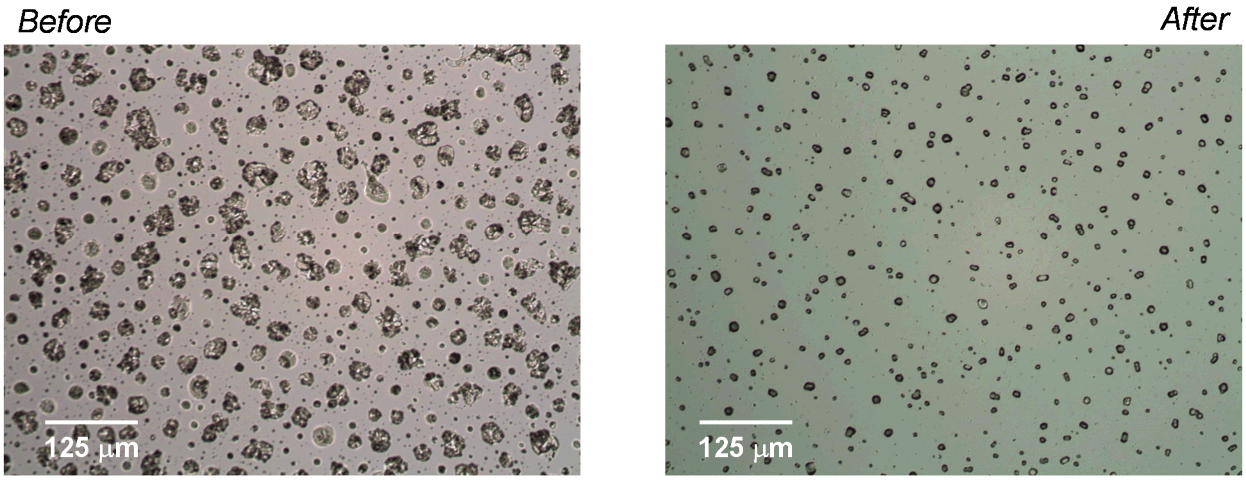

Figure 23. NH_4NO_3 loading on the QCM wafer, prior to and after testing.

Table 10. NH_4NO_3 degassing rates as a function of temperature.

T, ºC	RH	Decomp. Rate, mg/m^{-2} hr^{-1}	Days to degas a load of 1 g/m^{-2}
Dry			
49.7	13.2%	32.10	1.3
41.2	13.2%	8.78	4.7
30.6	13.0%	2.72	15.3
Deliquesced			
50.3	41.2%	20.28	2.1
40.8	41.0%	8.56	4.9
31.2	50.3%	1.97	21.2

3.3.3.2 NH_4Cl

A second salt and brine stability test was conducted with NH_4Cl, following the same protocol as the NH_4NO_3 experiment. Degassing rates were measured at 50ºC, 40ºC, and 30ºC under both dry and deliquesced conditions. Because NH_4Cl is less soluble than NH_4NO_3, the RH required for deliquescence is higher. At 50ºC and 40ºC, NH_4Cl deliquesced between 65% and 70% RH, while at 30ºC, it occurred between 70% and 75% RH. The QCM measurements of mass loss are shown in Figure 24. NH_4Cl degassing and mass loss occurred rapidly for both the solid phase and the deliquesced brine. Rates for NH_4Cl mass loss are provided in Table 11, and are only slightly lower than the rates for NH_4NO_3. An NH_4Cl surface load of 1 g/m^2 would degas within days to perhaps one month, even at canister surface temperatures as low as 30ºC.

Activation energies for NH_4NO_3 and NH_4Cl degassing

The measured rate data for NH_4NO_3 and NH_4Cl were used to create linearized Arrhenius plots (ln(rate) versus 1/T), as shown in Figure 25. A best-fit line was fitted to each data set and the slope of the line was used to calculate the activation energy (E_a) for decomposition of the solid salt, or degassing of the deliquesced brine. Measured E_a values are given in Table 12. For both salts, the values for degassing from the solid salt and the brine are very similar and probably within the uncertainty in the measurement. The E_a values for NH_4NO_3 are approximately 100 kJ/mol, while those for NH_4Cl are slightly lower, about 95 kJ/mol. These values are slightly higher than those reported in SNL (2008) which are, respectively, 91.5 and 89 kJ/mol.

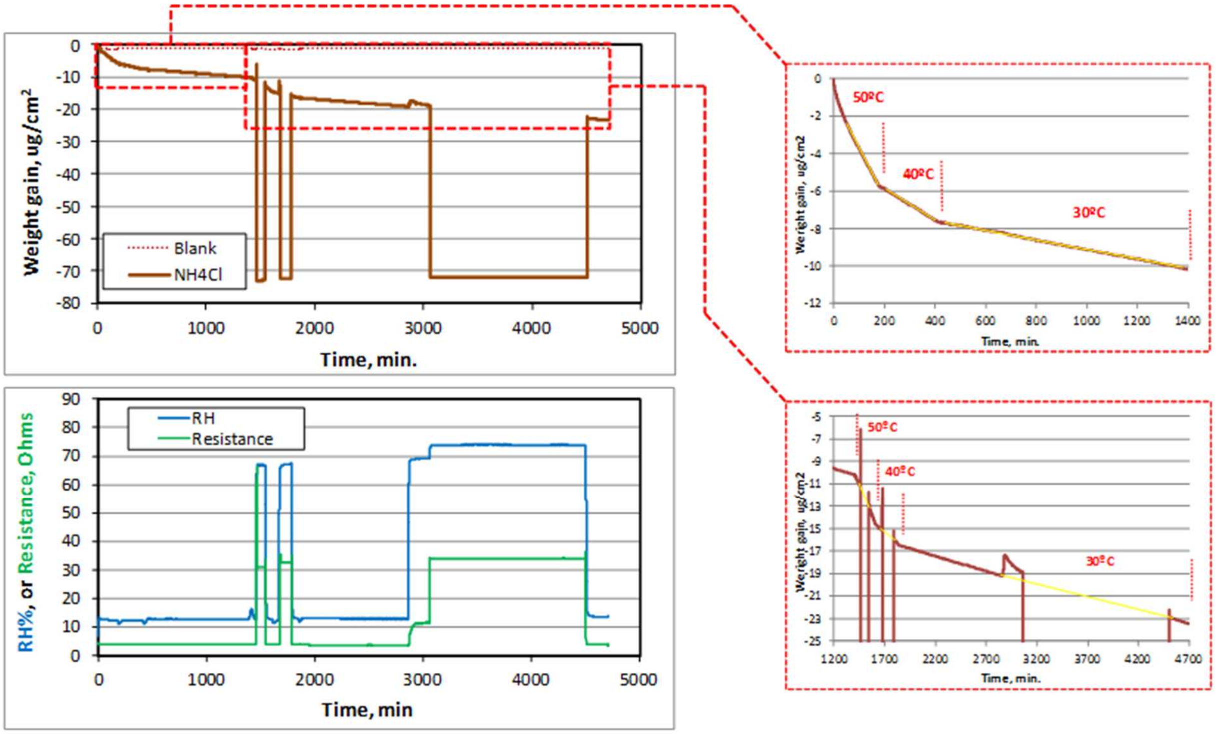

Figure 24. QCM measurements of NH_4Cl mass loss as a function of temperature, under dry and deliquesced conditions.

Table 11. NH_4Cl degassing rates as a function of temperature.

T, ºC	RH	Decomp. Rate, mg/m^{-2} hr^{-1}	Days to degas a load of 1 g/m^{-2}
Dry			
49.8	12.6	15.20	2.7
40.6	12.5	5.03	8.3
30.6	13.0	1.57	26.5
Deliquesced			
50.2	63.9	12.98	3.2
40.4	62.1	4.26	9.8
30.7	72.9	1.33	31.4

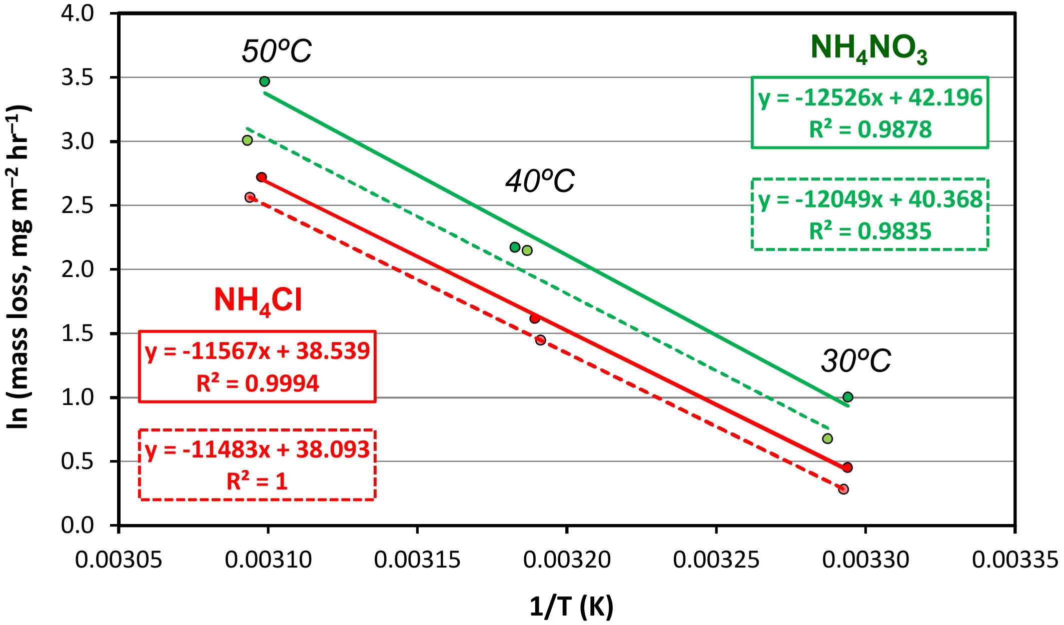

Figure 25. Arrhenius plots of mass loss data for NH_4NO_3 and NH_4Cl. Solid lines—dry conditions. Dotted lines—deliquesced conditions.

Table 12. Calculated activation energies for NH_4NO_3 and NH_4Cl degassing.

Salt	**Ea, kJ/mol**
NH_4NO_3, dry	104.1
NH_4NO_3, deliquesced	100.2
NH_4Cl, dry	96.2
NH_4Cl, deliquesced	95.5

3.3.3.3 $(NH_4)_2SO_4$

Only preliminary experiments have been carried out with $(NH_4)_2SO_4$. The results indicate that deliquescence occurs between 75% and 80% RH, but there is measurable water adsorption onto the salt surfaces as low at 55% RH. Degassing results at 50ºC seem to be consistent with those in SNL (2008). Over the course of a several-hour experiment, no measurable decomposition of the solid phase occurred. Degassing under deliquescent conditions was not evaluated. Longer duration experiments with $(NH_4)_2SO_4$ will be carried out in the future.

3.3.3.4 Summary of Salt/brine Stability Experiments

Preliminary experiments show that NH_4NO_3 and NH_4Cl decompose very rapidly in the solid phase, at even slightly elevated temperatures. Degassing from the deliquesced salt is also very rapid. It is not possible for these salts to persist or accumulate on the surface of interim storage canisters at temperatures above ambient. Preliminary data for $(NH_4)_2SO_4$ indicate it does not decompose rapidly, and will likely accumulate on canister surfaces at inland sites, where it is an important atmospheric aerosol.

It is important to recognize that ammonium chloride and ammonium nitrate will not persist on storage canisters at elevated temperatures, but the real goal of these experiments is to evaluate if chloride deposited as a different chloride salt at an inland site—perhaps NaCl in road salt—can deliquesce to form a corrosive brine on storage canister surfaces. It seems likely that this can only occur if the rate of nitrate and chloride deposition exceeds the rate of ammonium deposition (as sulfate, nitrate, or chloride), because once deliquescence occurs, the resulting brine will degas ammonia and chloride/nitrate until one or the other is consumed. Given that ammonium sulfate is the most abundant salt in inland aerosols and sulfate does not degas, it seems likely that ammonium will the component in excess, and chloride-rich brines will not form. Planned degassing experiments will evaluate the degassing of mixed salt assemblages to test this hypothesis. Additional experiments will evaluate the stability of sea salts, concentrating on potential reactions that convert magnesium chloride to less deliquescent salts.

4. CHARACTERIZATION OF WELD REGIONS ON A FULL-DIAMETER CYLINDRICAL MOCKUP OF AN INTERIM STORAGE CANISTER

In recognition that accurate assessment of storage canister SCC requires accurate characterization of canister weld regions, both in terms of material properties and weld residual stresses, SNL procured a full-diameter cylindrical mockup of an interim storage canister, made using the same materials and manufacturing processes as one type of in-service canister. SNL is in the process of characterizing the material properties of the canister base metal and weld zones. The status of the mockup characterization work was recently provided in Enos and Bryan (2015); a short summary is presented here.

In order for SCC to be a viable degradation mode, three criteria must be met – there must be a sufficiently large stress in the material to support crack growth, the material itself must be susceptible to stress corrosion cracking, and the environment must be sufficiently aggressive to support crack initiation and propagation (Section 1). SNL is evaluating the first two of these criteria for in-service containers by characterizing the material properties of the base metal and weld zones on the canister mockup. Assessment of residual stresses associated with forming and welding is being performed using a combination of three techniques. These include deep-hole drilling (DHD), the contour method, and x-ray diffraction (XRD). The DHD technique allows measurement of residual stresses along a one-dimensional hole drilled through the wall of the cylinder; it allows measurement of stresses within the intact cylinder and hence, captures the effects of the cylindrical constraint on the stresses. The contour method provides a two-dimensional map of stresses along a cross section through a region of interest; however, the mockup must be cut into pieces to measure the face of the cross section, and stresses due to the constraint of the intact cylinder are lost. XRD allows assessment of very shallow near-surface stresses, and potentially phase changes (e.g., formation of deformation-induced martensite), associated with shaping and grinding the mockup. It is also used to map stress components that are in-plane with the cross sectional surface, when using the contour method.

Characterization of residual stresses in the mockup has begun. After fabrication, the mockup was cut into three sections (Figure 26). The largest section was reserved for residual stress measurements; the other two pieces will be used for material characterization studies and testing of SCC evaluation methods. During the cutting process, strain gauges were used to monitor stress relaxation at locations where weld residual stresses will ultimately be measured, so that it can be added back in if necessary to obtain the as-manufactured residual stresses. However, measured strains were very small, as shown for strain gauges near the circumferential weld in Figure 27, and can be ignored. Cutting the cylinder in half had little effect on residual stresses.

One set of stress measurements has been collected to date, at a base metal location far from any weld. The incremental center-hole drilling (iCHD) technique was used to measure very shallow stresses (<0.5 mm), while the DHD technique was used to measure the through-thickness stress profile. Results (Figure 28) indicate that in this non-welded region, residual stresses are dominated by those introduced during the forming of the plate to make a cylinder. The rolling process extended the outer surface of the shell while shortening the inner surface, and the residual stresses reflect this; except for near-surface regions, the outer half of the shell wall is under tension, while the inner half of the wall is under compression. These data will provide a baseline for the residual stresses near the weld zones, to be measured in coming months.

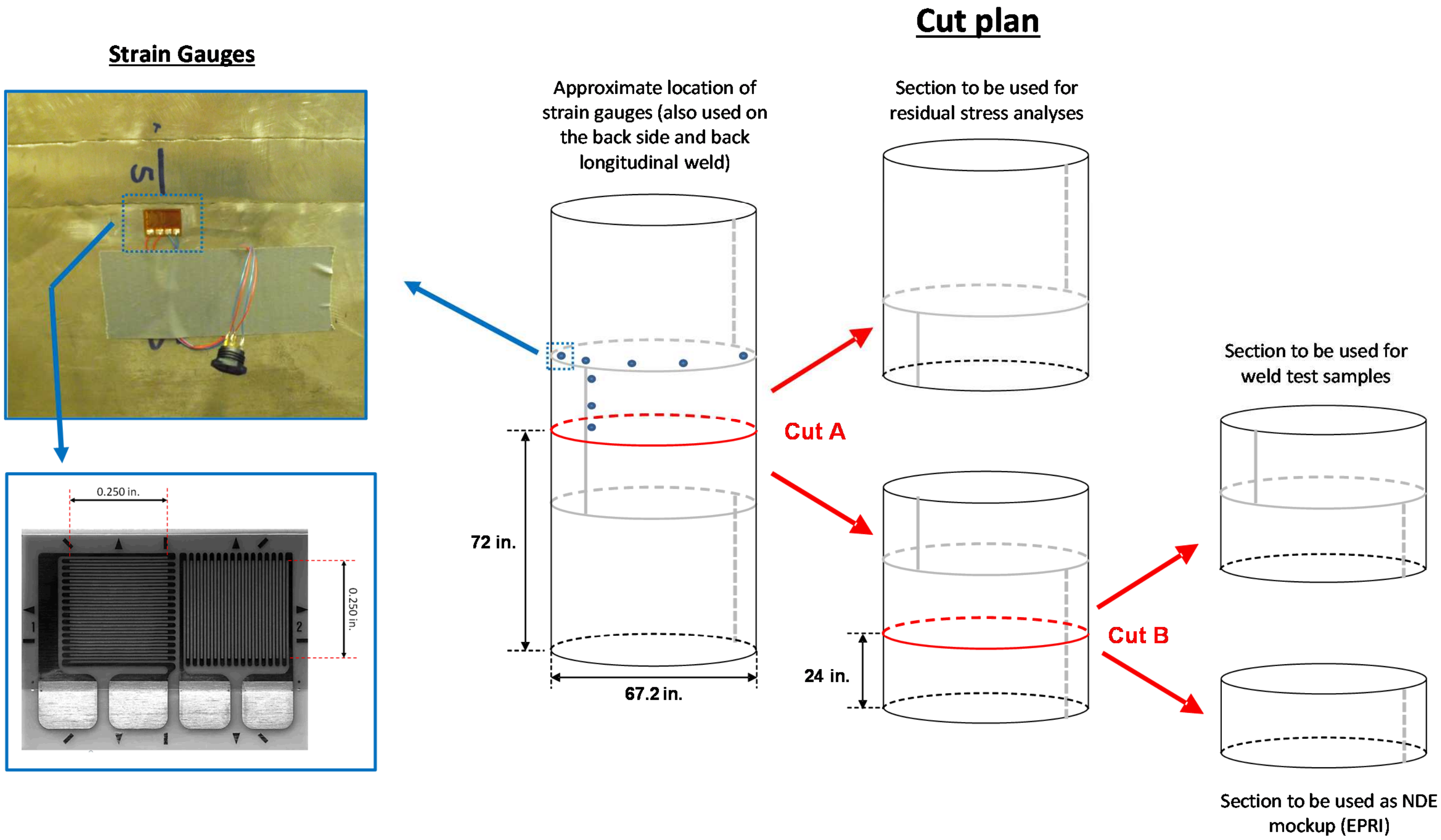

Figure 26. Cut plan used to subdivide the mockup container into sections for residual stress analysis and test coupons Strain gauges were placed adjacent to weld regions to monitor stress relaxation during cutting.

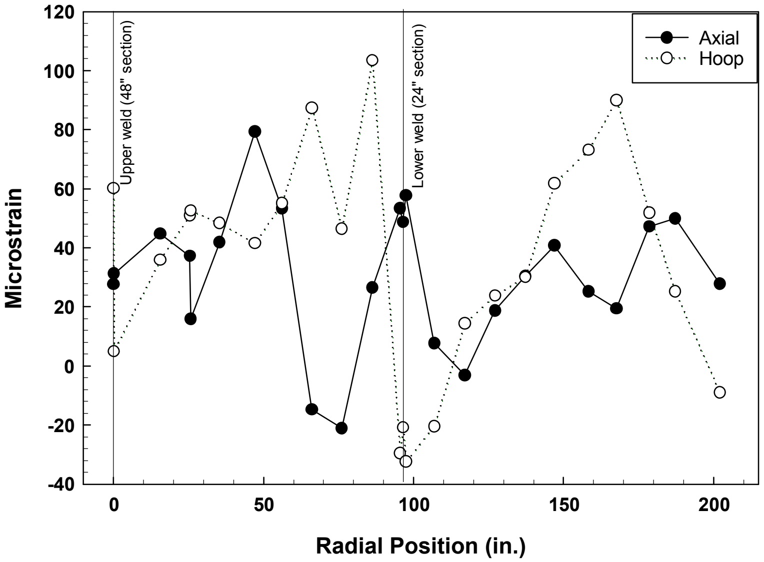

Figure 27. Surface strain measurements along the circumferential weld after cutting. Note that the sensors are located approximately 10 inches apart and that the overall circumference was 211 inches.

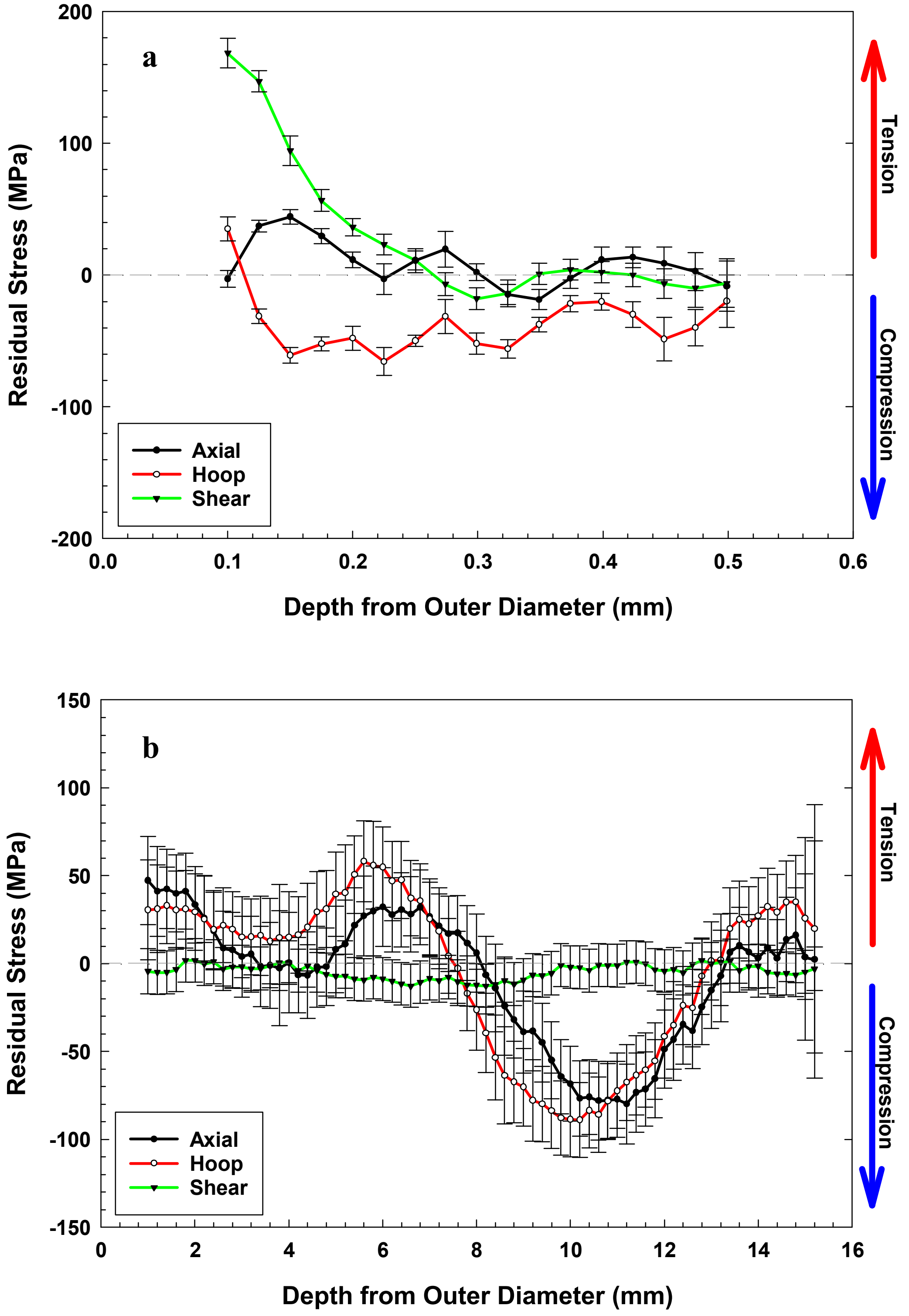

Figure 28. a) iCHD data for a base-metal region located far from any longitudinal or circumferential weldments). b) DHD data as a function of distance from the outer diameter of the container for a region located far from any weldments. Residual stresses were introduced when the original flat plate was formed into a cylinder.

Evaluation of the electrochemical properties of the welded regions of the container will first involve an assessment of the microstructure of the regions at the longitudinal, circumferential, and repair welds via standard metallurgical techniques. The thermal cycling associated with the welding process will, in addition to altering the overall microstructure of the near-weld material, result in the precipitation of chromium carbides and the formation of chromium-depleted regions along the grain boundaries. This effect, known as sensitization, will be particularly pronounced in the weld heat affected zone (i.e., the region near the weld fusion zone that has been impacted by the heat input from the welding process). The extent to which sensitization has taken place will be documented as a function of position from the edge of the weld fusion zone. This will be done both for the near-surface regions and through the thickness of the container wall. A volumetric assessment of the degree of sensitization will illustrate the extent of the affected region and illustrate the presence/absence of an active path for crack propagation through the material. Evaluation of sensitization will be done through either the single loop electrochemical reactivation (EPR) test or (ASTM G-108, ASTM 2010) or the double-loop EPR test (Scully 1995).

It should be noted that the degree to which an austenitic stainless steel can sensitize is a function of its carbon content, with reduced carbon content alloys (e.g., L grade stainless steels such as 304L) being less susceptible. Current canisters, and the mockup, are made from dual-certified 304/304L SS; however, some early canisters may have been made from 304 SS with a higher carbon content (Pacific Nuclear Fuel Services 1991).

Establishing the storage canister susceptibility to SCC will require both the crack nucleation and crack propagation processes be assessed using samples with relevant crystallographic textures and electrochemical properties, under typical environmental conditions under stress conditions as defined by analyses of the full scale mock-up. Several types of experiments are planned to evaluate both aspects of the cracking process, as well as to define methods to produce relevant weld analog materials using a Gleeble® (weld thermomechanical simulator) for testing purposes—samples from the mockup will be few and large, and not appropriate for many types of laboratory tests.

Upon completion of the residual stress measurements, the mock-up will be sectioned to provide samples for stress corrosion cracking initiation tests. These coupons are critical for the UFD program, but also are of great interest to outside parties such as EPRI and the academic groups working on canister SCC as part of the DOE Nuclear-Energy University Programs (NEUP). Samples will be disseminated to interested parties on an as-needed basis, with the UFD program getting first priority, followed by the DOE-funded NEUP groups and EPRI.

5. CURRENT AND PLANNED CORROSION EXPERIMENTS

SNL is currently performing corrosion experiments assessing the long-term corrosion performance of interim storage canisters, and has a suite of experiments currently planned to specifically evaluate canister SCC. Current experimental work at Sandia is evaluating whether limited amounts of reactants—light surface salt loads—have a limiting effect on the extent of corrosion over time. Planned experiments address many aspects of SCC, including environmental constraints on SCC initiation and growth such as threshold RH values or threshold salt loads, and pitting and crack growth rates. Current and planned experiments are discussed below.

5.1 Localized Corrosion Performance in the Presence of Limited Reactant

The materials used to construct most interim storage containers (i.e., austenitic stainless steels such as 304 and 316) are susceptible both to localized attack and stress corrosion cracking in chloride-rich solutions. The goal of the work discussed in this section is to explore the susceptibility of these materials in terms of the extent of attack that can be supported under atmospheric conditions, where a bulk electrolyte is not present. Understanding the susceptibility of the materials to localized attack will provide considerable insight into the existence of potential SCC nucleation sites on the metal surface, as well as the extent of electrochemical activity (crevice corrosion, pitting, or SCC) that can be supported under such conditions.

Researchers have suggested that for highly corrosion resistant/passive materials, several factors will prevent extensive localized corrosion in the presence of a thin electrolyte layer. Turnbull (1997) demonstrated for cracks and crevices that if the cathodic reactions which support the dissolution taking place at the corrosion site are pushed into the occluded geometry of the crack/crevice, that the pH would increase (due to hydroxyl ion production at the cathode), resulting in an inhibiting effect. Essentially, by moderating the pH it would not be possible to form and maintain the critical crevice solution required for continued activity of the crevice. More recently, Payer et al. (2008) and Kelly et al. (2006) demonstrated that the capacity of the external cathode controls the extent to which a crevice may propagate. Furthermore, Payer et al. (2008) demonstrated that the capacity of the cathode would be determined by the quantity of salt/contaminant available on the metal surface outside of the crevice, as it dictates the volume and properties of the brine layer. In addition to the electrochemical limitations, physical limitations (e.g., limited volume of brine coupled with consumption or sequestration of aggressive species in the corrosion product) can also play a role in governing the stability of a localized corrosion site.

In an effort to determine if there is indeed a potential for deliquescent brines to result in extensive localized corrosion, or if localized corrosion will stifle due to limitations as described above, a series of experiments has been performed. 304SS coupons were decorated with thin layers of salt in the presence of an occluded geometry in an effort to establish if localized corrosion (i.e., crevice corrosion) could initiate and propagate under such conditions. In these experiments, no inert species were added, so potential physical sequestration of the brine by the dust layer due to capillary forces have been eliminated, allowing all of the material deposited on the metal surface to participate in the corrosion reaction.

In previous reports, the number density and two-dimensional area of crevice corrosion sites was presented in an attempt to characterize the nucleation and growth of crevice corrosion sites as a function of time and salt loading on the surface. These data were combined with depth information obtained through laser confocal microscopy to quantify the extent to which localized corrosion (crevice corrosion) might stifle with time (Bryan and Enos 2014a). These data (Figure 29) indicated that site nucleation occurs primarily at early times, perhaps within the first few weeks of exposure, followed by growth of the sites over time. It is not clear why such a substantial increase in volume occurred between the 50 and 100 day data sets. One possible explanation is that the material source, and hence the composition and underlying microstructure, of the samples used for the 100 day tests (which were the first experiments performed) was different than that used for the later tests. As such, tests will shortly be underway using material from the 7 and 14 day experiments that have been re-polished and loaded with salt for 100 and 150 day exposures. These experiments should establish if the 100 day is an anomalous result related to the material source, and also, determine if site growth continues beyond the 100-day mark, or if it stifles.

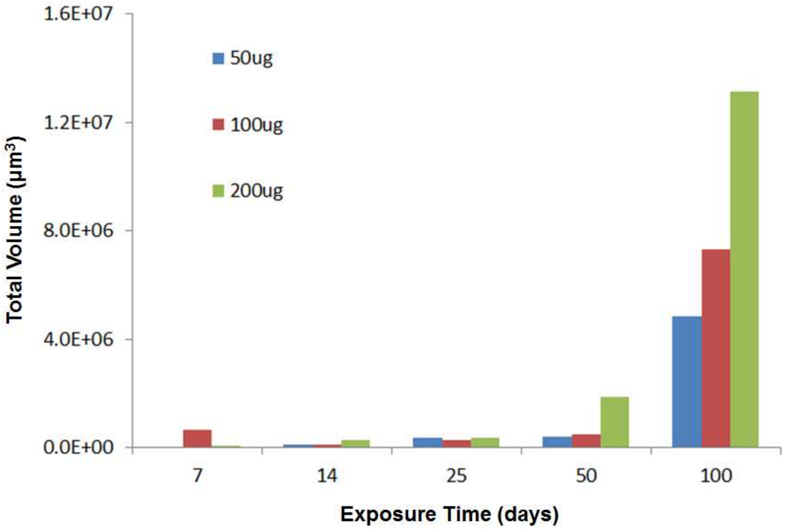

Figure 29. Estimates of total crevice corrosion volume as a function of salt loading and exposure time. Volumes are based upon laser confocal microscope measurements taken from representative sites corresponding to the different site geometry "bins" used when reporting the 2-D surface area of corrosion sites.

5.2 Planned Experiments

Recently, SNL developed a model to assess SCC of SNF interim storage canisters as part of a project to quantify the uncertainties in the predicted performance of long-term interim storage. One goal of this model was to identify the parameters for which uncertainty has a large effect on the predicted SCC penetration times for SNF interim storage canisters. Moreover, a separate model for storage canister SCC has been developed by EPRI (2014b), and comparing the results of the SNL model to the EPRI model also helps identify important parameters. As a result of that work, research needs have been identified.

5.2.1 Identification of Critical Parameters

Important parameters for predicting SCC include environmental parameters and material properties that have an effect on both the occurrence of SCC and the rate of canister penetration. Given the assumptions in the SNL and EPRI models, the results showed that uncertainties in the following parameters have the largest effect on predicted canister lifetimes:

- Crack growth rates: The most important factor in controlling penetration times was the sampled crack growth rate. Available experimental data show great variation in crack growth rates, and reducing the uncertainty in this parameter is critical for more accurately predicting SCC penetration times.
- Limiting RH at which corrosion can occur (RH_L). For any given absolute relative humidity (AH), the RH_L, controls the temperature at which corrosion can initiate, and also, during early times, the total time of wetness, or total time during which corrosive conditions are present.

- Some model parameters are handled by assumptions in both models. These assumptions may have a large effect on predicted canister lifetimes, and include:
  - It is assumed that, in the presence of chloride salts at an $RH > RH_L$, there is no incubation time for initiation of pitting and SCC.
  - It is assumed that there is no threshold lower limit for the chloride surface load that can cause SCC.
  - It is assumed that salts deliquesce instantly when the RH increases above the RH_L, and dries out instantly when the RH decreases below the RH_L.

SNL is initiating a suite of corrosion experiments to evaluate many of these parameters and model assumptions, with the aim of reducing uncertainty in predicted canister SCC penetration rates. Each of these parameters is discussed below.

5.2.1.1 Crack Growth Rates

Many experimental studies have been performed, yielding a large range in values. The SNL model evaluated the published studies, eliminated one specific set of data, generated by the Japanese research group CRIEPI (Tani et al. 2008; Shirai et al. 2011a; Shirai et al. 2011b), then probabilistically sampled the remaining data to determine corrosion rate parameters. Statistical analysis of the results of the SNL probabilistic SCC model identified crack growth parameters as the strongest control on penetration times. Even considering that that the CRIEPI data was not used, the large range in measured crack growth rates made uncertainty in this parameter the single most important factor in estimating canister performance. The EPRI model utilized the much slower crack growth rates in the CRIEPI data set that SNL eliminated and obtained considerably larger values for penetration time. For this reason, the CRIEPI experiments are discussed in detail here.

In the CRIEPI experiments, salts were placed on the surface of 4-point bend specimens, and the specimens were exposed to 35% RH at 80ºC for an extended period of time. The salts were added as a small 20 µL droplet to the surface of the samples, and both synthetic seawater (3 samples), and saturated magnesium chloride solution (one sample) were used. Stress corrosion cracks formed in all cases. In the case of sea-salts, the cracks grew rapidly to depths of 2-3 mm, and then slowed markedly to a steady, slow rate. In the case of magnesium chloride, the growth rate remained elevated throughout the course of the experiment. CRIEPI attributed the slowing of crack growth in the sea salt case to limitations in transport between the cathode and anode because the majority of the salts remained in solid form at the test RH. In the case of magnesium chloride, the salts would have entirely deliquesced, resulting in a larger volume of brine and reducing cathodic limitation. The EPRI SCC corrosion model implemented the CRIEPI data as a two-stage growth model, in which the initial fast rate applied to 3 mm, and then the longer term slow rate was used for greater depths. SNL evaluated the CRIEPI data and hypothesized that the slowing of crack growth rate for greater depths was an experimental artifact. For this reason, the slow crack growth rates at greater crack depths were not included in the crack growth data that formed the basis of the SNL model.

If the CRIEPI data accurately depict crack growth behavior, and thin brine films result in cathodic limitation of crack growth, then canister penetration by SCC may be greatly delayed. For this reason, it is critical to assess and verify the proposed mechanism and observed corrosion rates that CRIEPI derived. Potential issues with the CRIEPI results are based primarily on two experimental design choices:

- The crack growth rate experiments were performed using 4-point bend specimens.
- The salts were deposited on the bent beams as a single droplet, instead of being sprayed evenly across the surface of the sample, as dust on an interim storage canister would be distributed.

The potential implications of these choices are discussed below.

Use of 4-point bend specimens

Four-point bend specimens are commonly used to assess susceptibility to stress corrosion cracking, and there is an ISO method for this: ISO/FDIS 16540 *Corrosion of metals and alloys — Methodology for determining the resistance of metals to stress corrosion cracking using the four-point bend method.* However, this method is for assessing SCC susceptibility, not for measuring crack growth rates. The reason for this is given in the ISO method:

> *The four-point bend test is a constant displacement test that is performed by supporting a beam specimen on two loading rollers (bearing cylinders) and applying a load through two other loading rollers so that one face of the specimen is in tension (and uniformly stressed between the inner rollers) and the other is in compression. The stress at mid-thickness is zero and there will be significant gradients in stress through the thickness, this being most marked for thin specimens. As a consequence, cracks may initiate, but then arrest or their growth rate decrease.*

In the four-point bend specimens used by CRIEPI, the initial bending moment produced a stress profile as shown in Figure 30. The CRIEPI 4-point bent beam was 220 mm long, 20 mm wide, and 10 mm thick, with bending moment corresponding to a 270 MPa outer fiber tensile stress. Under a bending moment, the tensile stress decreases rapidly with depth, becomes 0 at a neutral plane in the center of the sample. With further increases in depth, the stress state becomes increasingly compressive, finally reaching a value of 270 MPa compressive stress at the inner fiber.

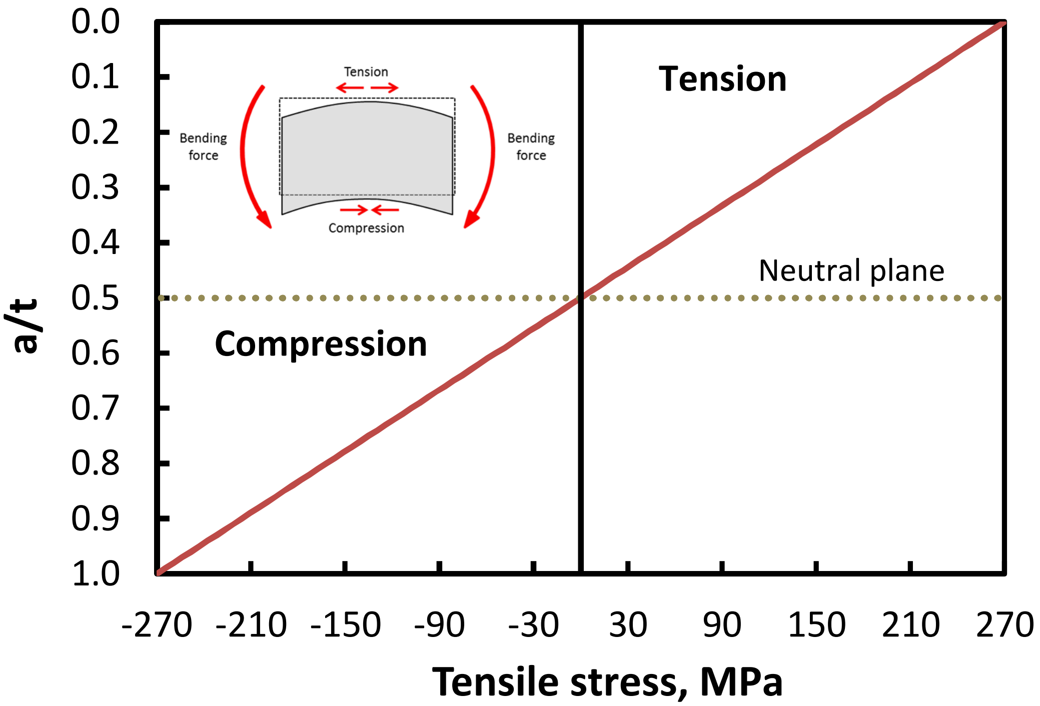

Figure 30. Initial stress distribution in the CRIEPI four-point bend specimens.
a/t = (depth)/(sample thickness)

As a crack propagates though the sample, the change in stress condition is reflected in the crack tip stress intensity factor (K_I). Values of K_I as a function of crack depth at crack tip locations corresponding to the bottom of the crack (90º) and the crack tip at the surface (0º) were calculated by EPRI (2014b) using the methods of Newman and Raju (1979), and have been recalculated here (Figure 31). Also shown is the predicted change in K_I for an infinite plate under the same bending moment, and the results are also shown for a crack in a sample under a uniform tension of 270 MPa, instead of under a bending moment. This is a good representation for a storage canister, because even a through-penetrating SCC crack will be very small relative to the area of the outside of a storage canister (5 m long and about 5.3 m in circumference). All calculations were done using a crack depth to half-length ratio (*a*/*c*) of 1. That is, the crack is assumed to be semicircular, as that is what EPRI assumed (although CRIEPI reported *a*/*c* values of 1 to 2).

In the case of the infinite plate, if *a*/*c* = 1 then K_I at the bottom of the crack (90º) initially increases, and then, after reaching a depth of a 1-2 millimeters, begins to decrease, passing though zero at a depth of 5 mm, or half the plate thickness. This is because, in an infinite plate, lateral constraints maintain the original stress profile in the sample. For a sample the dimensions of the CRIEPI beam, some constraint is lost as the crack grows, and the crack length becomes a significant fraction of the beam width. This result is a downward shifting of the neutral plane below the crack, and the neutral plane is forced down to about 7.4 mm. At the 0ºC position, on the surface of the sample, K_I continues to increase as the crack grows. Thus, K varies greatly around with location on the crack tip, from the surface to the bottom. Conversely, in a sample under uniform tension, K_I continues to increase with depth until penetration occurs. Moreover, the value of K_I varies only slightly with location on the crack tip, from where it intersects the surface to the bottom of the crack.

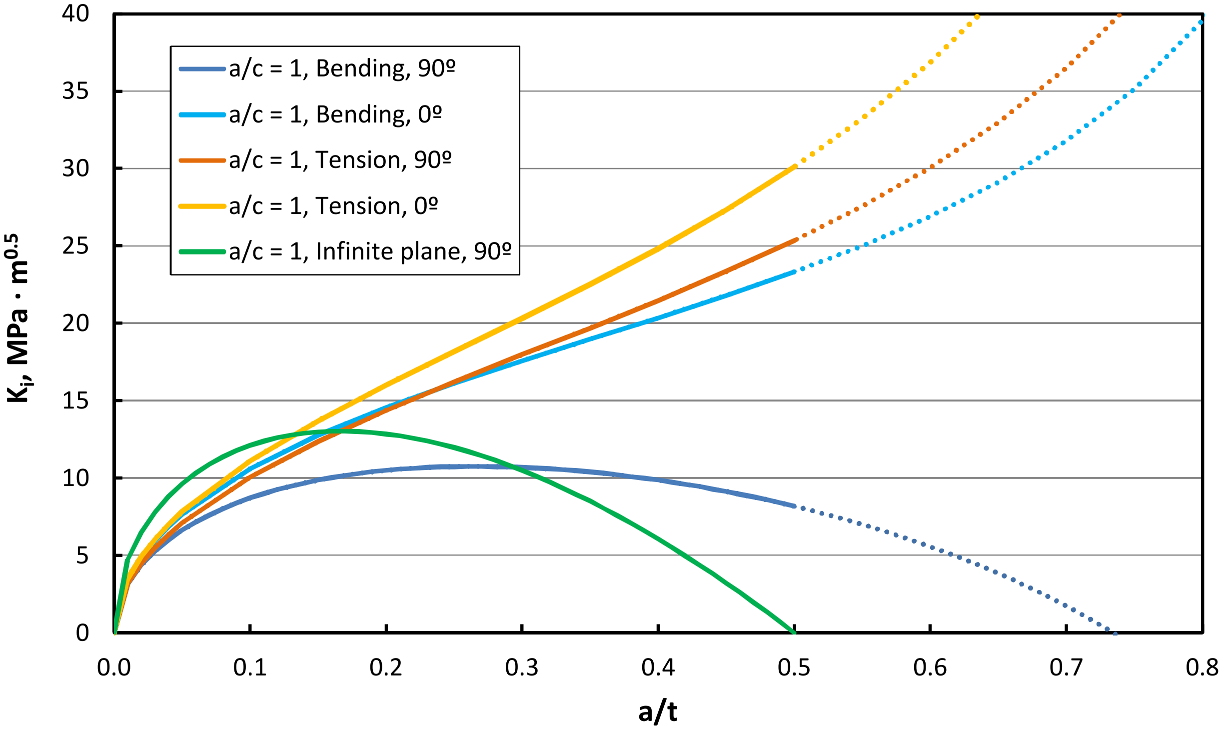

Figure 31. Stress distribution in the CRIEPI four-point bend specimens, calculated using the methods of Newman and Raju (1979). Dotted lines are outside of the range of the model used to calculate K_I values.

There are several implications of these results.

- In the CRIEPI bend sample, K_I initially increases rapidly, but slows with increasing depth, and levels off at 2-5 to 3 mm; at greater depths, it begins to decrease. This is why ISO-16540 says that cracks may slow and stop in 4-point bend specimens, and measuring crack growth with them is difficult. Note that 2.5-3 mm corresponds to the depth where crack growth changes to a much slower rate in the CRIEPI experiments. EPRI argued that although K_I levels out and begins to decrease in this range, it is unlikely to result in a change in crack growth rate, because crack growth rate was experimentally been observed to change little with K_I over a wide range in a study by Kosaki (2008). However, the Kosaki data are atypical in many ways; other studies have shown a strong dependence on K_I at low values, leveling out only at higher values (e.g., Speidel 1977; Khatak et al. 1996). Moreover, the Kosaki data were also collected on bend specimens. Moreover, other studies show the crack growth rate increasing with increasing K_I until a plateau is reached, and then sensitivity to K_I is lost. In the CRIEPI data, the crack growth rate decreases and then steadies out at a given slow rate, the exact opposite trend.
- K_I values for the bottom of a crack in a uniform tension field grow continuously with depth, and grow at a faster rate than in a bend sample, indicating that crack growth rates will likely be faster. Moreover, since crack branching is a function of K_I, occurring when K_I exceeds a threshold value (Speidel 1977), it will be inhibited in a bend specimen relative to a uniform tension specimen. Hence the geometry and mode of crack growth of a crack in a bend specimen might be expected to vary from that under uniform tension. For both of these reasons, it seems likely that 4-point bend specimens are poor testing analogs for SCC in an interim storage canister.
- For the CRIEPI bend sample, K_I has a strong dependence on location along the crack tip. Once the crack has extended to 3.5 mm, the K_I at the bottom of the crack is only about half the value of K_I where the crack tip intersects the surface. Because the crack growth rate is dependent on K_I, the crack aspect ratio will change as the crack grows, with a/c decreasing as the crack grows. On the other hand, for a sample under uniform tension, the difference in K_I along the crack front is much smaller, suggesting that the crack should be more semicircular ($a/c = 1$). This behavior has been observed experimentally and modeled theoretically for fatigue cracks by Newman and Raju (Newman and Raju 1981), and is probably applicable to SCC as well. Hence, SCC cracks in uniform tension samples and bend samples may differ in aspect ratio, making one a poor analog for the other. If the Newman and Raju (1981) model applies to SCC, then measuring SCC growth using a four-point bend specimen is not only incorrect because of the change in stress field, but also because the crack aspect ratio will differ from that of a specimen under constant tension. Moreover changes in the aspect ratio of the crack in the CRIEPI experiments, if it occurs, also affects the apparent crack growth rate in the CRIEPI specimens. This is because the crack growth rate was measured using the Potential Drop Method (PDM). The potential drop method does not measure crack depth directly, but instead measures the cross sectional area of the crack and how it affects the cross sectional area of the remaining ligament. CRIEPI calculated crack depths through time assuming that the crack aspect ratio was identical to that measured at the end of the experiment. However, if the aspect ratio changed over the course of the experiment, then the calculated evolution of crack depth as a function of time is incorrect.

Salt deposition as a droplet instead of an evenly deposited coating

The is some confusion about the salt loads used in the CRIEPI experiments and how they were applied, but the English translation of the CRIEPI report on these experiments is the most authoritative source, and is assumed to accurately describe the experimental procedure. In the 4-point bend tests, salts were applied to the beam by placing a 20 µL droplet of either synthetic seawater or saturated $MgCl_2$ solution on the center of the beam. Stated salt loads in both cases were 10 g m^2. However, this seems unlikely, as the salt was applied as a droplet, and it is very unlikely that the salt would have spread out to cover an area exactly corresponding to 10 g/m^2. Moreover, there is about 15 times as much chloride in a saturated $MgCl_2$ brine than in seawater, so the two droplets would have to spread out to very different diameters. Assuming a hemispherical shape, the initially deposited droplet containing 20 µL is about 4.2 mm in diameter. For seawater, the droplet would have spread to cover to cover an area of about 40 mm^2 (a circular area 7.2 mm in diameter) to have the reported salt loading. However, for the magnesium chloride solution, the droplet would have to be almost 600 mm^2, or cover a 3 cm long section of the 2 cm wide beam.

Assuming that the salt was deposited as a droplet, then it is possible that in the case of the sea-salts, the limited size of the salt-covered area artificially limited the surface area of the sample that could act as a cathode. This would especially be true once the length of the crack extended beyond the edge of the droplet, and further growth would require diffusion along the crack to the crack tip outside of the salt covered area. For a crack aspect ratio of a/c =1, this would occur when the crack length exceeded 5-7 mm, corresponding to a crack depth of 2.5-3.5 mm, exactly where the slow-down in growth occurred in the CRIEPI experiments.

The CRIEPI data are intriguing and promising. However, prior to relying on them, then must be verified. Part of the experimental work described below addresses that.

5.2.1.2 RH_L Values

The SNL probabilistic SCC model found that even relative small changes in the assumed RH_L had a large effect on predicted penetration times. Changing the assumed RH_L from 15% to 20% nearly doubled the predicted penetration times. However, this number is poorly known, and poorly understood. The RH_L is a function of the salt assemblage on the canister surface, and is generally somewhat below the deliquescence RH for the salt assemblage. For example, sea-salts are generally considered to deliquesce at ~30% RH, but corrosion has been observed on metal coupons covered with sea-salts at RH values as low as 15% (Mayuzumi et al. 2008); however, the SCC occurred at 80ºC, and there is some evidence that the RH_L is slightly higher at lower temperatures. However, SCC at RH values below the RH_D for magnesium chloride has been observed several times. This has been attributed to the presence of a $CaCl_2$ hydrate, which deliquesces at lower RH values, in small amounts (NRC 2014). However, this is probably incorrect. As discussed in Section 3.1.1, thermodynamic modeling shows that Ca concentrations in sea-salt deliquescent brines are controlled by precipitation of gypsum and anhydrite, and are extremely low at low RH (Figure 12). However, it is commonly observed for many deliquescent salts, including NaCl and $MgCl_2$ (e.g., Dai et al. 1997; Schindelholz et al. 2013), that water adsorption occurs on salt surfaces at RH values below the RH_D for that salt, and that is probably the reason why the RH_L is below the deliquescence RH. Thin adsorbed water films on the salt surface form initially at high-energy step sites, and then, with increasing RH, expand over the salt grain surface until they are sufficient to support corrosion.

Because of the high impact of the assumed RH_L on predicted penetration times, this parameter should be evaluated experimentally.

5.2.1.3 SCC Model Assumptions

As noted earlier, some model parameters are handled by assumptions in most current SCC predictive models. These assumptions may have a large effect on predicted canister lifetimes, and need to be evaluated experimentally. They include:

- It is assumed that, in the presence of chloride salts at an $RH>RH_L$, there is no incubation time for initiation of pitting and SCC.
- It is assumed that there is no threshold lower limit for the chloride surface load that can cause SCC.
- It is assumed that salts deliquesce instantly when the RH increases above the RH_L, and dries out instantly when the RH decreases below the RH_L.

5.2.2 Designing Experimental Protocols

A test plan is in development, but a general description of the experiments in provided below.

Pitting corrosion under atmospheric conditions (that is, deliquescent instead of immersed conditions) as a function of temperature, RH, and salt load. Pitting in a precursor to SCC; stress corrosion cracks initiate at pits, once the pits reach a certain depth. However, most pits that initiate on a metal surface will stifle, or stop growing prior to reaching the critical depth. Literature data suggest that pit growth and pit death are closely linked to salt load and RH, and the development of a sufficiently deep pit to initiate SCC may be delayed by very light salt loads. These studies will help determine if pit incubation times are sufficiently long to delay onset of SCC, and will inform canister SCC inspection intervals. These experiments will provide statistical information on pit initiation and growth rates as a function of environmental conditions—information that is not currently available in the scientific literature.

Crack initiation experiments. Much of the extant work on SCC has used salt loads that are much greater than have actually been measured. Moreover, once we have characterized the weld regions on the full-diameter mockup, we will have the necessary information to make test samples with tensile stresses, metallographic textures, and degrees of sensitization that are relevant to actual SNF interim storage canisters.

Crack growth experiments. As noted earlier, the SNL probabilistic model indicates that uncertainty in crack growth rates as a function of temperature and salt load has the single greatest impact on predicted crack growth rates. The observation by the Japanese research group CRIEPI that, under light salt loads, the growth of stress corrosion cracks seems to slow with depth is important. However, because of the potential for experimental artifacts, their interpretation, of the data, that the slowing is due to limitations in transport between the cathode (outside the crack) and the anode (within the crack) because of light salt loads, must be verified and the relationship between the surface load and the crack growth rate as a function of depth must be determined. Once again, characterization of the full-diameter mockup will allow us to evaluate these dependencies with samples and experimental setups that are relevant to actual in-service canisters.

5.2.2.1 SCC Initiation Testing

To date, the establishment of the susceptibility of the austenitic stainless steels to stress corrosion cracking has been limited to as-received material exposed to aggressive, high chloride deposits of varying concentration/surface density. While these tests established that austenitic stainless steels are indeed susceptible, they do not answer the question as to whether crack initiation is likely for the actual container material under the conditions that will exist at various ISFSI sites. The determination of the thermal and electrochemical conditions (i.e., chemical composition of the surface deposits) on fielded storage containers will enable testing to be performed under relevant conditions, allowing more realistic results to be obtained.

Material will be modified using the Gleeble® parameters established through the previously defined tasks. This material will represent the region most likely to support crack initiation from a microstructural point of view. While the residual stress analyses may indicate that this is not the most highly stressed region, it will be the most susceptible to the localized corrosion (i.e., pitting) from which SCC cracks typically initiate. Once initiated, the crack will likely propagate to and through the most highly stressed region. While cracks in sensitized materials are typically intergranular in nature upon initiation, they often propagate transgranularly (i.e., the chromium depleted zones, while having a significant impact on initiation, are not needed for propagation – the advancing crack is decoupled from the microstructural features such as grain boundaries that may be chromium depleted)

U-bend specimens will be fabricated from the above material, then loaded with the salt chemistries discussed previously. Loadings will be selected such that the chloride concentration is equal to the threshold concentrations identified elsewhere, and at loads of 10 and 100 times that level. Uniform salt deposition will be hindered by the geometry of the coupons. As such, the targeted loading will be based upon the top of the bent section, and may fall off with distance from that region. Sample loadings will be verified through the use of a quartz crystal microbalance coated in parallel with the U-bend specimens. Coated samples will be exposed to environments that bracket the worst case temperature and dewpoint levels anticipated for fielded storage containers. Samples will be exposed for 1 to 3 month time intervals, with periodic visual inspection for signs of localized corrosion (as indicated by the deposition of iron rich corrosion products on the sample surface). If no signs of attack are visible upon completion of the initial time interval, the exposure time may be extended, depending on equipment availability.

Upon completion of the test, each sample will be carefully characterized. The total number (and location) of any localized corrosion sites will be documented. Following that, the samples will be serially sectioned and the number of cracks, their depth, and crack morphology will be documented. Key parameters recorded will include the depth of any cracks present on the surface. It should be stressed that due to the loading/stress conditions that exist within a bend bar, that through thickness does not represent the upper limit of crack propagation. Rather, the maximum depth will be the region at which the stress state transforms from tensile to compressive.

5.2.2.2 SCC Crack Propagation

Crack propagation rates are needed for the effective modeling of the impact of the stress corrosion cracking process on interim storage containers. As discussed above, there is presently considerable uncertainty associated with this parameter, and it is virtually uncharacterized as a function of environment. The goal of this task, then, is to characterize the crack propagation rate as a function of surface conditions relevant to fielded storage containers. This includes both the surface chemistry as well as the thermal and humidity levels, as discussed in the crack initiation task defined above.

Crack propagation rate measurement is typically done on samples where the stress state and crack shape are known and well defined, such as compact tension specimens. Unfortunately, the nature of the environment (i.e., a salt film) for interim storage containers precludes the use of compact tension specimens. Uniform tensile specimens, such as dog bone or other similar geometries, must be used as they enable the target environmental conditions to be readily established. Furthermore, they allow thermomechanical processing of the material prior to experimentation, such that the microstructure of the material under test can be transformed to that of the heat affected zone adjacent to a weld in an interim storage container.

Uniaxial tension samples with a rectangular gauge length will be prepared. These will likely be in the form of dogbone type samples. Once machined, the surfaces will be cleaned and the current and voltage leads needed for DCPD measurements will be placed, and their contact points sealed with an appropriate material. The gauge length of the tensile bar will then be coated with varying loads of the salt chemistries identified in the tasks defined above. In addition, a series of tests will also be performed using an all chloride salt layer (i.e., $MgCl_2$, NaCl) emulating the conditions evaluated in literature studies. Samples will be loaded such that the uniaxial stress is equal to the maximum identified through residual stress analyses. Samples will be spring loaded such the test is effectively a constant load experiment (i.e., a rising K experiment). Specimens will then be placed into chambers at well defined temperatures and dewpoints for sufficient time to allow crack initiation and propagation. The DCPD signal will be utilized to assess crack propagation as a function of time.

There are a number of experimental risks associated with this approach. First, configuration of the specimen, in terms of positioning of the DCPD leads, must be done prior to beginning experimentation. Since the ultimate location of any crack that will be characterized will not be known at that time, their position may hinder the monitoring and characterization of an advancing crack, particularly when it is small. Second, the crack geometry will not be known, and any cracks which do initiate and propagate will likely not be planar and will likely be highly branched, both of which are typical properties of chloride induced stress corrosion cracks in austenitic stainless steels. As accurate prediction of crack length from a DCPD signal requires a strong understanding of the crack geometry as a function of time, while DCPD may indicate that crack propagation is taking place, correlating that to a crack length will require assumptions as to the nature of the advancing crack. Interrupted testing, where a crack is grown to a certain extent, then the sample broken open and the shape of the SCC crack characterized, will be used to quantify the geometry as a function of time. Finally, use of DCPD to estimate crack length requires that a single crack be present. In the case of experiments where a small region was contaminated (e.g., CRIEPI work), only one crack could initiate and grow. However, in the case where the sample is uniformly contaminated, this will not be the case. As a result, if multiple cracks are present, it may not be possible to deconvolute the growth rate of one particular crack from the overall DCPD response.

If unsuccessful due to multiple crack propagation, etc., additional geometries will be explored through which the specimen is precracked prior to performing environmental testing. One potential method would be to utilize EDM to place a shallow notch on one face of the test coupon. A precrack will then be grown via fatigue from that notch, then the precracked sample will be evaluated. The precrack might be filled with electrolyte by immersing in concentrated brine, then clean the surface, and deposit a relevant loading of salt on the surface (to serve as the "bulk" electrolyte). The sample will then be loaded uniaxially and the crack growth rate characterized as a function of time. Other defects could also be evaluated, such as using a Focused Ion Beam to cut a small “crack” in the surface of the coupon. Such a defect would be considerably shallower than the precracked sample discussed above, though.

5.2.2.3 Verification of CRIEPI Work

Is discussed previously, there is concern about experimental artifacts in the CRIEPI results, and also, whether 4-point bend specimens are appropriate analogs for SCC on an interim storage canister surface. Experimental designs are being considered to determine if the promising trends observed in the CRIEPI data can realistically be applied to the problem of SCC of SNF interim storage canisters.

6. SUMMARY

This progress report describes work being done at Sandia National Laboratories to assess the localized corrosion performance of container/cask materials used in the interim storage of spent nuclear fuel. Of particular concern is stress corrosion cracking, by which a through-wall crack could potentially form in a canister outer wall over time intervals that are shorter than possible dry storage times. In order for SCC to occur, three criteria must be met. A corrosive environment must be present on the canister surface, the metal must susceptible to SCC, and sufficient tensile stress to support SCC must be present through the entire thickness of the canister wall. SNL is currently evaluating the potential for each of these criteria to be met.

To assess the environment, SNL has continued to work with the Electric Power Research Institute in characterizing dust on canisters at Independent Spent Fuel Storage installations, evaluating dust samples from the surface of an unused canister at the Hope Creek site. Strong evidence of particle-to-gas conversion reactions were found, that may be effective at converting chloride salts into harmless sulfates or nitrates on the canister surface. Moreover, salt loads were actually heavier on the sides of the unused canister than on the in-service canisters sampled previously, despite the much shorter storage time, and much lower air flow rates though the overpack. This may indicate that thermophoresis is effective at rejecting dust from the surface of hot in-service canisters. Additional environment investigations include experimental work evaluating the stability of salts and deliquesced brines on hot canister surfaces; thermally-driven exchange reactions with the atmosphere may work to make salt assemblages or brines less corrosive. Moreover, the work can help define realistic salt assemblages and brine compositions for experimental studies. Preliminary studies have shown that ammonium chloride and ammonium nitrate decompose rapidly in the solid state, and cannot accumulate on a hot package. It is likely that a deliquesced brine containing ammonium and either nitrate or chloride cannot persist—it will degas ammonia and an acid gas (HCl, HNO_3, or both) until one or the other is consumed. These experiments both support development of relevant experimental matrices and potentially provide arguments for lengthening inspection intervals at some inland sites where chloride deposition may be overwhelmed by deposition of ammonium minerals.

The potential for high residual tensile stresses in interim storage canisters, and canister material properties, including material susceptibility to SCC are being evaluated by analysis of a full-diameter cylindrical mockup of a canister, fabricated by a canister supplier using the same materials and manufacturing procedures as real in-service canisters. Residual stresses due to cold working and welding processes are being measured in and around longitudinal and circumferential welds, simulated weld repair regions, and base metal far from any welds. Work to date has shown that base metal stress patterns are dominated by a bending moment introduced during rolling of the plate into a cylinder, with the outer half of the shell dominated by tensile stresses, and the inner half, by compressive stresses. Material characterization studies will begin once stresses are well understood and the mockup can be sectioned into smaller pieces, and will include 3-dimensional characterization of the degree of sensitization and textural changes near weld zones. Ultimately, this information will be used to identify relevant sample properties and stress states for corrosion testing. A suite of corrosion tests are being planned to (1) measure important environmental parameters such as threshold relative humidity and the salt surface load required for pitting and SCC initiation and growth (pits are precursors for SCC); (2) characterize pit initiation and growth rates as a function of environmental conditions; (3) SCC initiation experiments under relevant salt loads and compositions; and (4), SCC growth experiments evaluating the potential importance of processes such as cathodic limitation due to limited brine volumes and assessing crack growth rates as a function of time, crack depth, and salt load. All experiments will be carried out using samples prepared to match material properties and stresses determined from the mockup characterization work.

7. REFERENCES

Anderson, N., Strader, R. and Davidson, C. (2003). Airborne reduced nitrogen: ammonia emissions from agriculture and other sources. *Environment International* **29**, 277-286.

Aneja, V. P., Roelle, P. A., Murray, G. C., Southerland, J., Erisman, J. W., Fowler, D., Asman, W. A. and Patni, N. (2001). Atmospheric nitrogen compounds II: emissions, transport, transformation, deposition and assessment. *Atmospheric Environment* **35**, 1903-1911.

ASTM. (2010). *Method G108-94 (2010): Standard Test Method for Electrochemical Reactivation (EPR) for Detecting Sensitization of AISI Type 304 and 304L Stainless Steels*. West Conshohocken, PA. ASTM International.

Bryan, C. and Enos, D. (2014a). *Results of Stainless Steel Canister Corrosion Studies and Environmental Sample Investigations*, FCRD-UFD-2014-000055. U.S. Department of Energy.

Bryan, C. R. and Enos, D. (2014b). *Analysis of Dust Samples Collected from Spent Nuclear Fuel Interim Storage Containers at Hope Creek, Delaware, and Diablo Canyon, California*, SAND2014-16383. Albuquerque, NM. Sandia National Laboratories.

Bryan, C. R. and Enos, D. G. (2015). *Analysis of Dust Samples Collected from an Unused Spent Nuclear Fuel Interim Storage Container at Hope Creek, Delaware*, SAND2015-1746. Albuquerque, NM. Sandia National Laboratories.

Calvert Cliffs Nuclear Power Plant LLC. (2013). *Response to Request for Additional Information, RE: Calvert Cliffs Independent Spent Fuel Storage Installation License Renewal Application (TAC No. L24475)*. Lusby, MD. ADAMS ML13170A574,.

Chang, M. C., Sioutas, C., Kim, S., Gong, H. and Linn, W. S. (2000). Reduction of nitrate losses from filter and impactor samplers by means of concentration enrichment. *Atmospheric Environment* **34**, 85-98.

Cook, A., Lyon, S., Stevens, N., Gunther, M., McFiggans, G., Newman, R. and Engelberg, D. (2014). Assesing the Risk of Under-Deposit Chloride-Induced Stress Corrosion Cracking in Austenitic Stainless Steel Nuclear Waste Containers. *Corrosion Engineering, Science and Technology* **49**, 529-534.

Cook, A., Stevens, N., Duff, J., Mishelia, A., Leung, T. S., Lyon, S., Marrow, J., Ganther, W. and Cole, I. (2011). Atmospheric-induced stress corrosion cracking of austenitic stainless steels under limited chloride supply. *Proc. 18th Int. Corros. Cong., Perth, Australia*.

Dai, Q., Hu, J. and Salmeron, M. (1997). Adsorption of water on NaCl (100) surfaces: Role of atomic steps. *The Journal of Physical Chemistry B* **101**, 1994-1998.

Enos, D. and Bryan, C. (2015). *Status report: Characterization of Weld Residual Stresses on a Full-Diameter SNF Interim Storage Canister Mockup*, FCRD-UFD-2015-00123. U.S. Department of Energy.

Enos, D. G., Bryan, C. R. and Norman, K. M. (2013). *Data Report on Corrosion Testing of Stainless Steel SNF Storage Canisters*, FCRD-UFD-2013-000324. U.S. Department of Energy, Office of Used Nuclear Fuel Disposition.

EPRI. (2014a). *Calvert Cliffs Stainless Steel Dry Storage Canister Inspection*. Palo Alto, CA.

EPRI. (2014b). *Flaw Growth and Flaw Tolerance Assessment for Dry Cask Storage Canisters*. Palo Alto, CA. Electric Power Research Institute.

García, C., Martín, F., De Tiedra, P., Heredero, J. and Aparicio, M. (2001). Effects of prior cold work and sensitization heat treatment on chloride stress corrosion cracking in type 304 stainless steels. *Corrosion Science* **43**, 1519-1539.

Ghosh, S. and Kain, V. (2010a). Effect of surface machining and cold working on the ambient temperature chloride stress corrosion cracking susceptibility of AISI 304L stainless steel. *Materials Science and Engineering: A* **527**, 679-683.

Ghosh, S. and Kain, V. (2010b). Microstructural changes in AISI 304L stainless steel due to surface machining: Effect on its susceptibility to chloride stress corrosion cracking. *Journal of Nuclear Materials* **403**, 62-67.

Ghosh, S., Rana, V. P. S., Kain, V., Mittal, V. and Baveja, S. (2011). Role of residual stresses induced by industrial fabrication on stress corrosion cracking susceptibility of austenitic stainless steel. *Materials & Design* **32**, 3823-3831.

Hayashibara, H., Mayuzumi, M. and Mizutani, Y. (2008). Effects of temperature and humidity on atmospheric stress corrosion cracking of 304 stainless steel. *CORROSION 2008*.

Hitchcock, D. R., Spiller, L. L. and Wilson, W. E. (1980). Sulfuric acid aerosols and HCl release in coastal atmospheres: Evidence of rapid formation of sulfuric acid particulates. *Atmospheric Environment* **14,** , 165-182.

Kain, R. M. (1990). Marine atmosphere corrosion cracking of austenic stainless steels. *Materials Performance* **29**, 60-62.

Kelly, R. G., Agarwal, A. S., Cui, F., Shan, X., Landau, U. and Payer, J. (2006). Considerations of the Role of the Cathodic Region in Localized Corrosion. *International High-Level Radioactive Waste Managment Conference (IHLRWMC)*. Las Vegas, NV: American Nuclear Society.

Khatak, H., Gnanamoorthy, J. and Rodriguez, P. (1996). Studies on the influence of metallurgical variables on the stress corrosion behavior of AISI 304 stainless steel in sodium chloride solution using the fracture mechanics approach. *Metallurgical and Materials Transactions A* **27**, 1313-1325.

Kosaki, A. (2008). Evaluation method of corrosion lifetime of conventional stainless steel canister under oceanic air environment. *Nuclear Engineering and Design* **238**, 1233-1240.

Kuniya, J., Masaoka, I. and Sasaki, R. (1988). Effect of cold work on the stress corrosion cracking of nonsensitized AISI 304 stainless steel in high-temperature oxygenated water. *Corrosion* **44**, 21-28.

Malm, W. C., Schichtel, B. A., Pitchford, M. L., Ashbaugh, l. L. and Eldred, R. A. (2003). Spatial and month trends in speciated fine particle concentration in the United States. *Journal of Geophysical Research* **109,** , 1-22.

Mayuzumi, M., Tani, J. and Arai, T. (2008). Chloride induced stress corrosion cracking of candidate canister materials for dry storage of spent fuel. *Nuclear Engineering and Design* **238**, 1227-1232.

Mintz, T. S., Caseres, L., He, X., Dante, J., Oberson, G., Dunn, D. S. and Ahn, T. (2012). Atmospheric Salt Fog Testing to Evaluate Chloride-Induced Stress Corrosion Cracking of Type 304 Stainless Steel. *Corrosion 2012*. Salt Lake City, March 11-15: NACE.

NADP. (2015). National Trends Network. National Airfall Deposition Program.

Nakayama, G. (2006). Atmospheric stress corrosion cracking (ASCC) susceptibility of stainless alloys for metallic containers. In: VanIseghem, P. (ed.) *Scientific Basis for Nuclear Waste Management XXIX*, pp. 845-852.

Nakayama, G. and Sakakibara, Y. (2013). Prediction Model for Atmospheric Stress Corrosion Cracking of Stainless Steel. *ECS Transactions* **50**, 303-311.

Newman, J. and Raju, I. (1981). An empirical stress-intensity factor equation for the surface crack. *Engineering Fracture Mechanics* **15**, 185-192.

Newman, J. C. and Raju, I. S. (1979). *Analysis of Surface Cracks in Finite Plates Under Tension or Bending Loads*, Technical Paper 1578 Hampton, VA. NASA.

NRC. (2013). *Finite Element Analysis of Weld Residual Stresses in Austenitic Stainless Steel Dry Cask Storage System Canisters*, NRC Technical Letter Report (ADAMS ML13330A512). Washington D.C. Nuclear Regulatory Commission.

NRC. (2014). *Assessment of Stress Corrosion Cracking Susceptibility for Austenitic Stainless Steels Exposed to Atmospheric Chloride and Non-Chloride Salts*, NUREG/CR-7170. Washington D.C. U.S. Nuclear Regulatory Commission.

Pacific Nuclear Fuel Services, I. (1991). *Topical Report for the NUTECH Horizontal Modular Storage System for Irradiated Nuclear Fuel NUHOMS-24P*, Document NUH-002 Rev. 2A, April 1991. Adams ML110730769.

Parrott, R. and Pitts, H. (2011). *Chloride stress corrosion cracking in austenitic stainless steel: Assessing susceptibility and structural integrity*. U.K. Health and Safety Executive.

Payer, J., Shan, X., Agarwal, A. S. and Landau, U. (2008). Crevice Corrosion Processes in Thin Films of Electrolyte. *NACE Corrosion Conference, March New Orleans, LA*, Paper no. 08266.

Peguet, L., Malki, B. and Baroux, B. (2007). Influence of cold working on the pitting corrosion resistance of stainless steels. *Corrosion Science* **49**, 1933-1948.

Pio, C. A. and Lopes, D. A. (1998). Chlorine loss from marine aerosol in a coastal atmosphere. *Journal of Geophysical Research-Atmospheres* **103**, 25263-25272.

Prosek, T., Iversen, A. and Taxén, C. (2009). Low temperature stress corrosion cracking of stainless steels in the atmosphere in presence of chloride deposits. *Corrosion* **65**, 105-117.

Prosek, T., Le Gac, A., Thierry, D., Le Manchet, S., Lojewski, C., Fanica, A., Johansson, E., Canderyd, C., Dupoiron, F. and Snauwaert, T. (2014). Low temperature stress corrosion cracking of austenitic and duplex stainless steels under chloride deposits. *Corrosion*.

Rossi, M. J. (2003). Heterogeneous reactions on salts. *Chemical Reviews* **103**, 4823-4882.

Schindelholz, E., Tsui, L.-k. and Kelly, R. G. (2013). Hygroscopic Particle Behavior Studied by Interdigitated Array Microelectrode Impedance Sensors. *The Journal of Physical Chemistry A* **118**, 167-177.

Scully, J. R. (1995). Electrochemical Tests. In: Baboian, R. (ed.) *Corrosion Tests and Standards: Application and Interpretation. ASTM manual series, MNL-20*. West Conshohocken, PA. ASTM International.

Seinfeld, J. H. (1986). *Atmospheric Chemistry and Physics of Air Pollution*. New York, NY: John Wiley & Sons.

Shirai, K., Tani, J., Arai, T., Wataru, M., Takeda, H. and Saegusa, T. (2011a). SCC evaluation test of a multi-purpose canister. 10-14 April. *13th International High-Level Radioactive Waste Management Conference (IHLRWMC)*. Albuquerque, NM: American Nuclear Society, 824-831.

Shirai, K., Tani, J. and Saegusa, T. (2011b). *Study on Interim Storage of Spent Nuclear Fuel by Concrete Cask for Practical Use -- Feasiblity Study on Prevention of Chloride Induced Stress Corrosion Cracking for Type 304 Stainless Steel Canister*, CRIEPI N10035 (English translation).

SNL. (2007). *In-drift precipitates/salts model*, ANL-EBS-MD-000045 REV 03. Las Vegas, NV. Sandia National Laboratories.

SNL. (2008). *Analysis of dust deliquescence for FEP screening*, ANL-EBS-MD-000074 REV01. Albuquerque, NM. Sandia National Laboratories.

Speidel, M. O. (1977). Stress corrosion crack growth in austenitic stainless steel. *Corrosion* **33**, 199-203.

Tani, J., Mayuzumi, M. and Hara, N. (2008). Stress corrosion cracking of stainless steel canister for concrete storage of spent fuel. *Journal of Nuclear Materials* **379,** , 42-47.

Tani, J. I., Mayuzurmi, M. and Hara, N. (2009). Initiation and propagation of stress corrosion cracking of stainless steel canister for concrete cask storage of spent nuclear fuel. *Corrosion* **65**, 187-194.

Turnbull, A. (1997). Implications of internal cathodic reactions for crevice attack of stainless steels in chloride environments. *British Corrosion Journal* **32**, 283-290.

Turnbull, A., Mingard, K., Lord, J., Roebuck, B., Tice, D., Mottershead, K., Fairweather, N. and Bradbury, A. (2011). Sensitivity of stress corrosion cracking of stainless steel to surface machining and grinding procedure. *Corrosion Science* **53**, 3398-3415.

Wall, S. M., John, W. and Ondo, J. L. (1988). Measurement of aerosol size distributions for nitrate and major ionic species. *Atmospheric Environment (1967)* **22**, 1649-1656.

Wolery, T. W. and Jarek, R. L. (2003). *Software User's Manual, EQ3/6 Version 8.0*. Albuquerque, NM. Sandia National Laboratories.

Zhang, X. and McMurry, P. H. (1992). Evaporative losses of fine particulate nitrates during sampling. *Atmospheric Environment* **26A**, 3305-3312.